NORTHWESTERN UNIVERSITY

The Effects of Phase Transfers with Thiol Ligands on the Optical Properties of Water-Soluble Quantum Dots

A DISSERTATION

SUBMITTED TO THE GRADUATE SCHOOL

IN PARTIAL FULFILLMENT OF THE REQUIREMENTS

for the degree

DOCTOR OF PHILOSOPHY

Field of Chemistry

By

James Ciro Schwabacher

EVANSTON, ILLINOIS

September 2020

Abstract

The Effects of Phase Transfers with Thiol Ligands on the Optical Properties of Water-Soluble Quantum Dots

James Ciro Schwabacher

This dissertation examines the effects of phase transfers with thiol ligands on the optical properties of quantum dots (QDs) in water by investigating two systems: i) dihydrolipoic acid (DHLA)-capped PbS QDs and ii) thiolated DNA-capped core/shell CdSe/CdS QDs. QDs are bright, monodisperse, and tunable hydrophobic nanoparticles with high photoluminescence (PL) quantum yields (QYs). Phase transfers with thiol ligands impart hydrophilicity to QDs synthesized in organic solvents. However, these procedures often decrease the monodispersity, PL QY, and colloidal stability of the QD ensemble that makes QDs desired as Förster resonance energy transfer (FRET) donors or acceptors in biologically relevant environments. This work probes the relationship between an ensemble's polydispersity and its pH response after phase transfer. The bathochromic shifts of the PL of an ensemble of DHLA-capped PbS QDs can be entirely accounted for by FRET between QDs within aggregates. X-ray scattering techniques indicate that PbS-DHLA QD aggregates are mass fractals formed by clusters of tightly packed QDs in acidic environments. This work, expanding upon existing protocols, presents a new phase transfer method that employs a ternary solvent system to functionalize CdSe/CdS QDs with thiolated-DNA strands in less than one hour without intermediate ligands. This thesis provides insight into the challenges of deploying QDs in aqueous environments and highlights potential solutions.

Acknowledgments

I submit this completed work with sincere gratitude and humility. My life thus far has been relatively lucky despite various challenges and obstacles that I've encountered over the years. This luck, I suspect, is greatly due to the wonderful souls that I continue to meet along my path. Everything that I have ever accomplished and ever will achieve, including this dissertation, is thanks to a vast network of amazing individuals.

First and foremost, it is with unconditional love that I thank my family for their unfettered support: to my mom, Donna, for believing in me when I could no longer; to my dad, Tom, for recognizing and encouraging my grit; to my stepmom Alicia, for indulging my intellectual curiosity and providing sage advice; to my brother, Robert, for lending me his strength and his humor; to my sisters, Avalon and Meridian, for sharing their joy and interest in the world with me; to my father's parents, Donald and Eva Kay, for allowing me to peruse the old dusty books that aligned their walls; to my mother's father and stepmother, Charlie and Minnie, for sharing and creating laughter-inducing memories; to my mother's mother, Marie, for painting a vision of this phase of my life with such clarity and certainty that I knew the path long before I stepped on it. While growing up, my extended family was a village of caring adults that shepherded me into the world. I am forever grateful to each of them for the love, protection, and encouragement they gifted me time and time again. Finally, I am thankful to Scott, who's caring makes it easier for me to do what I must.

There have been many additional families that have provided love and support as if I was born to them—the Barrals, Defalcos, Agnellos, Rotunnos, Reillys, Thatchers, Stefaneses, and Mejias—

and I am forever indebted to them all. I offer extraordinary thanks to Amanda, Jodi, Alyssa, and JJ; without them, I would not be the person I am today. Likewise, I would not be the person I am becoming without Jenny and her family. Words cannot adequately describe how lucky I am to have met Jenny, and it is the single greatest thing (of many) that has ever happened to me.

My teachers at Staten Island Technical High School were critical to my career and were the first scholars to highlight my aptitude for chemistry and physics while helping to uncover my writing style and voice.

To the team of adventurers who taught me my limits and how to move past them—especially Megan, Sam, Cali, Casey, Chelsea, Jose, Emily, Molly, and Melanie—thank you for continuing to teach me new ways to be in the world.

My decision to attend American University in Washington, D.C.—and enter through every door it opened for me—has proven to be one of the best choices that I've ever made. I am grateful to Sebastian, Nida, Leanza, Chelsea W., Chelsea M., and Gaby for continuously celebrating my work, even when I don't think it's adequate, and encouraging me towards each next step. A sincere thanks to my friends and fellow scientists, A. J., Madeleine, Eleni, and Katie, for their support and their work improving our world with science. I must also thank my colleagues in the Dean Peter Starr's Office—especially Marla, Alyssa, Erica, and Mimi—who created a home away from home.

I consider the Department of Chemistry at American to be my academic home, and that is all thanks to Arij Farran and Dr. Jim Girard for offering opportunities that spawned everything else. I am thankful to Dr. Abigail Miller for her time, attention, support (without which I would have never known to apply for fellowships) and overall vote of confidence, and to Dr. Nate Harshman for help and feedback that was critical to getting me to Northwestern. I am grateful for my friend, colleague, and international host, Dr. Svenja Morsbach, for welcoming a novice researcher and

foreigner. I give the warmest of thanks to Dr. Matthew Hartings, who is as true a friend as he is brilliant and as great a mentor as he is a person. I would not be here without him.

My life and the world have changed significantly throughout my time at Northwestern University. I am in awe of the brilliant staff, faculty, and students that I have met here. I am sincerely grateful to the Chemistry Department's staff and student organization leaders for their continued support of graduate and undergraduate students. I am incredibly lucky to have met and worked with Dr. Stephanie Knezz, Dr. Veronica Berns, and Dr. Lauren Woods. Their support and insights enabled me to secure awards and attend conferences that were otherwise inaccessible. They have left permanent, beautiful marks on my professional identity. To my peers and friends, Shaunna, Ariana, Zack, Jen, Lee, Riki, Becky, and Louis, your presence and camaraderie have made my time here sweet and fulfilling.

I am grateful to have had the opportunity to work in the Weiss Lab and share hoods and offices with spectacular scientists. A special thanks to Dr. Rachel Harris, Dr. Kedy Edme, Dr. Ofer Kedem, Dr. Bryan Lau, and Dr. Mohamad Kodaimati for their mentorship, discussions, and overall encouragement. I am grateful to have had the opportunity to mentor and befriend Jeremiah and Aaron. The Weiss lab will always feel special to me, mainly due to my cohort—Jack, Dana, Kevin, Zhengyi, and Kaitlyn—who have been with me every step of the way. Working alongside Dr. Kaitlyn A. Redfern was an honor and a privilege; I could not have done this without her. Lastly, I am grateful for my advisor, Dr. Emily A. Weiss, who taught me how to ask fundamental questions regarding the world around me.

Emily, working under your guidance has changed my life for the better—thank you.

Table of Contents

List of Figures

List of Tables

List of Schemes

Chapter 1: Introduction

1.1 Chapter Summary

This chapter introduces colloidal quantum dots (QDs), semiconductor nanocrystals that are on the order of or smaller than the exciton Bohr radius of the bulk semiconductor material. Their relatively small size results in the confinement of their electronic wavefunctions, which generates size-dependent optoelectronic properties that deviate from the properties of the bulk material. These properties are detailed below, as well as the specifics of two types of QD materials discussed in this thesis: lead sulfide (PbS) and cadmium selenide (CdSe). Well-established QD syntheses and post-synthetic modification methods are also explored before describing QD-QD Forster resonance energy transfer (FRET). The roles of post-synthetic ligand exchanges and QD-QD FRET on the applicability, or lack thereof, of water-soluble QDs to biologically relevant fields are detailed. This chapter concludes with an outline of the research described in this dissertation.

1.2 Properties of Quantum Dots

Colloidal quantum dots (QDs) are semiconductor nanocrystals with electronic wavefunctions that are spatially confined in three dimensions. They are often simplified as nanometer-sized spheres, though this framework ignores the fact that they are faceted.[1-2] When a QD is excited by a photon of some energy equal to or greater than the energy of its QD optical bandgap, an electron is excited from the valance band to the conduction band. This photoexcitation creates an exciton, which is a quasi-particle consisting of a Coulombically attracted electron-hole pair. QD radii are on the order of or less than the delocalization length of an exciton in the corresponding bulk material (*i.e.,* QD radius < exciton Bohr radius), thus QD's exciton is spatially confined in all three dimensions.[3] This confinement yields discrete energy levels for the electron and hole, and the QD's size determines the energy levels' positions.[4]

The relatively small size of QDs, and the resulting quantum confinement, induces size-tunable optoelectronic properties that are different from the properties of the bulk material. QDs are most often sought-after for their broad absorption spectra, which ranges from the ultra-violet to near-infrared[5] regions of the electromagnetic spectrum (depending on QD size and material composition). QDs exhibit extinction coefficients that are an order of magnitude greater than the extinction coefficients of organic dyes. In conjunction with their high absorptivity, their long excited-state lifetimes, which range from 10–3000 ns, narrow emission spectra, and high photoluminescent (PL) quantum yields (QYs) make QDs desirable fluorophores.[6-7] Over four decades of QD research has optimized the production of highly monodisperse QD ensembles with high PLQYs from synthetic procedures using organometallic precursors and hot coordinating solvents.[8-10] These established hot-injection syntheses[11] enable effortless manipulation of the size of the QDs in an ensemble, usually through reactant concentrations, temperature, and/or time, and thus allow researchers to tune the optoelectronic properties of a QD batch.

QDs are also solution-processable and can be post-synthetically modified to tune their optoelectronic properties, reactivity, and solubility by doping the QD lattice[12], shelling the QD core[13-15], encapsulating the QD surface[16], or exchanging the QD ligands[17]. The small sizes and spherical structures of QDs offer large surface-to-volume ratios that provide a significant area for targeted applications, such as sensing or photocatalysis, however large surface-to-volume ratios also make QDs highly sensitive to changes at their surface and within their environment.

The work presented in this thesis was performed using two types of colloidal QDs: PbS QDs and CdSe/CdS core/shell QDs. PbS QDs are IV-VI semiconductor nanocrystals with a rock-salt crystal structure. Their shapes are dependent on the synthetic conditions and colloidal size.[2] PbS QDs have size-tunability over the near-infrared region. The quantum confinement possible with

PbS QDs is stronger than the confinement possible with other QDs, such as CdSe QDs, because of the relatively large exciton Bohr radius (18 nm for PbS[18] *vs.* 5.8 nm for CdSe[19]). CdSe QDs are II-VI semiconductor nanocrystals with either zincblende[20] or wurtzite[21] lattice structures determined by the conditions of their synthesis.[22] CdSe QDs have size-tunability over the visible light spectrum. For the purposes of our research, we add a thin CdS shell to our CdSe QD cores to increase stability and PL QY. The CdS shell passivates the QD surface and suppresses nonradiative recombination.[23]

1.3 QD-QD Energy Transfer

Energy transfer (EnT) is a non-radiative process by which a donor, such as a QD, transfers its excited-state energy to a ground-state acceptor. EnT occurs through either the bilateral exchange of electrons between an excited donor and ground-state acceptor (Dexter energy transfer) or through the simultaneous transmission of excess energy from the excited donor to the ground-state acceptor through the coupling of the donor and acceptor transition dipoles (Förster resonance energy transfer, or FRET)[24], which is the EnT mechanism relevant to the research presented herein. If donors and acceptors are assumed to be point dipoles, then the rate of FRET decays to the sixth power of the donor-acceptor distance; therefore, the donor and acceptor must be brought nearby, usually within 10 nm, to observe EnT. It is possible, though, to extend Förster distances beyond the usual 10 nm when QDs are acceptors for lanthanide-based donors.[7] Besides the donor-acceptor distance, the FRET efficiency is dependent on the refractive index of the medium, the orientation of the donor's emission transition dipole and the acceptor's absorption dipole, the overlap of the donor's emission spectrum and acceptor's absorbance spectrum, and the quantum yield (QY) of the donor.

1.4 Aqueous Quantum Dot Systems

Despite their promising characteristics highlighted above, such as the ability to participate in FRET, QDs have yet to revolutionize fields like biological sensing or biomedical imaging—likely due to challenges presented by the aqueous environments inherent to these applications. The instability of aqueous QDs has been known for some time.[25] The first QDs were, in fact, synthesized using stabilizing agents in aqueous environments and were colloidally unstable.[26-27] Though water-based QD syntheses have since improved, they typically result in ensembles with broader shape and size distributions, and therefore broader optical spectra[28-29] than those synthesized using hot-injection methods. In place of improved syntheses for hydrophilic QDs, the bright, crystalline, and monodisperse hydrophobic QDs produced from hot-injection syntheses are subjected to post-synthetic ligand exchanges to impart hydrophilicity. Unfortunately, post-synthetic phase transfers often induce QD etching, Ostwald ripening, and/or formation of defects that cause PL quenching[30-33]. Furthermore, successful phase transfer and exchange with hydrophilic ligands do not necessarily guarantee colloidal stability in water, especially long-term.

1.5 Dissertation Outline

The research in this dissertation investigates the effects of phase transfers with thiol ligands on the optical properties of QDs in aqueous solutions. In Chapter 1, we introduced the fundamentals and properties of colloidal QDs, specifically PbS QDs that emit near-infrared light, and thinly shelled CdSe/CdS QDs that emit bright visible light. In Chapter 2, we describe how exchanging the native oleate ligands on PbS QDs with dihydrolipoic acid (DHLA) molecules to provide water solubility determines the pH response of aqueous PbS-DHLA QD ensembles. We find that the magnitude of the pH-dependent PL shift is strongly correlated with the polydispersity of the ensemble after phase transfer into water. In Chapter 3, we analyze x-ray scattering measurements

to elucidate the structure and mechanism of formation of PbS-DHLA QD aggregates first observed in Chapter 2. Our analysis suggests that PbS-DHLA QDs pack in clusters with center-to-center distances of approximately 3.8 nm, which then undergo diffusion-limited cluster aggregation (DLCA) or reaction-limited cluster aggregation (RLCA) to form large mass fractal structures. In Chapter 4, we apply a ternary solvent system to explore a new, quick ligand exchange method to functionalize bright CdSe/CdS core/shell QDs with thiolated DNA strands for applications in aqueous environments. In Chapter 5, we present some concluding remarks and three possible future directions for further developing aqueous QD systems.

Chapter 2: Origin of the pH Dependence of Emission of Aqueous Dihydrolipoic Acid-Capped PbS Quantum Dots

Adapted From:

Schwabacher, J. C.; Kodaimati, M. S.; Weiss, E. A. *J. Phys. Chem. C.* **2019**, *123* (28), 17574–17579.

2.1 Chapter Summary

This chapter describes the mechanism behind the pH response of the photoluminescence (PL) of aqueous dihydrolipoic acid (DHLA)-capped PbS quantum dots (QDs). The PL spectra of ensembles of PbS-DHLA QDs bathochromically shift by up to 95 meV as the pH value decreases from 12 to 5. The results of optical spectroscopy and dynamic light scattering experiments, along with the results of a phenomenological model for exciton hopping among QDs, suggest that bathochromic shifts can be entirely accounted for by Förster-type energy transfer (EnT) among QDs as they aggregate with decreasing pH. The magnitude of the PL shift is strongly correlated with the full width at half maximum (fwhm) of the ensemble's PL in its most disaggregated state (i.e., the polydispersity of the sample directly after phase transfer into basic water). Extrapolation of these data to a hypothetically completely monodisperse sample of QDs yields a PL fwhm of an ensemble of single DHLA-capped PbS QDs in water of 130 meV. This work shows that the PL linewidth before aggregation, which is controlled by the phase transfer procedure, is an excellent predictor of the pH response of the emission spectra of the QDs.

2.2 Introduction

Colloidal semiconductor quantum dots (QDs) are bright, highly tunable, and synthetically simple chromophores useful for aqueous photocatalysis and biological sensing[34-35]; both applications have strict requirements for the pH range under which the QDs must operate. QDs synthesized in water have broader shape and size distributions, and therefore broader optical spectra[28-29], than those synthesized in organic solvents[8-10, 36], so water-solubility is typically imparted post-synthetically, through a ligand exchange/phase transfer procedure. Unfortunately, post-synthetic phase transfers in some cases decrease the quality of the QD sample by etching, Ostwald ripening, and/or formation of photoluminescence (PL)-quenching defects[30-33]. Here we

analyze the impact of the phase transfer of near-IR-emitting PbS QDs into water using a popular dithiol ligand[37-42], dihydrolipoic acid (DHLA), on the size dispersity of the sample, and connect this dispersity to the pH-dependence of the ensemble's PL spectrum. As the pH decreases, decreased electrostatic repulsion and increased hydrogen bonding interactions, in the presence of attractive van der Waals forces, cause the aqueous DHLA-capped QDs to aggregate. For polydisperse samples, Förster-type energy transfer (EnT) among QDs within these colloidally stable aggregates results in a bathochromically shifted, narrowed PL spectrum for the ensemble at more acidic pH. A phenomenological exciton hopping model, coupled with experimental data from optical spectroscopy and dynamic light scattering (DLS), indicates that the pH dependence of the emission of these samples can be accounted for entirely by EnT upon aggregation, and that the PL linewidth of a hypothetically completely monodisperse ensemble of PbS QDs is 130 meV in water.

2.3 Quantum Dot Synthesis and Ligand Exchange

We synthesize and purify oleate (OA)-capped PbS QDs, approximately 3.2 nm in diameter, according to established procedures.[8] All syntheses, ligand exchanges, titrations and sample preparations are conducted under nitrogen atmosphere with degassed solvents to minimize oxidation of the QD surfaces and their ligands. To solubilize the PbS QDs in H_2O (or D_2O, which we use in the PL experiments instead of H_2O to prevent reabsorption of the near-IR QD emission), we add 4 μL of DHLA from a previously prepared stock of reduced lipoic acid to 5 mL of 15 μM PbS-OA QDs in $CHCl_3$ in a 15-mL centrifuge tube (420 DHLA equiv. per QD). We then add 30 μL of 0.5 M NaOH (1.7 equiv. per DHLA), followed immediately by 5 mL of degassed H_2O, and vigorously shake the tube for five seconds. We open the tube and add an additional 70 μL of 0.5 M NaOH (4.0 equiv. per ligand), re-seal the tube, and shake for approximately three minutes until

a clear black layer forms at the top of the beige solution in the centrifuge tube. We centrifuge the mixture at 7500 RPM for 5 minutes, after which we carefully remove the top (dark brown) aqueous layer with a syringe and filter the solution into a clean vial using a syringe filter (0.22 μm pore size). The resulting ~10 μM aqueous QD dispersions are basic (pH ~ 10.5 pH) after exchange.

2.4 Sample Preparation

We dilute 333 μL aliquots of the exchanged stock into six 5-mL samples of 1 μM PbS-DHLA QDs with pH values of 12, 11, 9, 7, 6, and 5. We adjust the pH by the addition of 0.5 M NaOH or 0.5 M HCl and add aliquots of 0.1 M NaCl as necessary to maintain an ionic strength of ~0.01 M across all samples. For complete experimental details, see section 2.7.

2.5 Results and Discussion

Figure 2.1, solid lines, shows that the PL spectra of a series of samples of 1 μM PbS-DHLA QDs shift to lower energy by 40 meV and narrow by 19% upon decreasing the pH from 12 to 5; this range spans the pK_a of the free thiol (=10.3) and of the carboxylic acid of DHLA when bound to the QD (=8.6, see section 2.7). The intensity of the PL increases as the pH decreases from 12 to 9, and then decreases as the pH decreases from 9 to 5 (shown explicitly in Figure 2.10 in section 2.7), a result that has been reported previously.[38, 43-45]

Particles within all aqueous PbS-DHLA QD dispersions begin to agglomerate when pH < 9, as reflected in an increase in the baseline of their absorbance spectrum as the pH decreases (**Figure 2.2A**).[46] **Figure 2.2B** displays the volume distribution, in percent, of the hydrodynamic diameter for dispersions of PbS-DHLA QDs at pH = 12, 11, 9, 7, 6, and 5, measured by dynamic light scattering (DLS), a technique utilized in similar systems[47]. The distribution shifts to larger average

sizes with decreasing pH. Basic solutions (pH ≥ 9) contain particles with hydrodynamic diameters

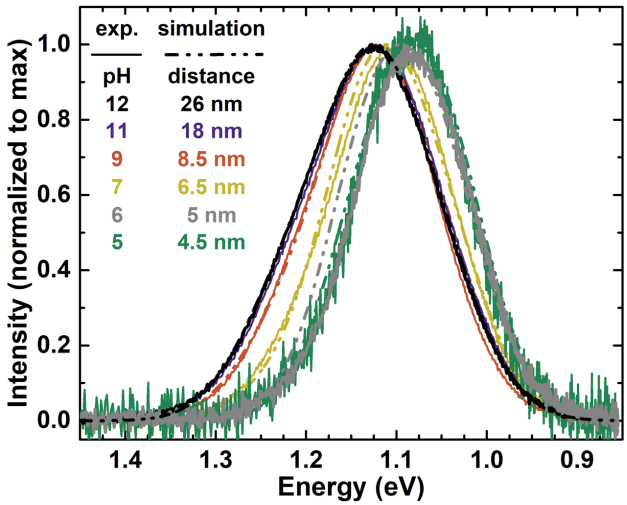

Figure 2.1 Experimentally measured PL spectra of 1 μM PbS-DHLA QDs (in D_2O) as a function of pH (solid lines), superimposed with simulated PL spectra for a polydisperse PbS QD ensemble with a series of average center-to-center interparticle distances (dashed lines).

smaller than 10 nm, which are colloidally stable for a few days if stored in the dark under inert atmosphere, while more acidic solutions contain colloidally stable particles with hydrodynamic diameters as large as 360 nm. These acidic solutions also contain precipitates that migrate to the bottom of the cuvette, which is outside the DLS measurement window, and, thus, cannot contribute to the measured distribution. For more details, see section 2.7.

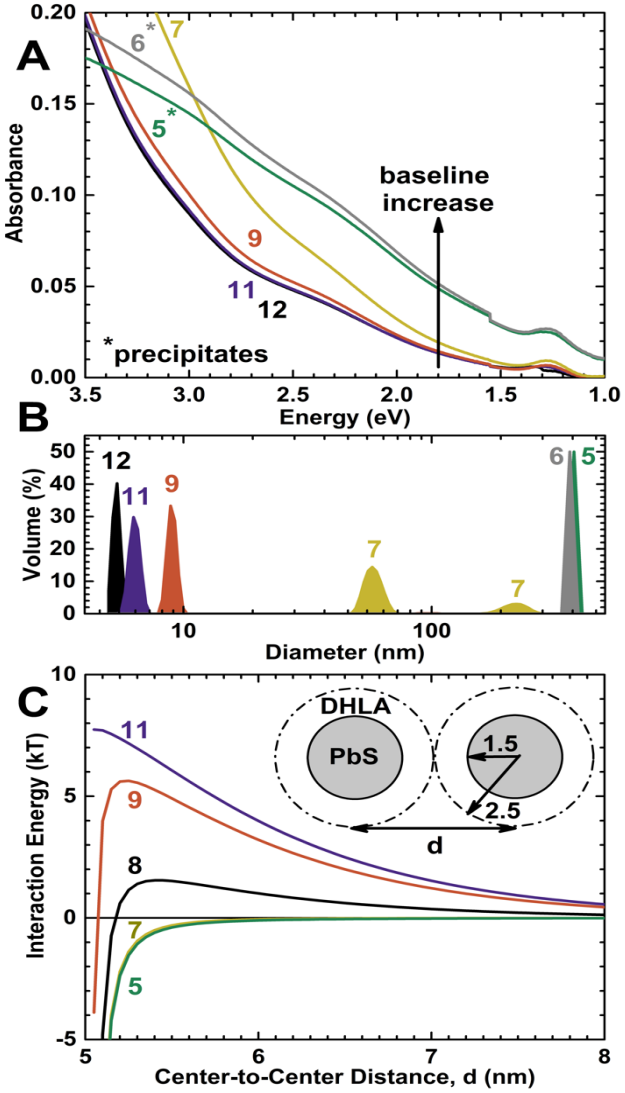

Figure 2.2 A) Absorbance spectra of 1 μM PbS-DHLA QDs (aq) as the pH was adjusted from 12 to 5 by the addition of 0.5 M NaOH or 0.5 M HCl. The black, purple, orange, yellow, grey, and green colors denote pH values of 12, 11, 9, 7, 6, and 5, respectively. **B)** The volume percent distribution of the hydrodynamic diameter, in nm, measured by DLS, over the same pH range. **C)** The calculated interaction energy between two 3-nm DHLA-capped QDs, in *kT*, as a function of center-to-center distance, d, in nm. See section 2.7 for calculation details. The repulsiveness of the interaction, indicated by a positive *U* value, decreases as the pH decreases.

We follow the work of Grzybowski and coworkers[48-50], which builds upon Derjaguin—Landau—Verwey—Overbeek (DLVO) theory to improve the description of the interactions of charged particles at short separations, to describe the pH dependence of the observed aggregation. We estimate the interaction energy, *U*, between two PbS-DHLA QDs as a function of center-to-center distance, d, for dispersions with pH values of 11, 9, 8, 7, and 5 (**Figure 2.2C**) using **eq 2.1**. This model decomposes the interaction energy into a sum of the van der Waals

$$U(d, pH) = U_{vdw}(d) + U_{es}(d, pH) + U_{hb}(d, pH) \qquad (2.1)$$

(U_{vdw}), electrostatic repulsion (U_{es}), and hydrogen bonding (U_{hb}) interactions between two QDs, where the strength of the electrostatic repulsion and hydrogen bonding are modulated by pH through the protonation state of the terminal carboxylate group of DHLA (pK_a = 8.6 when bound to the QD). Protonation of the carboxylate decreases the electrostatic repulsion between ligand shells while increasing the number of hydrogen bonds possible at contact. At high pH, electrostatic repulsion is stronger than the attractive interactions to yield a dispersion of individual QDs. As the pH decreases, the repulsion weakens, which allows the short-range attractive forces to dominate to yield QD aggregates. For complete calculation details, see section 2.7.

We hypothesized that Förster-type EnT within the polydisperse ensemble of PbS-DHLA QDs was at least partially, if not entirely, responsible for the observed bathochromic shift in PL as QDs aggregate with decreasing pH (**Figure 2.1**). EnT decreases the emission from smaller (higher-energy) populations and increases the emission from larger (lower-energy) populations, and, for samples comprising populations with overlapping PL spectra, effectively "red-shifts" the observed emission peak. We previously found[51] that increasing the Zn^{2+} concentration of a solution of aggregated glutathione-capped PbS QDs increases EnT but does not change the aggregate size measured by DLS, which plateaus at relatively low Zn^{2+} concentrations. We interpreted this result

to mean that the QDs initially form loosely bound aggregates, and that continuing to increase the Zn^{2+} concentration decreases the average interparticle distance within these aggregates. Steady-state and time-resolved PL confirmed inter-QD EnT upon coupling with Zn^{2+}. To determine the contribution of EnT to the shift in PL energy as a function of pH in **Figure 2.1**, we first identified three spectroscopically distinct populations of DHLA-capped QDs within the disaggregated (pH 12) sample by fitting the measured PL spectrum for this sample with three Gaussian curves, see section 2.7, Figure 2.12. This is the minimum number of Gaussian curves required to satisfactorily deconvolute QD PL spectra before and after aggregation. We assume that these same three populations are present in the samples at every pH value, and use a kinetic master equation model, governed by **eq 2.2,**[43, 51] to calculate the exciton population of each of the three sub-populations of

$$\frac{d}{dt}P_i(t) = P_i(t)\left\{-\frac{1}{\tau_i} - \sum_{j\neq i} k_{i,j}\right\} + \sum_{j\neq i} k_{j,i}P_j(t) \qquad (2.2)$$

QDs as a function of time, for various degrees of aggregation. The degree of aggregation is quantified in the model as average interparticle distance within the entire ensemble; the average interparticle distance ranges from the diameter of the QD, including ligand shell, for the most aggregated sample, to >8× the diameter of the QD for the most disaggregated sample.

These simulations are initiated by randomly photo-exciting QDs and are propagated forward in time until all excitons have completely decayed. Throughout the simulation, we "collect" the photons emitted by each population of QDs in order to reconstruct the steady-state PL spectra of the entire system. We initially create excitons in random locations within QD assemblies (on average, 10% of the QDs within each assembly is photoexcited), and then allow the exciton to hop from QD to QD, with rate constants $k_{i,j}$ (**2.2**) for EnT between QDs *i* and *j*. The EnT rate constants are determined by Förster theory with the point-dipole approximation[52], using experimental

parameters including the absorption and emission spectra, radiative lifetime, and fluorescence quantum yield. We have determined previously[43] that the point-dipole approximation is adequate for predicting EnT lifetimes for this range of interparticle distances among PbS QDs. In **eq 2.2**, $P_i(t)$and $P_j(t)$ are the photoexcited populations of QDs *i* and *j*, respectively, τ_i is the previously reported intrinsic lifetime of aqueous PbS QDs[43]. We randomly assign QDs to be either "dark" or "bright" for the duration of each simulation run with the bright/(dark+bright) ratio equaling the experimentally measured PL QYs. Once a QD is assigned to be dark, we set its rate of radiative recombination and EnT to other QDs to zero; the rate of non-radiative decay in our case is arbitrary and cannot affect the outcome of the simulation. The SI contains details of the simulation.

The output of these simulations is the emission spectrum of our experimental QD ensemble as a function of average interparticle distance, and we can find a series of these distances for which the simulated and experimentally measured PL spectra of our samples at various pH values overlay (**Figure 2.1**, dashed lines). Disaggregated samples (pH=12) correspond to simulated spectra for average interparticle distances that are at least six times greater than the QD diameter, while aggregated samples (pH=5) correspond to simulated spectra for average interparticle distances of 4.5 nm, which is similar to interparticle distances within aggregates observed in our previous work[43, 51], and is reasonable for QDs that are 3 nm in diameter and coated with DHLA (8-carbon chain, ~1 nm). From the simulated and experimentally measured spectra, we calculate a parameter we denote "PL Weighted Average", which is the sum of the emission intensity (in counts) at each wavelength multiplied by its corresponding energy (in eV) for the entire emission spectrum, divided by the total emission (in counts) simulated or measured, (**eq 2.3**). This parameter

$$\text{PL Weighted Avg.} = \frac{\sum_{i=0}^{n} I_i \lambda_i}{\sum_{i=0}^{n} I_i} \qquad (2.3)$$

allows us to characterize the shape of each emission spectrum with a single number. **Figure 2.3A** shows that the experimentally measured plot of PL Weighted Average *vs*. pH overlays well with the simulated plot of PL Weighted Average *vs*. interparticle distance. This agreement implies that

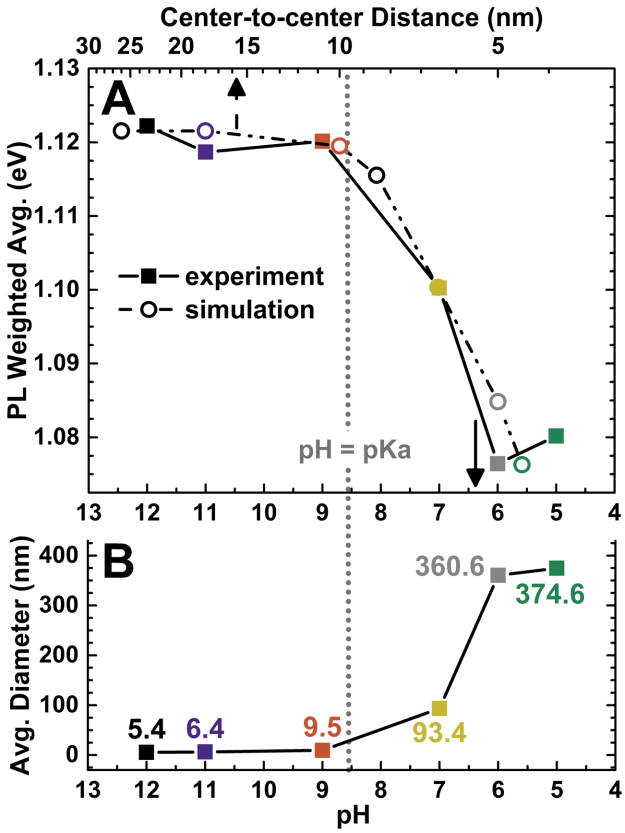

Figure 2.3 A) The weighted average of the experimentally observed PL peak energies of 1 μM PbS-DHLA QDs (aq) (filled squares, solid line), in eV, as a function of pH (bottom x-axis), superimposed with the weighted average of the simulated PL peak energies (open circles, dashed line) as a function of the average interparticle center-to-center distance, in nm (top x-axis). The grey dotted line indicates the measured apparent pK_a of the PbS-DHLA QD carboxylate, 8.6. **B)** Average hydrodynamic diameter of PbS-DHLA QD aggregates, measured with DLS, in nm, as a function of pH. The greatest change in the PL energy is correlated with the greatest increase in aggregate size, which is observed when pH < pK_a = 8.6.

the observed pH dependence of the PL spectra can be accounted for entirely by aggregation-enabled EnT given spectroscopically measured optical parameters of the system and physically reasonable interparticle distances. Simulating the PL as a function of aggregate size at a constant interparticle distance fails to accurately describe our experimental trend, which reinforces the

validity of our model. This conclusion is further supported by the correlation between the plots of PL Weighted Average *vs.* pH and measured average aggregate size *vs.* pH (**Figure 2.3B**).

The *y*-axis of **Figure 2.4** is "ΔPL Weighted Avg.", the effective shift in the emission spectra of 15 PbS-DHLA QD samples to lower energy induced by aggregation on going from a pH ≥ 10.7 to a pH ≤ 6. The *x*-axis of **Figure 2.4** is the FWHM of each PL spectrum at pH ≥ 10.7. The PL FWHM values for the ensembles before aggregation are direct measures of the size polydispersity of the QD sample after ligand exchange and transfer into water. Given that there is no correlation

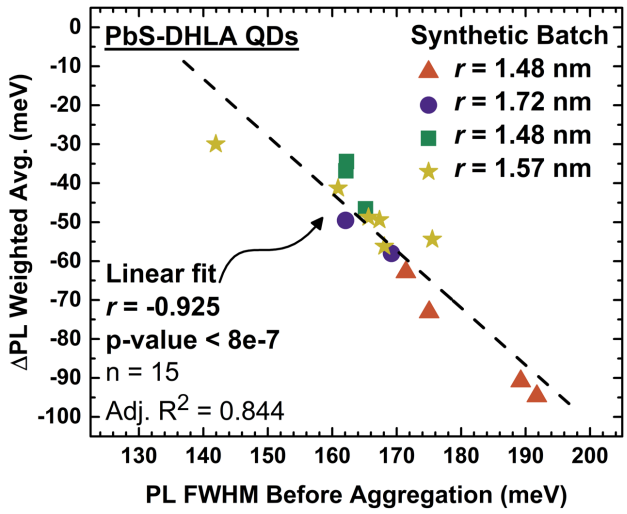

Figure 2.4 Plot of the bathochromic shift, quantified as the change in the weighted average of the ensemble PL, upon changing the pH from ≥10.7 to ≤ 6, *vs*. the PL FWHM of DHLA-capped PbS QDs in the disaggregated state (pH ≥ 10.7), for 15 exchange/titration experiments. PbS QDs, ~ 3.0 to 3.4 nm in diameter, from four separate syntheses (orange triangles, squares, purple circles, green squares, and yellow stars) were used. The PL FWHM were measured when the PbS QDs were disassembled. Linear fitting (adjusted R^2 = 0.844) yields a statistically significant (p-value < 8e-7) Pearson's correlation coefficient, r = -0.925. Section 2.7, Table 2.2, contains details about the preparation of each sample.

between ΔPL Weighted Avg. and the PL FWHM of the PbS-OA QDs *before* ligand exchange (see section 2.7), the strong correlation in **Figure 2.4** indicates that the ligand exchange process itself introduces the polydispersity within the ensemble that promotes EnT as the QDs aggregate with

decreasing pH. We performed calculations to show that the apparent linear relationship between ΔPL Weighted Avg. and the FWHM of the disaggregated sample is almost certainly a result of overlaying non-linear plots from several batches of QDs (see section 2.7, Figure 2.15). If, however, as we propose, the shift in PL of the samples with decreasing pH is caused entirely by aggregation, then ΔPL Weighted Avg. upon aggregation of a completely monodisperse ensemble of PbS-DHLA QDs is, by definition, zero, and the *x*-intercept of the fit line to the empirically linear plot **Figure 2.4** is the homogeneous linewidth of PbS QDs. Indeed, the value of this *x*-intercept (130 ± 5 meV) agrees well with what has been observed previously[53] for the homogenous linewidth of a PbS QD ensemble (125 meV) and approaches the PbS QD single QD linewidth estimate[54] of 100 meV.

2.6 Chapter Conclusion

In summary, the bathochromic shift of the PL of aqueous PbS-DHLA QDs as pH decreases from 12 to 5 can be entirely accounted for by Förster-type EnT among QDs as they aggregate with decreasing pH. This result indicates that the PL linewidth of the QD ensemble in the disaggregated state, a metric for their size dispersity after phase transfer, is an excellent metric for judging not only the quality of a phase transfer but also the degree to which the PL will shift as the QDs form colloidally stable aggregates. For DHLA-coated QDs, this aggregation is driven by protonation of the carboxylate groups of DHLA ligands. The ensemble polydispersity varies between phase transfer attempts; while this irreproducibility here helps us to determine the relationship between the polydispersity and the pH response, it suggests that further work is needed to develop DHLA-based ligand exchange procedures that consistently yield monodisperse QD ensembles with pH-independent spectra. While there is some debate concerning the sources of PL energy and broadening for PbS QDs[32, 53-55], our data suggests that PL FWHM of an ensemble of monodisperse PbS QDs is 130 meV.

This work also implies that choice of a particular phase transfer procedure can serve as a handle to tune the pH response of an aqueous QD system. Tuning the pK_a values of the terminal (solubilizing) groups of the QD-ligand system will alter the degree of aggregation as the pH is adjusted. Eliminating aggregation will require the use of ligands that favor interparticle repulsion by retaining their charges over wide pH ranges, such zwitterionic ligands that contain at least one charged functional group at all pH values in the desired range[56], ligands that extend tertiary amines into solution (pK_a=10.7)[56], or ligands that offer colloidal stabilization without charge, such as poly(ethylene glycol) derivatives[35, 57]. If it is desirable to prevent a pH response of the emission energy, then QDs must be monodisperse or have thick shells that inhibit EnT.

2.7 Supplementary Information

2.7.1 Synthesis of PbS Quantum Dots

We synthesized oleate-capped PbS quantum dots using a protocol adapted from Hines *et al*.[8] We dissolved 0.36 g lead oxide (PbO, MilliporeSigma, 99.999%) in 20.05 ml solution of 19 mL of 1-octadecene (ODE, MilliporeSigma, 90%) and 1.05 mL of oleic acid (OA, MilliporeSigma, 90%) in a 50 ml three-neck flask at 120 °C under N_2 atmosphere. We bubbled N_2 through the mixture while stirring at 120 °C for 30 min, and then at 150 °C for an additional 30 min. We stopped bubbling N_2 but maintained N_2 flow through the flask and cooled the reaction mixture to 110 °C. We used bis(trimethylsilyl)sulfide (TMS, MilliporeSigma) as the sulfur precursor. The precursor solution was prepared by dissolving 0.14 ml of TMS in 8 ml ODE that was purged with dry N_2 for 1 hour at ambient temperature while sonicating. We quickly injected the sulfur precursor into the solution of lead oleate at 110 °C and immediately removed the heating mantle. Once the solution cooled < 50 °C, the reaction mixture was divided into four 50-mL centrifuge tubes. We added 40 mL of acetone to each centrifuge tube and shook the mixture to wash the PbS QDs. We

centrifuged the mixture at 3500 rpm for 20 min. After removing the supernatant and drying the pellet with N_2, we resuspended the QDs in minimal hexanes. We repeated the washing process again by adding 40 mL of methanol and centrifuging at 3500 rpm for 20 min. We dried the resulting pellet and resuspended it with a small amount of hexanes, added 50 mL of methanol, centrifuged at 3500 rpm for 20 min a third time. We repeated the washing procedure for a final (fourth) time with acetone. After the QD pellets were dried under N_2 flow, they were dispersed in hexanes. We stored the PbS-OA QD stock in the dark and sealed under N_2 atmosphere.

2.7.2 Sizing of PbS QDs via Ground State Absorption

All ground state absorption spectra were obtained on a Varian Cary 5000 spectrometer using a 2 mm/10 mm dual pathlength quartz cuvette. We excited our samples along the 2 mm axis and corrected the baselines with solvent blanks prior to measurement. We collected the absorption spectra for the synthesized PbS-OA QDs and determined their size from the position of the first excitonic peak using the calibration curve published by Moreels *et al.*[58], a method that we previously corroborated[59] *via* TEM. All concentrations of QDs were calculated from the absorbance of QDs at 400 nm.

2.7.3 Steady State Photoluminescence Measurements

The photoluminescence (PL) spectra were measured with a Horiba Fluorolog-3 spectrofluorometer using a right-angle geometry and a 2 mm/10mm dual-pathlength cuvette. The excitation beam was applied along the 10-mm path of the cuvette and the sample emission was collected along the 2-mm path. The excitation and emission slit widths were 5 nm.

2.7.4 Calculating PL fwhm

The PL full width at half maximum (fwhm) was manually calculated for each PL spectrum by taking the difference in energy for the two points that were half the maximum emission intensity.

2.7.5Preparation of Stock Solutions

Milli-Q water (18.2 MΩ·cm at 25 °C) was used for all aqueous solutions. Solutions were purged of air by bubbling with dry N_2 while submerged in a sonicating bath.

2.7.6 Preparing Dihydrolipoic Acid (DHLA) from Lipoic Acid (LA).

DHLA was prepared from lipoic acid following the procedure outlined by Uyeda *et al*.[60] Briefly, lipoic acid was dissolved in 0.25 M $NaHCO_3$ and cooled in an ice bath. $NaBH_4$ was added slowly while stirring 2 h below 4 °C. The reaction mixture was acidified with 6 M HCl to pH = 1, extracted with toluene, and dried over $MgSO_4$. After evaporation of the solvent, the desired product was a clear colorless oil that was stored in the dark in a refrigerator. ^{1}HNMR ($CDCl_3$): δ 10.5 (bs, 1H), 2.93 (m, 1H), 2.71 (m, 2H), 2.38 (t, J = 7.3 Hz, 2H), 2.0–1.4 (m, 8H), 1.35 (t, J = 8.0, 1H), 1.30 (d, J = 7.6, 1H).

2.7.7 Ligand Exchange with DHLA

We prepared water-soluble PbS QDs capped with DHLA as described in section 2.3, which was adapted from Deng *et al*.[61]

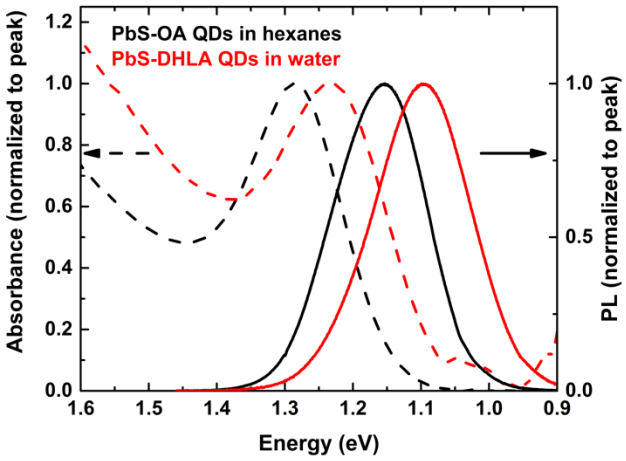

Figure 2.5. The absorbance (dashed) and emission (solid) spectra, normalized to their peaks, for PbS QDs before and after phase transfer from hexanes (black) to water (red) with DHLA.

2.7.8 Dynamic Light Scattering (DLS) and Titrations

All PbS-QD samples were prepared in a polymer glove box (Terra Universal) under N_2 atmosphere. We triple rinsed 20-mL scintillation vials and 1-cm path-length disposal cuvettes with syringe-filtered (0.22 μm pore size) Milli-Q water to minimize dust interference in our DLS measurements. Equal (333 μL) aliquots of the PbS-DHLA QD (aq) stock solution were distributed into six scintillation vials. Each sample was diluted with the volumes of D_2O, 0.5 M NaOH or 0.5 M HCl, and 0.1 M NaCl necessary for achieving a 5 mL solution of 1 µM PbS-DHLA QDs with approximately ~ 0.01 M ionic strength at the pH values of 12, 11, 9, 7, 6, and 5. We transferred and sealed 3 mL of each sample in a 1-cm path-length cuvette DLS measurements, while the rest of the sample was used for absorbance and PL measurements. We measured the hydrodynamic diameters of the dispersed QDs and the aggregates with a dynamic light scattering analyzer (Malvern, Zetasizer Nano). The samples were illuminated with 633-nm He-Ne laser at 25 °C for each measurement. The pH of each samples was confirmed using pH test strips (MQuant pH 0 – 14 Universal Indicator, Millipore Sigma).

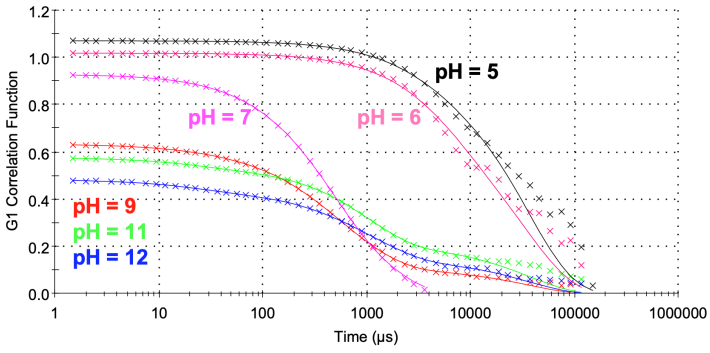

Figure 2.6. Representative distribution fits, exported from the Malvern Zetasizer Nano software, for one measurement of 1 μM PbS-DHLA QDs at each pH value (pH = 12, 11, 9, 7, 6, and 5).

2.7.9 Colloidal Stability

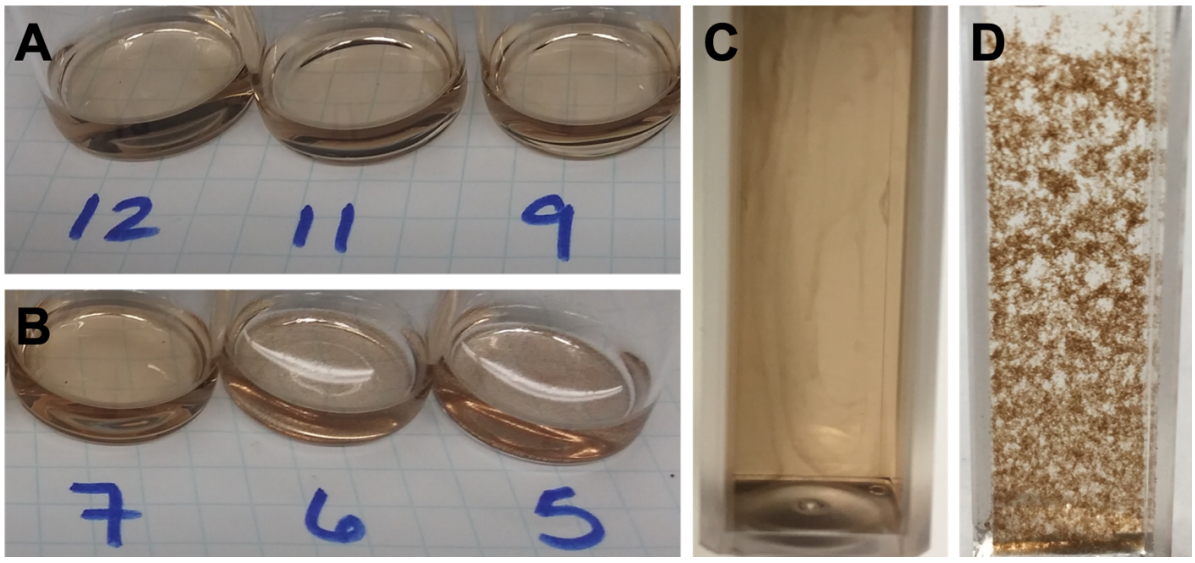

Figure 2.7. Photographs of aqueous 1 μM PbS-DHLA QDs in water after being stored under N_2, in the dark, for three days at various pH values (pH = 12, 11, and 9, **A**; pH = 7, 6, and 5, **B**). The QDs begin to flocculate at pH ≤ 6 (**C**), and will continue to precipitate and settle, which is most visible if left to form in a 2 mm path-length cuvette (**D**).

2.7.10 Titrations and Fitting for pKa

The development of functions for fitting titration data was informed by previous work.[62-63]

Triprotic acid Titrated with a Strong Base. We developed a function to use in Origin to find the pK_a of each function group of DHLA. We fit our experimental data to **eq 2.4**, where

$$V_b = -\left(\frac{V_a*\left(H^5-AH^3K_1+H^4K_1-2AH^2K_1K_2+H^3K_1K_2-3AHK_1K_2K_3+H^2K_1K_2K_3-H^3K_w-H^2K_1K_w-HK_1K_2K_w-K_1K_2K_3K_w\right)}{(BH+H^2-K_w)*(H^3+H^2K_1+HK_1K_2+K_1K_2K_3)}\right) \quad (2.4)$$

V_b is the total volume of titrant added, in mL, V_a is the sample volume, in mL, H is the molar proton concentration (converted from our experimental pH measurements where $H = 10^{-pH}$), A is the concentration of acid at the start of the titration, B is the concentration of base in the titrant,

and K_w is the ionization constant of water (assumed here to be $1 * 10^{-14}$). Our fit yields K_1, K_2, and K_3, which we convert to pK_a.

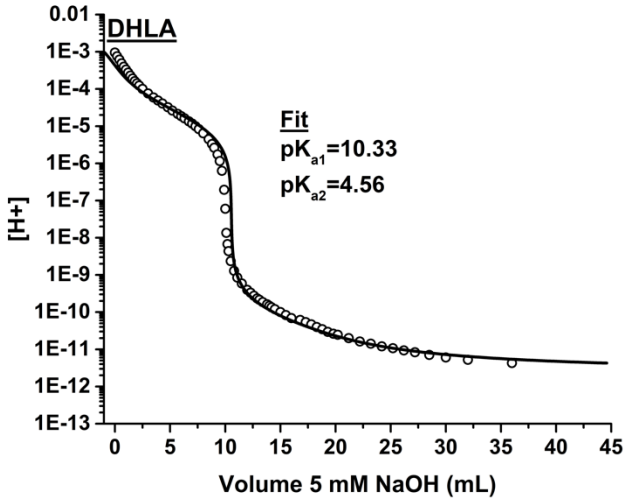

Figure 2.8. Titration of DHLA in water (pH=3) with 5 mM NaOH. Fitting with the triprotic acid function (**eq 2.4**) yields two distinct pK_a values of 10.33 and 4.56, which correspond to the thiol and carboxylate groups of free DHLA.

Method for PbS-DHLA QD Titration. PbS-DHLA QD (aq) stock solutions were diluted to 1 μM samples of 8 mL or more in volume. The pH was adjusted to the titration starting point by the addition of 0.5 M NaOH. The prepared sample was titrated with 0.5 M HCl. The pH was measured using a Hanna Instrument potable pH meter (HI 9126) calibrated with pH = 12.00 (Ricca Chemical) and pH = 1.00 (Hanna Instruments) buffer solutions.

Origin Fitting Function for Triprotic Acid Titrated with a Strong Base. We developed a function to use in Origin to find the apparent pK_a of PbS-DHLA QDs. We fit our experimental

$$V_t(H) = -1 * \left(\frac{C_n + F_{a1} * C_a * (1-r) + F_{a2} C_a r + H - \left(\frac{K_W}{H}\right)}{-1 * C_t + H - \left(\frac{K_W}{H}\right)} \right) * V_s \qquad (2.5)$$

titration data to **eq 2.5**, where $V_t(H)$ is the total volume of titrant added, in mL, V_s is the starting volume, in mL, H is the molar proton concentration (converted from our experimental pH measurements where $H = 10^{-pH}$), $C_n$is the concentration of excess hydroxide at the start of the

titration, C_a is the concentration of ligand at the start of the titration, C_t is the concentration of acid in the titrant, r is the fraction of ligands bound to the QD (0.2 for 420 equiv. of DHLA per QD), and K_w is the ionization constant of water (assumed here to be $1 * 10^{-14}$). **Equation 2.5** relies on the terms F_{a1}, F_{a2}, d, and e, as described below:

$$F_{a1} = \left(\frac{2H^2}{d}\right) + \left(\frac{K_1 H}{d}\right) \quad (2.6)$$

$$F_{a2} = \left(\frac{2H^2}{e}\right) + \left(\frac{K_3 H}{e}\right) \quad (2.7)$$

$$d = H^2 + HK_1 + K_1K_2 \quad (2.8)$$

$$e = H^2 + HK_3 + K_3K_4 \quad (2.9)$$

We set $K_n = 10\text{^} - (pK_{an})$ and fix $pK_{a3} = 4.56$ and $pK_{a4} = 10.33$ for the population of free DHLA. We fit our experimental data, allowing pK_{a1} and pK_{a2} to float, to determine the apparent pK_a of PbS-DHLA QDs.

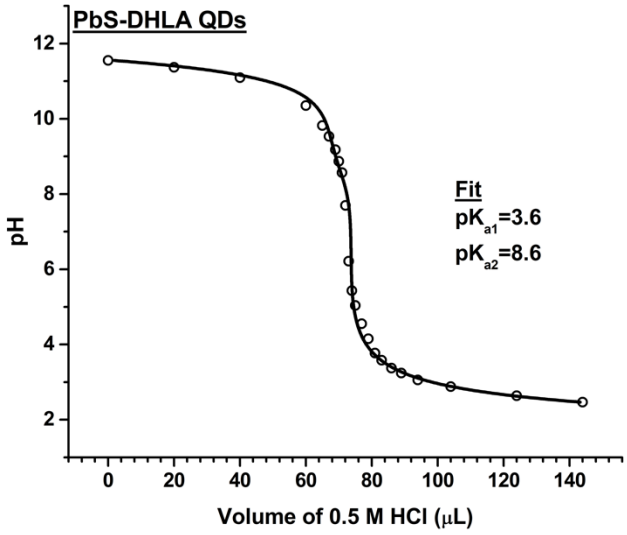

Figure 2.9. Titration of 9 mL of 1 μM PbS-DHLA QDs in water (pH=11.55) with 0.5 M HCl. Fitting results in the two pK_a values of 3.6 and 8.6 for QD-bound DHLA molecules, which correspond to the thiol and carboxylate groups.

2.7.11 PL Intensity as a Function of pH

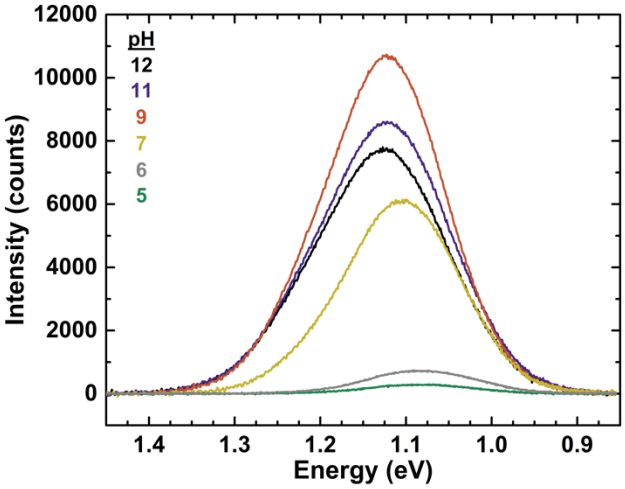

Figure 2.10. The PL of PbS-DHLA QDs as pH decreases from 12 to 5. Normalized data displayed in **Figure 2.1**.

2.7.12 Quantification of DHLA Ligands within the Ligand Shell of PbS QDs

We prepared 15 μM of DHLA-capped, water-soluble PbS QDs using the procedures described above and 100 equiv. of DHLA per QD. We applied ^{1}H NMR to quantify the number of bound DHLA ligands per QD. We set the acquisition time to 27 s and the relaxation time to 90 s, respectively, to allow for complete collection of the free induction decay signal and sufficient relaxation of proton nuclei between measurements, and performed 32 scans to get a spectrum with satisfactory signal-to-noise ratio. The 2.1 – 2.4 ppm region of the resulting spectra (which contains signal from the methylene protons alpha to the carboxylate group in DHLA) is fit with a sum of Lorentzian functions as we described in our previous work.[37] The broad feature centered at ~2.22 ppm corresponds to those protons of DHLA ligands that are bound to the surface of QDs. We compare the area of the broad feature to the area of the sharp features to determine the number of bound ligands. Our result of approximately 83 DHLA/PbS-QD aligns with our previous measurements with DHLA derivatives.[37]

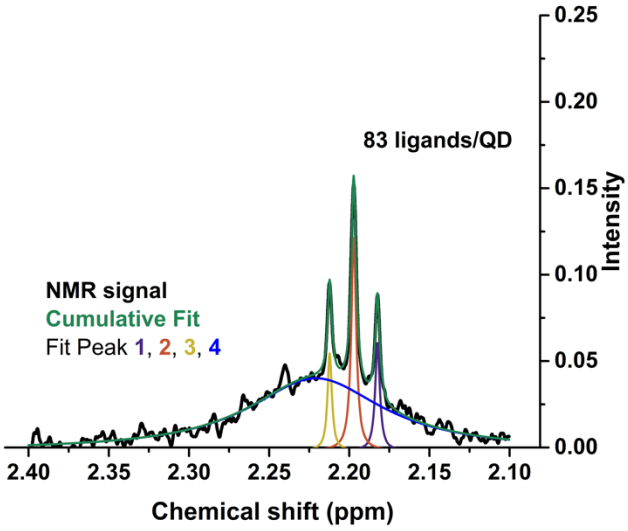

Figure 2.11. ^{1}H NMR spectra of DHLA-capped PbS QDs zoomed in at 2.1 – 2.4 ppm. The fitting lines are the best fits using a sum of four Lorentzian functions. The broad feature (blue trace) corresponds to the population of DHLA that are bound to the surface of QDs.

2.7.13 Model for Interparticle Potential Energy

Following the work of Grzybowski and coworkers[48-50], we define the van der Waals energy between two QDs (due to interactions between the QD cores) in units of k_BT, as a function of separation distance between ligand shells, h, where A is the Hamaker constant for PbS across water, R_c is the radius of the PbS QD core, r is the radius of the core and ligand shell, k_B is Boltzmann's constant, and T is temperature.

$$U_{\mathrm{vdw}} = \begin{matrix}(-A/3\,((\mathrm{R_c^2}/\big((h+2r)^2-(4\mathrm{R_c^2})\big)) + (\mathrm{R_c^2}/(h+2r)^2) \\ +0.5 * \log[1-((4\mathrm{R_c^2})/(2r+h)^2)]))\end{matrix} /(k_BT) \quad (2.10)$$

We use a simple estimation of the energy of hydrogen bonding, $\mathrm{U_{hb}}$, as a function of h, where $\mathrm{Q_h}$ is the charge on a hydrogen atom of a water molecule, $\mathrm{u_d}$ is the dipole strength of acetic acid, ϵ is the relative permittivity of water, and ϵ_0 is the vacuum permittivity.

$$\mathrm{U_{hb}} = \mathrm{N_{hb}}((-\mathrm{Q_h u_d})/(4\pi\epsilon\epsilon_0)) * (1/h^2) * (1/(k_BT)) \quad (2.11)$$

The maximum number of hydrogen bonds possible at contact for a given pH, N_{hb}, is defined as:

$$N_{hb} = (\Gamma_0 - \Gamma) * A_{eff} \quad (2.12)$$

where Γ is the number of deprotonated ligands per m^2 on a QD with a total coverage of Γ_0 ligands per m^2, and $A_{eff} = 2\pi r a$ is the effective area of contact between two QDs with total radius, r, in meters that takes into account the minimal distance between two dipoles, a. We relate Γ to the solution pH by

$$\Gamma = \frac{\Gamma_0}{1+10^{pK_a - pH}} \quad (2.13)$$

where the pK_a corresponds to the protonation of the PbS-DHLA carboxylate tail.

We use the thermodynamic integration method to estimate the electrostatic potential between two charged QDs in equilibrium with an electrolyte solution.[48-49] We employ the linearized Poisson–Boltzmann equation for an isolated nanoparticle with a charge regulating boundary condition, which gives the relation

$$\frac{(G-e\varphi)}{k_B T} - \log\left[\left((-e\Gamma r) - (\epsilon_0 \epsilon \varphi) - (\epsilon_0 \epsilon \kappa r \varphi)\right) / \left((\epsilon_0 \epsilon \chi_B \varphi) + (\epsilon_0 \epsilon \chi_B \kappa r \varphi)\right)\right] = 0 \quad (2.14)$$

where the Debye screening length, κ, is defined as $\kappa = (\epsilon \epsilon_0 k_B T / 2 N_A c_s e^2)^{-\frac{1}{2}}$ and χ_B is mole fraction of counter ions in solution, G is the free energy of ion dissociation in the absence of any external fields, N_A is Avogadro' s number, c_s is the monovalent salt concentration, and e is the elementary charge. We solve this relation for the surface potential at infinite separation φ, and rename this solution as Φ.

To calculate the electrostatic potential, we first need to calculate the surface charge density at the QD surface. The surface charge density, σ, can be expressed as **eq 2.15** where ϕ is the electrostatic

$$\sigma = -e\Gamma/(1 + \chi_B * \exp[(G/k_BT) - (e\phi/k_BT)]) \qquad (2.15)$$

potential at the surface. We take the derivative of σ with respect to ϕ at infinite separation, Φ,

$$\mathrm{d} = \frac{\partial\sigma}{\partial\phi}|_{\phi=\Phi} \qquad (2.16)$$

which we solved for previously, and set this value equal to d. Taken together, we define the electrostatic potential, in k_BT, as a function of h, **eq 2.17**, where $\Delta = (\mathrm{d} - (\epsilon\epsilon_0\kappa))/(\mathrm{d} + (\epsilon\epsilon_0\kappa))$.

$$U_{es} = (\Phi^2/\Delta * \log[1 - (\Delta^2 \mathrm{e}^{-2\kappa h})] + (2\Phi^2/|\Delta|) * \arctan[|\Delta|\mathrm{e}^{-\kappa h}])\frac{\pi\epsilon\epsilon_0 r}{k_BT} \qquad (2.17)$$

Finally, the total interaction potential in k_BT, as a function of separation h, of two mercapto-alkanoic acid-capped QDs in a solution at some pH is calculated as **eq 2.1** and described in the main text.

$$U(h, pH) = U_{vdw}(h) + U_{es}(h, pH) + U_{hb}(h, pH) \qquad (2.1)$$

We convert the ligand shell-to-ligand shell separation, h, to center-to-center distance, d, by accounting for the radius, where $d = h + 2r$.

Table 2.1. Input Parameters for Calculating the Interparticle Energy between two PbS-DHLA QDs

	Description	Value (Units)
T	Temperature	298 (K)
k_B	Boltzmann's constant	1.38E-23 (J/K)
R_c	Radius of QD core	1.5E-9 (m)
r	Radius of QD + ligand shell	2.5E-9 (m)
A	Hamaker constant for PbS across water	4.98E-20
$\mathrm{Q_h}$	charge on hydrogen atom of water molecule (estimated from 0.24 e) [64]	0.4E-19 (C)
$\mathrm{u_d}$	The dipole strength of acetic acid (1.5 D) [64]	5E-30 (C*m)
ϵ	Relative permittivity of water	80
ϵ_0	Vacuum permittivity	8.854E-12 (F/m)
a	The minimal distance between two dipoles[50]	5E-10 (m)
Γ_0	Ligand density (assuming 85 bound ligands per QD, **Figure 2.11**)	3E18 (m^{-2})
$\mathrm{p}K_a$	For the carboxylate ligand tail (**Figure 2.9**)	8.6
χ_B	mole fraction of counter ions in solution (estimated from salt concentration)	.0018
G	free energy of ion dissociation in the absence of any external fields[48-50]	2.1E-20 (J)
$\mathrm{N_A}$	Avogadro' s number	6.022E23 (mol^{-1})
c_s	the monovalent salt concentration	100 (mol/m^3)
e	the elementary charge	1.602E-19 (C)

2.7.14 Deconvoluting PL spectra for Simulations

First, we identified three spectroscopically distinct populations of DHLA-capped QDs within the disaggregated (pH 12) sample by fitting the measured PL spectrum for this sample with three Gaussian curves, where the range of fwhm for each population was bound to approximate single PbS QD linewidths (50 -150 meV)[54]. The deconvoluted spectra serve as distinct QD populations within our simulations.

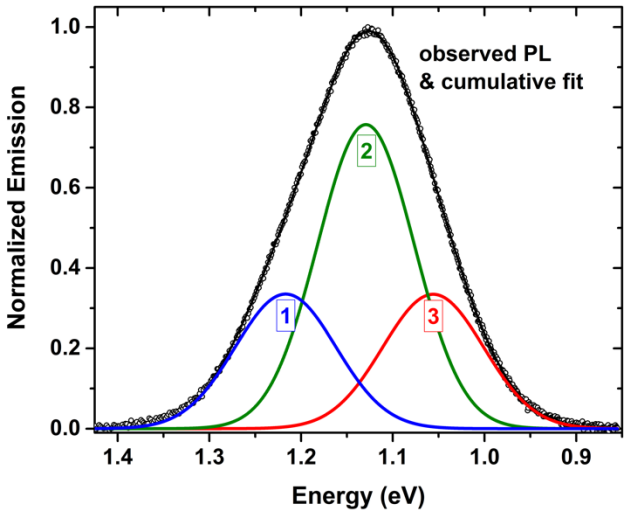

Figure 2.12. The observed PL for PbS-DHLA QDs at pH=12 (open circles) fit with three Gaussian curves (blue, green, and red traces labeled 1, 2, and 3). The sum of the three populations (black trace) agrees well with the experimental data.

2.7.15 Simulating PL Spectra as a Function of Average Interparticle Distance

We implemented an exciton hopping model similar to what we previously used to model the energy transfer within PbS QD assemblies.[43, 51] Our model simulates the ensemble PL spectrum as a function of *average* interparticle distance between all QDs in the ensemble, which accounts for both the presence of both loosely bound aggregates and more closely-packed structures (depending on pH), and is therefore more general than assuming a single interparticle distance within the aggregates and simply changing the population of QDs in the aggregates. The rate equation model (RE model) was governed by the master equation, **eq 2.2**, which allows for FRET between distinct populations of QDs as well

$$\frac{d}{dt}P_i(t) = P_i(t)\left\{-\frac{1}{\tau_i} - \sum_{j\neq i} k_{i,j}\right\} + \sum_{j\neq i} k_{j,i}P_j(t) \qquad (2.2)$$

as radiative/non-radiative relaxation of individual QDs. In **eq 2**, the population of each QD site is represented by $P_i(t)$; the QD sites decay by an intrinsic relaxation lifetime, τ_i, that reflects the

non-radiative and radiative relaxation and by EnT to nearby QDs. The rate of EnT from site *i* to site *j*, $k_{i,j}$, is determined using the Förster equation assuming the point-dipole approximation[43], where the spectral overlap is calculated between the deconvoluted QD PL spectra and the ensemble QD absorption. The radiative lifetime (900 ns) and fluorescence quantum yield (8.7%) are taken from our previously reported values for aqueous PbS QDs[43]. We assume $\kappa^2 = 2/3$ (valid for quasi-spherical QDs) and use a Maxwell-Garnett approximation to calculate the effective dielectric medium within the system.

First, we randomly generated 200 assemblies of 1000 QDs with a hexagonally close-packed structure, where we randomly assigned QDs to a sub-population based upon the results of the spectral deconvolution, as shown in **Figure 2.12**. We assume that these same three populations are present in the samples at every pH value, and propagate **eq 2.2** to determine how much each population fluoresces during the simulation time period (6 μs). We initialize the system by generating excitons in random locations within QD assemblies (on average, 10% of the QDs within each assembly is photoexcited) –assuming equal probability of excitation for each sub-population. To treat the non-radiative exciton decay pathways within the QDs, we randomly assign 91.3% of the QDs as "dark QDs" which have a fast non-radiative decay time constant of 50 ps. The remaining 8.7% of the QDs fluoresce with a radiative lifetime of 900 ns. For each QD assembly, we created a 1000 × 1000 matrix where element n_{ij} is the rate of FRET from QD *j* to QD *i*, and element n_{ii} represents the rate of radiative/non-radiative relaxation of QD *i*. We propagated the system in time with 10 ps steps for a total simulation time of 6 μs. The degree of aggregation is quantified in the model as average interparticle distance within the entire ensemble; this parameter ranges from the 4.0 nm (center-to-center) for the most aggregated sample, to >8× the diameter of

the QD for the most disaggregated sample. Our simulations were written using Python 2.7 using NumPy and SciPy libraries.

2.7.16ΔPL Weighted Avg. vs. PL fwhm

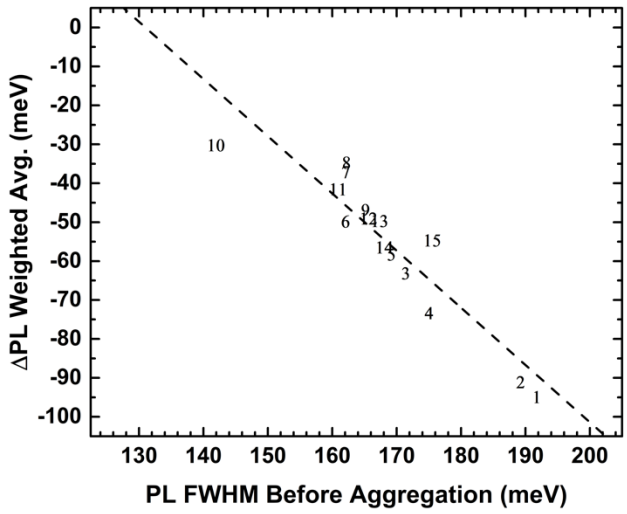

Figure 2.13. Figure 2.4 reformatted to show each titration experiment by number. **Table 2.2** contains the relevant parameters for each titration experiment.

Table 2.2. The experimental conditions for each PbS-DHLA QD titration experiment.

	PbS-OA batch, radius (nm)	DHLA equiv. (per QD)	[QD] (μM)	Solvent, ionic strength
1	Batch A, 1.48	420	5	H_2O
2	Batch A, 1.48	420	5	H_2O
3	Batch A, 1.48	420	1	H_2O
4	Batch A, 1.48	420	1	H_2O
5	Batch D, 1.72	420	1	H_2O
6	Batch D, 1.72	420	1	H_2O, 85.5 mM NaCl
7	Batch B, 1.48	100	1	D_2O
8	Batch B, 1.48	100	1	D_2O
9	Batch B, 1.48	420	1	D_2O, ionic strength ~0.01 M
10	Batch B, 1.57	420	1	D_2O
11	Batch C, 1.57	420	1	D_2O
12	Batch C, 1.57	420	1	D_2O
13	Batch C, 1.57	420	1	D_2O
14	Batch C, 1.57	420	1	D_2O
15	Batch C, 1.57	420	1	D_2O

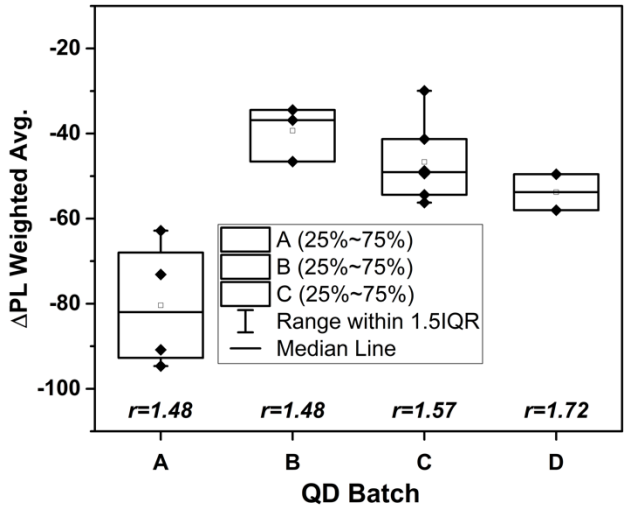

Figure 2.14. The ΔPL Weighted Avg. upon aggregation, for each DHLA exchange, sorted by the PbS-OA QD batch. Each batch corresponds to particular size (and inherent polydispersity/PL fwhm). A wide range of shifts are accessible within the same batch and there is no clear correlation between PL shift and QD size.

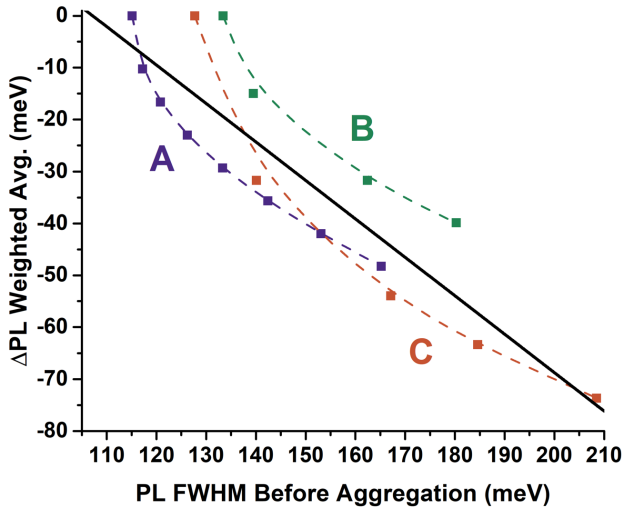

Figure 2.15. The calculated ΔPL Weighted Avg. for a given set of sub-populations (denoted A, B, and C) as a function of the PL fwhm before aggregation (solid squares, dashed lines). The concatenated linear fit of all points, shown for reference, is displayed as a solid black line.

We assume populations a, b & c (The highest energy population is "a", followed by "b" and "c") all share the same absorbance parameters. We fit half of the absorbance peak of experimental data to a single Gaussian in Origin and use this Gaussian curve, normalized to 1, as the absorbance spectrum. We fit the normalized experimental PL for the starting solution to three Gaussians (in Origin) and share the area of the three components. We hold the widths and amplitudes constant, but scale the separation between the emission of population a and the emission of populations b and c. We fix the ratio of the separation between a & b to a & c constant. We compute the resulting Gaussian curves representing emission from populations b and c over a wide range of separations. We compute the PL at the start of the titration (before aggregation, no EnT) by taking the sum of the emission of a, b, and c. We then use Förster EnT theory to compute the contribution of each population to the PL at the end of the titration (upon aggregation, distance of 4.5 nm). In our computation, EnT occurs from population a to population b or population c, and may also occur from population b to population c. We assume QY=10%, as well as assume that the areas and

widths of the emissive populations do not change. We employ experimentally relevant input parameters, such as QD concentration and molar absorptivity. Finally, we calculate the ΔPL Weighted Avg. upon aggregation for each set of populations. We export the computed PL into Origin, where we manually calculate the fwhm before aggregation.

Chapter 3: Structure and Mechanism of Aggregation of Dihydrolipoic Acid-Capped PbS Quantum Dots

Adapted From:

Schwabacher, J. C.; Redfern, K. A.; Weiss, E. A. *Unpublished work.*

3.1 Chapter Summary

This chapter describes the x-ray scattering profiles of PbS quantum dots (QDs) transferred from hexanes into water *via* displacement of native oleate ligands with dihydrolipoic acid (DHLA). Small-, mid-, and wide-angle x-ray scattering (SAXS/MAXS/WAXS) spectra of samples flowing at 20 μL/s through a quartz capillary were recorded simultaneously upon exposure to 9.0 keV x-rays. Following the system described in Chapter 2, we performed forward and reverse titrations ($12 \geq pH \geq 5$) using 0.5 M HCl and 0.5 M NaOH, respectively, to assess the structure and mechanism of formation of PbS-DHLA QD aggregates. Absorbance and photoluminescence (PL) spectra confirm that the QDs aggregate as the pH decreases below the pK_a of the PbS-DHLA system (=8.6), which results in an increase in the baseline of the absorbance spectrum and a bathochromic shift of the PL energy that is characteristic of energy transfer (EnT) between QDs in an aggregate. Distinct features at high q values in the x-ray scattering spectra of all samples correspond to spherical particles with an approximate radius of 1.79 nm. The x-ray scattering spectrum of the most aggregated sample (PbS-DHLA QDs at pH = 5) features a distinct peak at $q \sim 0.1$ Å^{-1}, which we attribute to closely packed QDs with an approximate center-to-center distance of 3.8 nm, as well as a correlation hole near $q \sim 0.11$ Å^{-1}. We use the correlation hole to calculate an estimated local volume fraction of 13 ± 2% and maximum 6-to-1 coordination for QDs in an aggregate. The scattering profile at pH = 5 also features an upturn at $q < 0.1$ Å^{-1}, which is attributed to the presence of relatively large fractal aggregates with a fractal dimension of 1.8–1.9. The scattering spectrum of the aggregated sample is well described by the diffusion-limited cluster aggregation (DLCA) and/or the reaction-limited cluster aggregation (RLCA) of polydisperse hard spheres into a mass fractal.

3.2 Introduction

Small-, mid-, and wide-angle x-ray scattering (SAXS/MAXS/WAXS) measurements are potent tools in the ever-expanding list of experimental techniques that characterize nanoparticles.[65] In SAXS/MAXS/WAXS techniques, an incident x-ray is elastically scattered by the atomic-shell electrons within an irradiated sample, and the intensities of the scattered x-rays are measured as a function of the scattering angle. The resulting intensity at a given angle is dependent on the electron density (number and distribution of electrons) of the experimental sample. SAXS/MAXS/WAXS measurements can provide information on structures as large as several micrometers (for ultra-small scattering angles) or as small as a few ångströms (for wide scattering angles) as determined by the range of detectable scattering angles.[66]

SAXS has been used to quantify the size of PbS QDs by fitting scattering spectra to hard-sphere structure factors with some polydispersity (*e.g.*, log-normal or Gaussian size distribution).[67-69] This method corroborates the sizes determined by electron microscopy and calibration curves coupled with absorbance spectra. In conjunction with small-angle neutron scattering (SANS), which is sensitive to organic capping ligands, SAXS can quantitatively characterize the entire QD structure (core, surface, and ligand shell).[68, 70] Similarly, x-ray diffraction (XRD) can provide information about the QD lattice.[67]

Beyond elucidating the structures of individual nanoparticles, scattering techniques provide information about assembly of nanoparticles in solution. SAXS has been used to characterize the assembly of nanoparticles into hierarchical structures[71], especially within polymer nanocomposites[72-75] and gold nanoparticle-based structures[76-77]. SAXS/WAXS measurements of PbS-OA QD supercrystals[78] formed by solvent evaporation revealed the orientation, lattice structure, and surface ligand conformation of the assembled QDs. A combination of

SAXS/MAXS/WAXS and SANS demonstrated that the addition of a non-solvent removes ligands from PbS QD surfaces, thus destabilizing the QDs and promoting the assembly of faceted supercrystals in organic solvents.[79] The relative miscibility of the non-solvent and native ligands determines the resulting supercrystal structure by altering the ligand shell's thickness and the QD's solvation.

We sought to understand the mechanism of aggregation and the structure of the aggregates formed when titrating 1 μM Dihydrolipoic acid (DLHA) capped-PbS QDs in water with 0.5 M HCl (from pH=12 to pH=5) using SAXS/MAX/WAXS measurements at the Advanced Photon Source (APS) at Argonne National Laboratory in Argonne, IL. There are two primary measurement methods for SAXS/MAXS/WAXS characterization of liquid samples: static capillaries and flow cells.[69] We first attempted static measurements of aqueous PbS-DHLA QDs in sealed quartz capillaries. However, we observed sample degradation (i.e., loss of distinct peaks and change in the general shape of the scattering signal) between scans, and proper subtraction of the capillary scattering spectrum was difficult since the thickness varies slightly from capillary to capillary. We, therefore, made a (separate) second attempt to characterize the PbS-DHLA QD system using a flow cell supplied by APS. The details of this successful second attempt, which deepen our understanding of the pH-responsive system investigated in Chapter 2, are described below.

3.3 Experimental Methods

3.3.1 Quantum Dot Synthesis and Ligand Exchange

We adapted a protocol from Hines *et al*.[8], as described in the previous chapter[80], to synthesize oleate-capped PbS quantum dots. We dissolved 0.36 g lead oxide (PbO, MilliporeSigma, 99.999%) in 20.05 ml solution of 19 mL of 1-octadecene (ODE, MilliporeSigma, 90%) and 1.05 mL of oleic

acid (OA, MilliporeSigma, 90%) in a 50 ml three-neck flask at 120 °C under N_2 atmosphere. We bubbled N_2 through the mixture while stirring at 120 °C for 30 min, and then at 150 °C for an additional 30 min. We stopped bubbling N_2 but maintained N_2 flow through the flask and cooled the reaction mixture to 110 °C. We used bis(trimethylsilyl)sulfide (TMS, MilliporeSigma) as the sulfur precursor. The precursor solution was prepared by dissolving 0.14 ml of TMS in 8 ml ODE that was purged with dry N_2 for 1 hour at ambient temperature while sonicating. We quickly injected the sulfur precursor into the solution of lead oleate at 110 °C and immediately removed the heating mantle. Once the solution cooled < 50 °C, the reaction mixture was divided into four 50-mL centrifuge tubes. We added 40 mL of acetone to each centrifuge tube and shook the mixture to wash the PbS QDs. We centrifuged the mixture at 3500 rpm for 20 min. After removing the supernatant and drying the pellet with N_2, we resuspended the QDs in minimal hexanes. We repeated the washing process again by adding 40 mL of methanol and centrifuging at 3500 rpm for 20 min. We dried the resulting pellet and resuspended it with a small amount of hexanes, added 50 mL of methanol, centrifuged at 3500 rpm for 20 min a third time. We repeated the washing procedure for a final (fourth) time with acetone. After the QD pellets were dried under N_2 flow, they were dispersed in hexanes. We stored the PbS-OA QD stock in the dark and sealed under N_2 atmosphere.

Ligand exchange and sample preparation was conducted under a nitrogen atmosphere with degassed solvents to minimize oxidation of the QD surfaces and their ligands. Milli-Q water (18.2 MΩ·cm at 25 °C) was used for all aqueous solutions. Solutions were purged of air by bubbling with dry N_2 while submerged in a sonicating bath as previously reported.[80]

We prepared water-soluble PbS QDs capped with DHLA as described Chapter 2, which was adapted from Deng *et al*.[61] DHLA for was prepared from lipoic acid following the procedure

outlined by Uyeda *et al*.[60] Briefly, lipoic acid was dissolved in 0.25 M $NaHCO_3$ and cooled in an ice bath. $NaBH_4$ was added slowly while stirring 2 h below 4 °C. The reaction mixture was acidified with 6 M HCl to pH = 1, extracted with toluene, and dried over $MgSO_4$. After evaporation of the solvent, the desired product was a clear colorless oil that was stored in the dark in a refrigerator. ^{1}HNMR ($CDCl_3$): δ 10.5 (bs, 1H), 2.93 (m, 1H), 2.71 (m, 2H), 2.38 (t, J = 7.3 Hz, 2H), 2.0–1.4 (m, 8H), 1.35 (t, J = 8.0, 1H), 1.30 (d, J = 7.6, 1H).

We added 4 μL of DHLA to 5 mL of 15 μM PbS-OA QDs in $CHCl_3$ in a 15-mL centrifuge tube (420 DHLA equiv. per QD). We then added 30 μL of 0.5 M NaOH (1.7 equiv. per DHLA), followed immediately by 5 mL of degassed H_2O, and vigorously shake the tube for five seconds. We opened the tube and added an additional 70 μL of 0.5 M NaOH (4.0 equiv. per ligand), re-sealed the tube, and then shook the tube by hand for approximately three minutes until a clear black layer formed at the top of the beige solution in the centrifuge tube. We centrifuged the mixture at 7500 RPM for 5 minutes, after which we carefully removed the top (dark brown) aqueous layer with a syringe and filtered the solution into a clean vial using a syringe filter (0.22 μm pore size). The resulting ~10 μM aqueous QD dispersions are basic (pH ~ 10.5 pH) after exchange.

3.3.1 Sizing of PbS QDs via Ground State Absorption

All ground state absorption spectra were obtained on a Varian Cary 5000 spectrometer using a 2 mm/10 mm dual pathlength quartz cuvette. We excited our samples along the 2 mm axis and corrected the baselines with solvent blanks prior to measurement. We collected the absorption spectra for the synthesized PbS-OA QDs and determined their size from the position of the first excitonic peak using the calibration curve published by Moreels *et al.*[58], a method that we

previously corroborated[59] *via* TEM. All concentrations of QDs were calculated from the absorbance of QDs at 400 nm.

3.3.2 Photoluminescence Measurements

The photoluminescence (PL) spectra were measured with a Horiba Fluorolog-3 spectrofluorometer using a right-angle geometry and a 2 mm/10mm dual-pathlength cuvette. The excitation beam (λ=825 nm) was applied along the 10-mm path of the cuvette and the sample emission was collected along the 2-mm path. The excitation and emission slit widths were 5 nm.

3.3.3 Calculating PL fwhm

The PL full width at half maximum (fwhm) was manually calculated for each PL spectrum by taking the difference in energy for the two points that were half the maximum emission intensity.

3.3.4 Sample Preparation

Before arriving at the Advanced Photon Source in Argonne, IL, we adjusted the pH of a 1 μM solution of PbS-DHLA QDs (total volume = 40 mL) from 10.4, the condition after phase transfer, to 12 using 600 μL of 0.5 M NaOH. We then titrated the sample with 0.5 M HCl and measured the absorbance and emission spectrum of the ensemble at pH = 11.8, 11.1, 9.57, 8.4 and 5.2 titration points, hereto referred to as pH = 12, 11, 10, 8 and 5. At each of these points of interest in the titration, a 2-mL aliquot of the solution was removed under an inert (Nitrogen) atmosphere and sealed. We performed the same characterization procedure for a reverse titration using the addition of 0.5 M NaOH to raise the pH = 5 sample to pH = 9.87 and pH = 11.24, which we refer to as pH = 10 and 11 when discussing the reverse titration. A control sample (sometimes referred to as a buffer or blank) of DHLA in water was prepared by conducting the exchange procedure without QDs and diluting the resulting aqueous layer ten times to mimic the dilution performed for the titration. The aliquots and buffer were stored in the dark until their x-ray scattering profiles were

measured approximately 24 hours later. Samples of 1 μM PbS QDs capped with oleic acid (OA) in hexanes and pure hexanes solvent were also transported to APS.

3.3.5 X-ray Scattering Measurements

Synchrotron x-ray measurements were performed at the DuPont-Northwestern-Dow Collaborative Access Team (DND-CAT) located at Sector 5 of the Advanced Photon Source (APS). DND-CAT is supported by Northwestern University, The Dow Chemical Company, and DuPont de Nemours, Inc. This research used resources of the Advanced Photon Source, a U.S. Department of Energy (DOE) Office of Science User Facility operated for the DOE Office of Science by Argonne National Laboratory under Contract No. DE-AC02-06CH11357. Data was collected using an instrument funded by the National Science Foundation under Award Number 0960140.

After transporting samples to APS, we performed simultaneous SAXS/MAXS/WAXS measurements under flow using the beamline-supplied flow cell set up with a 1.50-mm diameter quartz capillary (Charles Supper Company) at room temperature. While applying an x-ray energy of 9.0 keV, 8 consecutive frames (3 s of exposure per frame and 5.15 s wait-time between each frame) were collected while 950 μL of sample passed through the beam with unidirectional continual flow of 20 μL/s. SAXS, MAXS, and WAXS 2D patterns were collected simultaneously on a custom triple-detector system consisting of three Rayonix fast-frame CCD detectors. Calibrations were performed by measuring a glassy carbon sample, the empty capillary cell, and the cell filled with Millipore water. The cell was cleaned between samples by flowing 2.5 mL of 0.5 M NaOH, 2.5 mL of soap solution, and then 5 mL of water through the capillary. Before the measurement of each sample, the scattering spectrum of the cleaned, empty capillary was measured, followed by the scattering spectrum of the buffer (dilute DHLA in water). The capillary

was rinsed with ethanol and acetone before measuring the sample of PbS-OA QDs in hexanes, and hexanes was used as the buffer solution. Calibration and data reduction were performed at the beamline using beamline-supplied custom code on a Linux-based system.

To obtain the scattering contribution of only the PbS QDs, the scattering contribution of the buffer in the rinsed capillary was subtracted from the scattering profile of the experimental sample for each measurement. Measurements from each detector were merged after background subtraction using Irena for Igor with Igor Pro 8.[81] Data analysis and fitting were performed using SASfit[82] and Origin(Pro), Version 2016.

3.4 Results and Discussion

The impacts of the phase transfer process on PbS-OA QDs, as suggested by changes in absorbance, PL, and x-ray scattering spectra, are discussed below, followed by a discussion of the effects of the forward and reverse titrations on a 1 μM solution of PbS-DHLA QDs. We use a detailed analysis of the scattering profile of the aggregated sample (pH=5) to expand our description of PbS-DHLA QDs first introduced in Chapter 2.

3.4.1 Impacts of Phase Transfer

Figure 3.1 displays the absorbance and emission spectra PbS QDs before and after phase transfer. The native oleate-capped QDs have absorbance and emission maxima at 1.2912 eV and 1.1481 eV, respectively, with a PL fwhm of 155 meV. The QDs have a radius of 1.57 nm, which was calculated using the absorbance and emission spectra of the PbS-OA QDs before phase transfer.[80] Upon ligand exchange and subsequent phase transfer into water using DHLA, the absorbance and emission maxima undergo bathochromic shifts to 1.2338 eV and 1.1071 eV, respectively, along with a slight broadening of the PL fwhm to 158 meV and an 82% decrease in PL intensity, as expected.[80, 83-84] Aliquots of the solutions characterized in **Figure 3.1** were stored

in the dark under a N_2 atmosphere and further characterized using x-ray scattering measurements 24 hours later.

The x-ray scattering profiles of 1 μM PbS-OA QDs in hexanes and 1 μM PbS-DHLA QDs in water (pH=10.4) are shown in **Figure 3.2**. Both spectra feature a prominent peak near $q = 0.3$ Å^{-1}, which is likely contributed from a spherical form factor with an approximate radius of 1–2 nm.[85] We attribute this feature to the individual QDs present in solution, which fall within that size range. The scattering profile of the PbS-OA QDs in hexanes relatively flattens at $q < 0.05$ Å^{-1} (**Figure 3.2**, black trace), which is qualitatively similar to the scattering profile of a dilute solution of non-interacting spheres.[85] The scattering profile notably changes upon ligand exchange and phase transfer for $q < 0.2$ Å^{-1}, but the peak near $q = 0.3$ Å^{-1} remains (**Figure 3.2**, purple trace). The increase in the slope and intensity of scattering signal at low-q values suggests that larger structures may have formed.[85] We expect that some degradation and subsequent aggregation of our aqueous QDs occurs during overnight storage and/or upon loading into the flow-cell capillary under air.

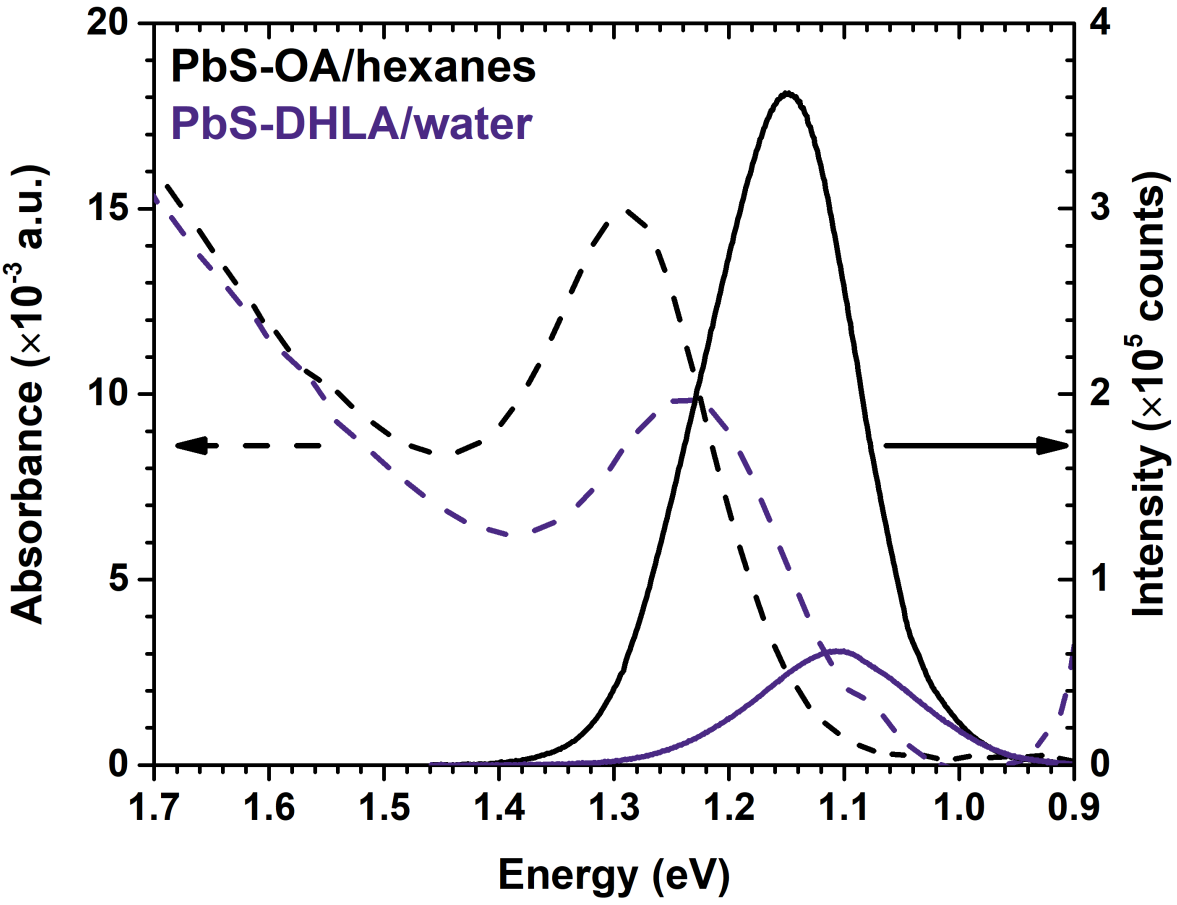

Figure 3.1. Absorbance (dashed, left *y*-axis) and emission (solid, right *y*-axis) spectra, for PbS QDs before and after phase transfer from hexanes (black, oleate-capped QDs) to water (purple, DHLA-capped QDs, pH=10.4).

We also note the apparent suppression of the scattering profile upon phase transfer between q ~ 0.04–0.4 Å^{-1}. The responsiveness of these features to changes in pH, and their subsequent implications, are discussed below.

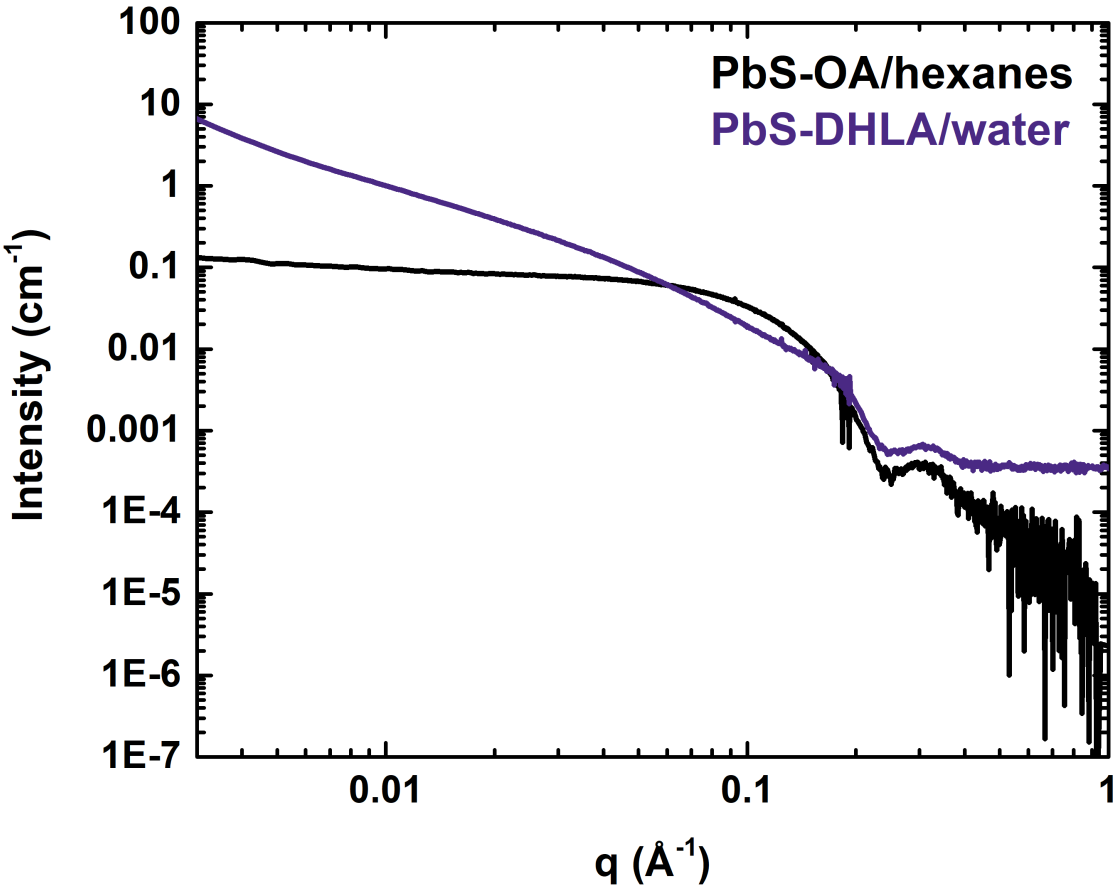

Figure 3.2. X-ray scattering measurements of 1 μM PbS-OA QDs in hexanes (black trace) and 1 μM PbS-DHLA QDs in water at pH = 10.4 (purple trace).

3.4.2 Forward Titration

We adjusted the pH of a 1 μM solution of PbS-DHLA QDs from 10.4, the condition after phase transfer, to 12 using 0.5 M NaOH. We then titrated the sample with 0.5 M HCl and measured the absorbance and emission spectrum of the ensemble at pH = 11.8, 11.1, 9.57, 8.4 and 5.2 titration points, referred to as pH = 12, 11, 10, 8 and 5, **Figure 3.3**. This range spans the pK_a of the free thiol (=10.3) and the carboxylic acid of DHLA when bound to the QD (=8.6, see section 2.7).[80] At each of these points of interest in the titration, an aliquot of the solution was removed. The aliquots

were stored in the dark under an inert atmosphere until their x-ray scattering profiles were measured 24 hours later.

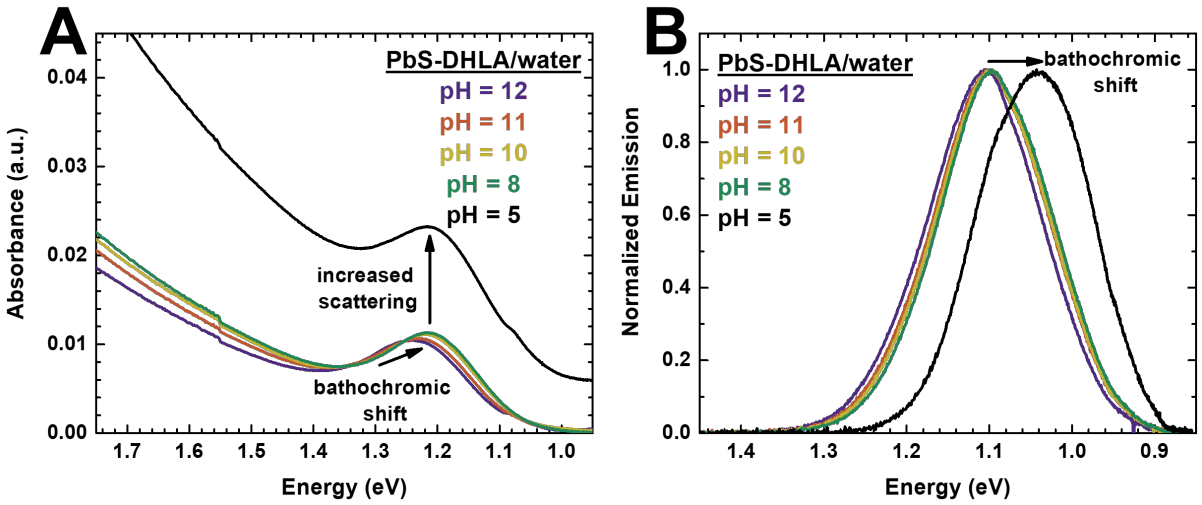

Figure 3.3. Absorbance (**A**) and emission (**B**) spectra of aqueous of 1 μM PbS-DHLA QDs titrated with 0.5 M HCl. Measurements were performed for pH values of 12, 11, 10, 8 and 5 (purple, orange, yellow, green, and black solid lines, respectively). The addition of HCl induced a bathochromic shift in both the absorbance and emission peaks, as well as a significant increase in the absorption spectrum baseline upon approaching pH=5, as indicated by the arrows.

Figure 3.3A illustrates the bathochromic shift of the absorbance peak (~28 meV) from 1.2450 eV to 1.2169 eV that occurs as the pH is decreased from 12 to 8. A significant increase in the baseline, and a small decrease of the absorbance peak energy (~2.4 meV) to 1.2145 eV occurs as the pH jumps from 8 to 5, which we attribute to the increased scattering from acid-induced aggregates present when pH < 6, as noted previously (see section 2.5).[80] **Figure 3.3B** depicts the bathochromic shift of the PL spectrum as the pH decreases. The sample has a PL weighted average of 1.0998 eV at the start of the titration (pH=12) that decreases 59.7 meV to 1.0401 eV by the end of the titration (pH=5). Based on our previous work[80] described in section 2.5, we would expect a population of DHLA-capped PbS QDs with a PL fwhm of ~160 meV to exhibit a bathochromic PL shift of ~45 meV on going from a pH ≥ 10.7 to a pH ≤ 6; thus the 51 meV decrease on going

from pH = 11 to pH = 5 in this sample aligns well with our previous report. The greatest change in the PL weighted average between two titration points, 45.7 meV, occurs as the pH is decreased from 8 to 5, which corresponds to the greatest increase in the absorbance baseline. This result was also observed previously (see section 2.5).[80]

The x-ray scattering profile of the 1 μM PbS-DHLA QDs at each titration point, **Figure 3.4**, prominently features the peak near q = 0.3 Å^{-1}, which we attribute to the spherical form factor of the QDs in the sample. The inset in **Figure 3.4** highlights the suppression of the signal between q ~ 0.04–0.4 Å^{-1}, which occurs as the pH decreases. Within this q region, the trace for the sample when pH = 12 overlays the trace when pH = 11, and the trace when pH = 10 overlays the trace when pH = 8. The maximum suppression for our sample was observed when pH = 5, which is also when a shoulder-like peak at q ~ 0.165 Å^{-1} is formed. This suppression has been attributed interference between the x-rays scattered from the individual particles present when spherical particles aggregate or when the average density of the measured sample is at least one-third of the system's close packing density.[86] Simulated scattering profiles of Pd nanoparticles also suggest the presence of scattering interference accompanying a shoulder-like peak when tightly-packed clusters are formed.[87] Others have attributed this suppression to the repulsive interactions between nanoparticles[88] and agree that this suppression is characteristic of an aggregated system. We attribute the peak at q ~ 0.165 Å^{-1} to the ordering of QDs within an aggregate with a center-to-center distance (=$2\pi/q$)[89] of approximately 3.8 nm. This result is in reasonable agreement 4.5 nm, the average center-to-center distance for the ensemble that simulates the PL when pH = 5 (see section 2.5).[80]

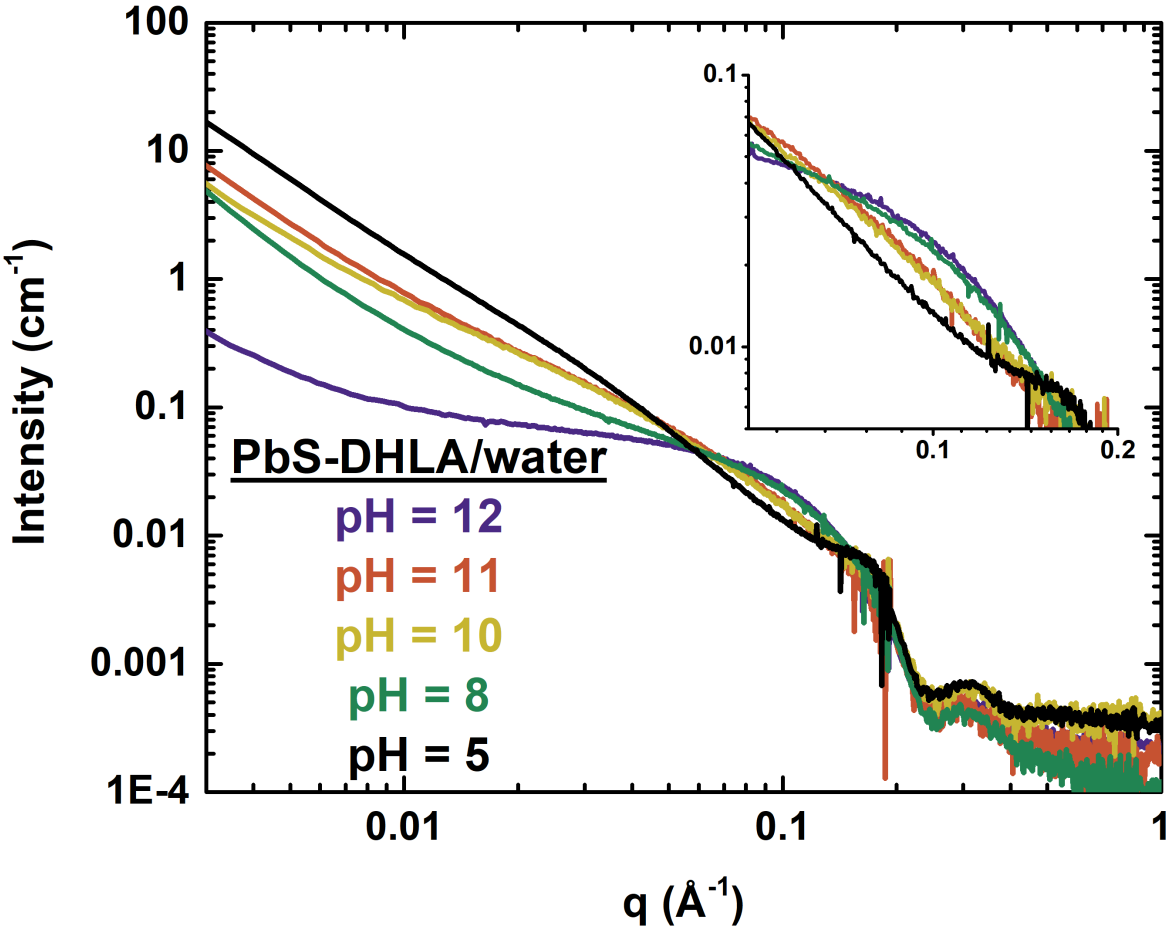

Figure 3.4. X-ray scattering spectra (intensity, cm^{-1}, *vs* q, $Å^{-1}$) of aliquots of 1 μM PbS-DHLA QDs in water titrated with 0.5 M HCl. The samples reflect the same batch of aqueous QDs at pH values of 12, 11, 10, 8 and 5 (purple, orange, yellow, green, and black traces, respectively). The inset displays the suppression of the signal between $q \sim 0.04–0.4$ $Å^{-1}$, which occurs when pH=5.

3.4.3 Reverse Titration

We performed a reverse titration of the PbS-DHLA QDs using 0.05 M NaOH to adjust the

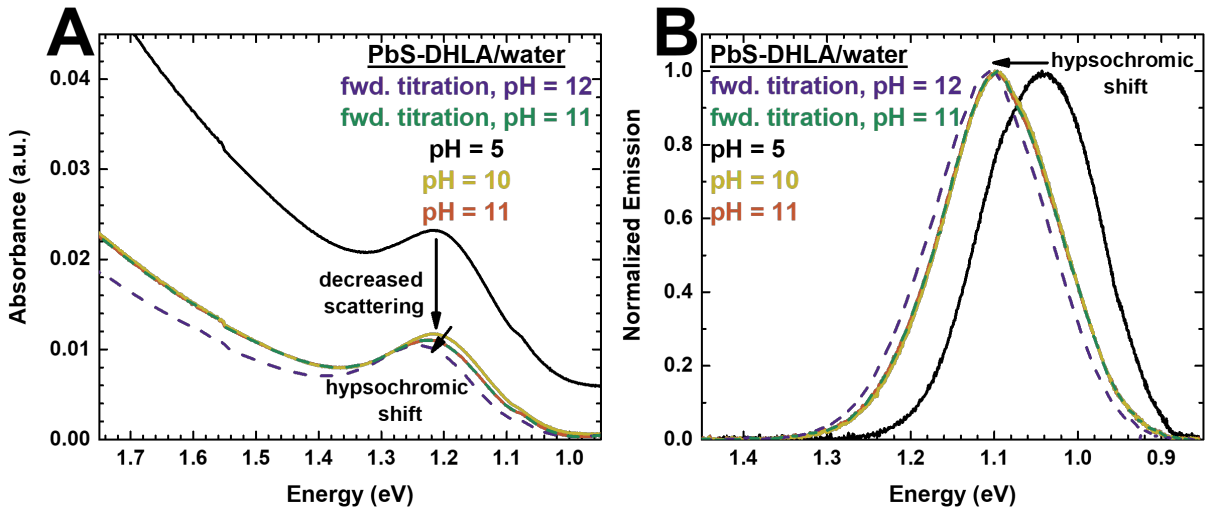

Figure 3.5. Absorbance (**A**) and emission (**B**) spectra of the reverse titration of the aqueous 1 μM PbS-DHLA QD sample from **Figure 3.1**. The reverse titration was performed by the addition of 0.5 M NaOH. The addition of NaOH induces a hypsochromic shift in the emission spectrum peak, as well as a significant decrease in the absorption spectrum baseline, as indicated by the included arrows. The addition of NaOH also partially reverses the bathochromic shift in the absorption spectrum peak that occurs upon the forward titration.

sample from pH = 5 to pH = 10, and to a final condition of pH = 11. The absorbance and PL spectra were recorded for each condition, and aliquots were stored in the dark under an inert atmosphere until their x-ray scattering profiles were measured approximately 24 hours later. The absorbance, **Figure 3.3A**, and PL spectra, **Figure 3.3B**, for the reverse titration reasonably resemble the absorbance and PL spectra for the basic points of the forward titration as the sample is adjusted from pH = 5 to pH = 10. Specifically, the absorbance baseline decreases as the pH increases, the absorbance peak shift reverses ~2.4 meV, and the PL weighted average undergoes a hypsochromic shift from 1.0401 eV to 1.0876 eV. While there is no discernable difference between the normalized PL spectra when the pH = 10 and pH = 11 during the reverse titration, there is a small

but clear hypsochromic shift in the absorbance peak (~3.6 meV), from 1.2169 eV to 1.2205 eV. There is a hysteresis of 3.9 meV of the PL weighted average for the emission spectra when pH = 11 for the forward and reverse titration, and a hysteresis of 12.2 meV between the start point of the forward titration (pH=12) and the end point of the reverse titration (pH=11). The absorbance and emission spectra for the forward and reverse titrations of PbS-DHLA QDs in water also follow our previous report, as we also

The x-ray scattering spectrum of the PbS-DHLA QD sample undergoing a reverse titration from pH = 5 to pH = 11 also exhibits a reverse of the features that formed during the forward titration. In particular, the scattering profile between $q \sim 0.04–0.4$ grows back in and the shoulder at $q \sim 0.165$ Å^{-1} disappears as the pH of the solution is adjusted from 5 to 10, which suggest that the QD packing is loosened as the pH is increased. There is no discernable difference between the x-ray scattering spectra for the pH = 10 and pH = 11 samples in the range of $q \sim 0.04–0.4$ Å^{-1}, which intimates that the change in QD packing occurs during the first jump from pH = 5 to pH = 10. The persistence of the upturn at low-q values across all samples suggests that some aggregation is irreversible.

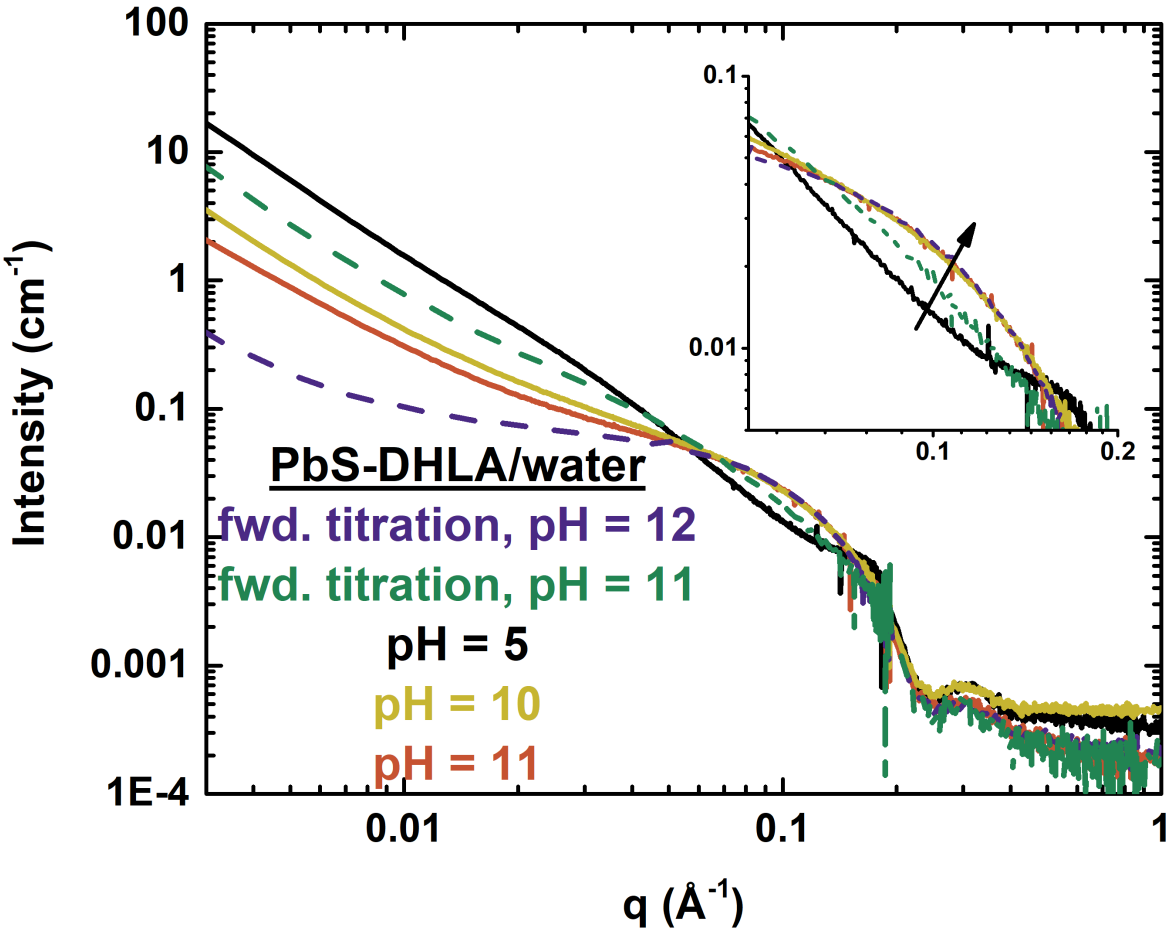

Figure 3.6. X-ray scattering spectra (intensity, cm^{-1}, *vs* q, $Å^{-1}$) of aliquots of 1 μM PbS-DHLA QDs in water titrated with 0.5 M NaOH to bring the same sample of QDs from pH = 5 (black trace) to pH = 10 (yellow trace) and pH = 11 (orange trace). The inset and accompanying arrow highlights the return of the signal between q ~ 0.04–0.4 that occurs as the pH increases. The scattering profiles for the forward titration when pH = 12 (dashed purple trace) and pH = 11 (dashed green trace) are shown for comparison.

3.4.4 Identifying the Mechanism of Aggregation and Higher-Order Structures

We assume the scattering profile of PbS-DHLA QDs is dominated by individual particles at pH = 12 and fit this profile to a spherical form factor with lognormal polydispersity and an optimized mean radius of 17.85 Å. Given that the absorbance spectrum of the as-synthesized QDs

suggests a radius of 1.57 nm, that QD sizes determined by SAXS are known to be larger than QD sizes determined by absorbance/TEM[69], and that the exchange procedure introduces an additional layer of sulfur atoms to each QD as DHLA molecules bind, an increase of up to 3 Å for the radius of the QD core is expected[90]; thus, 17.85 Å is reasonable. We fix the particle concentration to that of our experimental sample (1 μM) and include a flat background of 0.0023 a.u. to account for the baseline at high q. We allow the polydispersity, σ, and scaling factor, η, to float and select a fit range of 0.1–1 $Å^{-1}$. **Figure 3.7** shows the spherical form factor determined from the fit to the scattering profile for PbS-DHLA QDs at pH = 12 with our given input parameters. The spherical form factor deviates from the scattering profile as q decreases, which suggests that this fit underestimates the polydispersity of the system. As previously stated, the upturn at low q suggests that aggregation had occurred by the time the measurement was performed, which would further increase the deviation of the scattering profile of the experimental sample from a fit to the scattering profile of one population of polydisperse hard spheres.

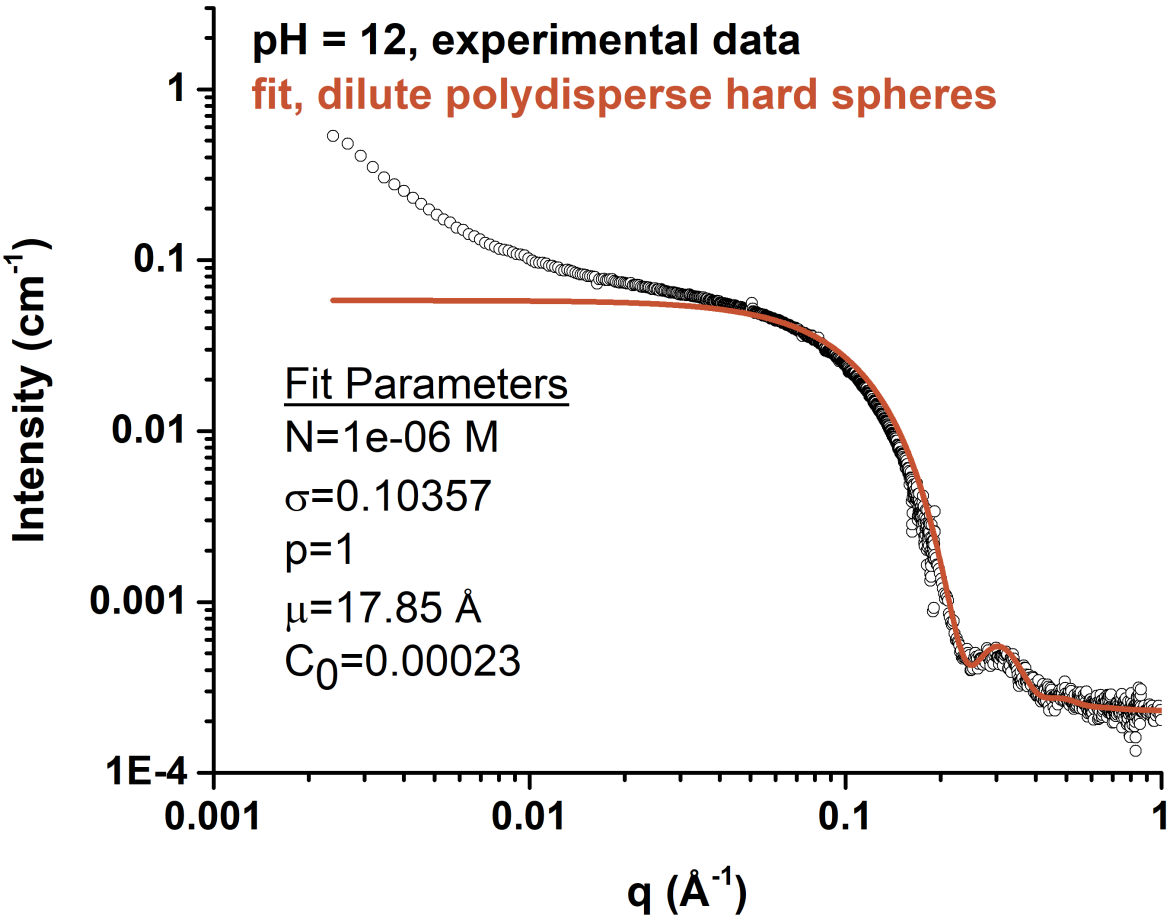

Figure 3.7. X-ray scattering spectra (intensity, cm^{-1}, *vs* *q*, $Å^{-1}$) of aliquots of 1 μM PbS-DHLA QDs in water titrated with 0.5 M NaOH to bring the same sample of QDs from pH = 5 (black trace) to pH = 10 (yellow trace) and pH = 11 (orange trace). The inset and accompanying arrow highlights the return of the signal between $q \sim 0.04$–0.4 that occurs as the pH increases. The scattering profiles for the forward titration when pH = 12 (dashed purple trace) and pH = 11 (dashed green trace) are shown for comparison.

Following the work of Genix *et al*., we use the estimated spherical form factor with lognormal polydispersity to quantify the suppression of the scattering intensity that arises from aggregation at pH = 5.[88] **Figure 3.8**, which results from dividing the scattering profiles at each pH (see Figure 3.4) by the spherical form factor (solid trace, Figure 3.7), prominently illustrates the correlation

hole that arises when pH = 5. The depth of this hole, 0.48 a.u., corresponds to a compacity (volume fraction), κ, of 13 ± 2%, where the error is estimated to be %15 of the calculated value.[88]

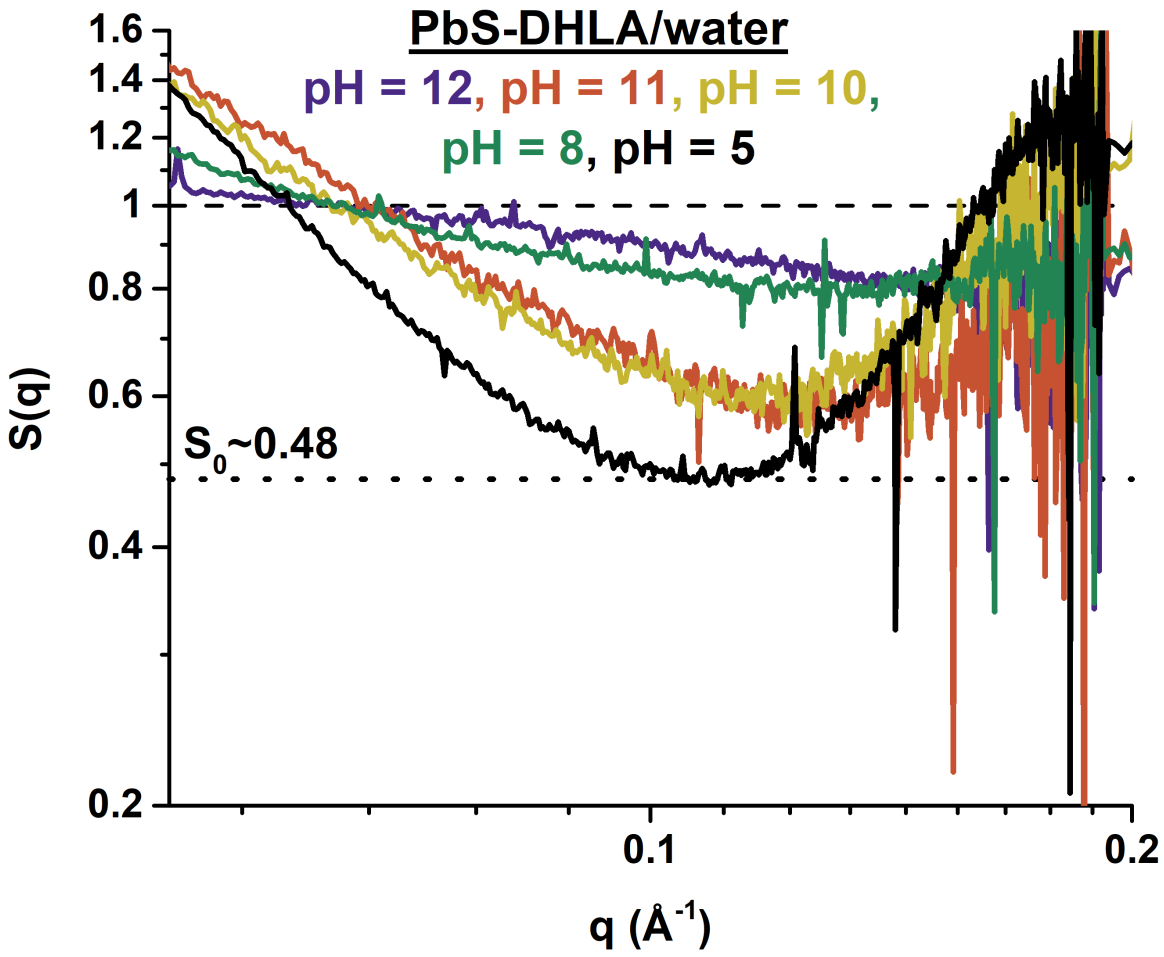

Figure 3.8. The structure factor, S(q), arbitrary units, of 1 μM PbS-DHLA QDs in water at pH = 12, 11, 10, 8, and 5 (purple, orange, yellow, green, and black traces, respectively). S(q) was calculated by dividing the net measured scattering profile of each sample by the spherical form factor. The spherical form factor was estimated by fitting the sample of dispersed QDs (pH=12). The dashed line at S(q) = 1 is a guide to highlight the deviation from the spherical form factor for non-aggregated polydisperse hard spheres. The correlation hole, which appears at q ~ 0.11 Å^{-1}, has a minimum value S_0 ~ 0.48 a.u., as illustrated by the dotted line, which corresponds to a volume fraction, κ, of 13 ± 2%.

This means that local density within an aggregate of QDs is approximately 13% on the scale of the first coordination shell. Following the approximation made by Genix *et al.* that the first

coordination shell is contained within a cube with a side that is 6 times larger than the radius of one nanoparticle[88], there are approximately 7 QDs per cube, which suggests maximum coordination of 6 to 1 for aggregated particles. The coordination may be less than 6 to 1, since the average local density described here will include distributions of aggregates of different sizes, including aggregates that coexist with isolated QDs.[71, 88] For complete details, see section 3.7.

To better understand the structure of the aggregates formed, we fit the x-ray scattering profile for PbS-DHLA QDs at pH = 5. **Figure 3.9** displays the scattering profile of the PbS-DHLA QD aggregates (pH=5, black open circles) fit to a model consisting of a flat background component = 0.00047 a.u. (dashed yellow trace), a polydisperse hard-sphere component with the Percus-Yevick closure (HSPY)[91-92] (solid orange trace), and a mass fractal aggregate component described by the Beaucage model[93-94] (solid green trace). For each component's contribution before the background is added, see section 3.7. The HSPY component was fit with a fixed particle radius of 17.85 Å and a log-normal polydispersity (p=1, σ=0.1, μ=17.85 Å) taken from the optimized fit of the dispersed sample (pH=12), while the volume fraction and concentration (N, which serves as a scaling factor in this particular case) were allowed to float. The resulting volume fraction was determined to be ≈ 0.33. **Figure 3.9** demonstrates that the HSPY component agrees well the measured scattering profile and reproduces both the form-factor peak at $q \sim 0.3$ Å^{-1} and the close-packing peak at $q \sim 0.165$ Å^{-1}. The HSPY scattering component levels off at $q < 0.1$ Å^{-1}, and thus can only account for the scattering in the high-q region.

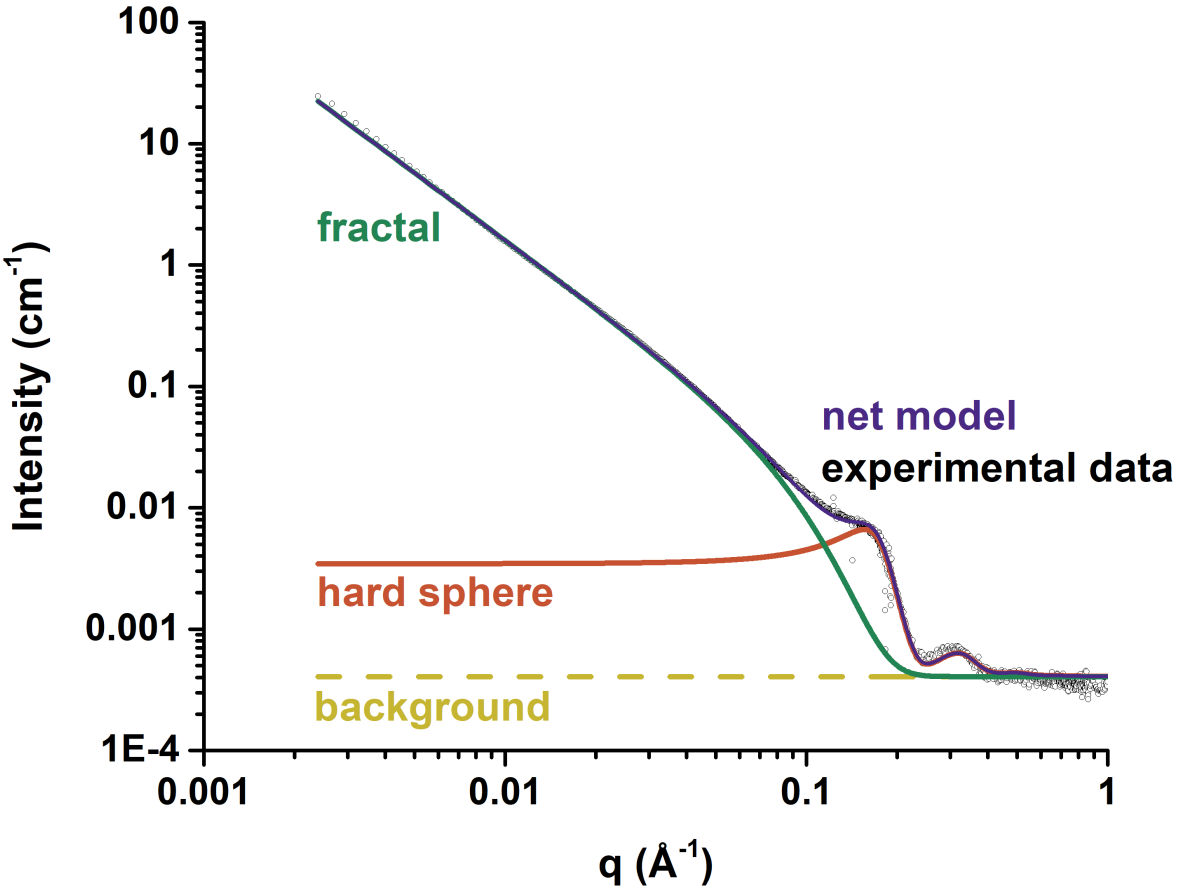

Figure 3.9. X-ray scattering spectra (intensity, cm^{-1}, *vs* *q*, $Å^{-1}$) of 1 μM PbS-DHLA QDs in water at pH = 5 (black open circles) fit with a model (purple trace) consisting of mass fractal aggregates (green trace) made up of hard spheres with log-normal polydispersity. The flat background component is displayed (yellow dashed trace).

For the Beaucage model component, the Guinier pre-factor of the aggregate, G, was arbitrarily fixed = 1. The radius of gyration of the aggregate, Rg_i, was arbitrarily fixed = 10,000 Å to account for the fact that aggregates grow larger than the scale of objects measured by this method and eventually precipitate from solution. The radius of gyration of the subunit, Rg_{i+1}, was fixed to the previously determined QD radius (17.85 Å) for simplicity. The power-law scattering pre-factor, B, and the power-law scaling component, P, were allowed to float. The constant k was fixed = 1.06, as suggested by the literature for systems with weak power-law decays (P<3).[93] The best fit

was determined to correspond to B = 0.000339715 and P = 1.83752. The resulting fractal component (solid green trace, Figure 3.9) agrees well with the experimentally measured scattering profile at low-q values. At $q < 0.1$ Å^{-1}, the contribution from the HSPY component diminishes, and the contribution from the fractal component dominates.

The fractal dimension, d_f, suggested by the power-law scaling component from the fit ($d_f = P \approx 1.84$) indicates that either diffusion-limited cluster aggregation[95-96] (DLCA, $d_f = 1.8$) or reaction-limited cluster aggregation[97] (RLCA, $d_f = 1.9–2.1$) occurs as the pH decreases to 5.[98] We also fit the low-q region to of the experimentally measured scattering spectrum to a power-law function, $I(q) = aq^b$, where $d_f = |b| \approx 1.9$ (see section 3.7), which further supports an aggregation mechanism within the DLCA—RLCA regime. In DLCA, colloids diffuse through solution and aggregate irreversibly upon contact. Individual colloids or smaller clusters continue to spread and collide, eventually growing into larger aggregates with fractal structures. The RLCA model is similar to the DLCA model but asserts that the colloids will irreversibly aggregate upon contact with some probability, not every collision, that is determined by interparticle repulsion strength. In general, DLCA results in structures that are more open than structures formed through RLCA because clusters participating in RLCA have some probability of interpenetrating each other upon collision.[97]

Our analysis, overall, suggest that PbS-DHLA QDs aggregate and form large fractal structures as the pH decreases below the pK_a of the DHLA-coated QD surface (=8.6). The structures produced when pH = 5 may be approximated as polydisperse hard spheres that pack as close as one QD diameter within local clusters. Since a volume of approximately one coordination shell contains roughly 7 QDs, there is likely no more than 6 QDs coordinated to one QD, which suggests a simple cubic packing structure. The volume fraction estimated by the HSPY model, however, is

only 0.33 and not 0.52, which indicates a diamond-like (or Zinc-blende like) packing structure[99], and that, on average, as few as 4 QDs may be coordinated to one QD. The DHLA ligands likely take up some space within a given volume of the experimental sample and will lower the density of the inorganic PbS QD core that provides the SAXS/MAXS/WAXS signal, which will, in turn, lead to an underestimation of the QD packing density *via* these methods.

The fractal dimension of the aggregated system, as determined by fitting the experimental scattering profile using a Beaucage model and a simple power-law function, is ~ 1.8–1.9. Given this d_f range, either DLCA or RLCA may dominate. The PbS-DHLA QD system likely experiences both DLCA and RLCA as the titration is performed. At the start of the titration (pH > pK_a=8.6), the QDs experience significant interparticle repulsion that inhibits aggregation (see Chapter 2).[80] As the pH decreases and approaches the pK_a of the system, the interparticle repulsion decreases and the probability of aggregating upon collision increases, as described by the RLCA model. As the pH decreases further (pH < pK_a=8.6), the interparticle repulsion becomes negligible, attractive interparticle forces dominate, and the probability of aggregating upon collision approaches unity, which is described by the DLCA model. Therefore, both RLCA and DLCA mechanisms may influence structures formed at pH = 5, and thus those structures have a fractal dimension that falls on the cusp of the two regimes.

3.5 Limitations and Future Directions

The wealth of information and insight regarding structures across relatively large length scales in solution makes simultaneous SAXS/MAXS/WAXS measurements a powerful tool to investigate the aggregation of QDs. Despite the amount of information gleaned from relatively few samples, the generalizability and reproducibility of this particular study remain unclear. Though this PbS-DHLA sample has a pH-response similar to the collection of samples reported

previously[80], discrepancies exist: i) a 3% increase in PL fwhm on titrating to pH = 5, rather than the 20% decrease in PL fwhm reported earlier; ii) a lack of dependence of the emission intensity of the sample on pH when pH ≥ 9; and iii) a noticeable bathochromic shift in the first absorption maximum as pH decreases, which was absent across the extensive collection of experiments described in Chapter 2. Future work, therefore, should focus on repeating these SAXS/MAXS/WAXS, absorbance, and PL measurements and analyses for multiple exchanges with the same batch of QDs, as well as across multiple batches of QDs.

It is also important to note that the compacity analysis included in section 3.4.4 is not suitable for describing density across large fractal aggregates, since density will decrease with size (in this case), nor is it appropriate for describing the density of linear aggregates.[88] Thus, it is important not to conclude the density of the larger structures from this analysis. Furthermore, to confirm that this analysis accurately applies to the PbS-DHLA QD system, some other measurement of aggregate shape is needed.

Liquid-phase electron microscopy (LP EM) and/or cryogenic electron microscopy (cryo-EM) should be performed moving forward to elucidate the shape of the aggregates formed in solution. Both methods seek to preserve the structures as they exist in solution to avoid artifacts that form during sample preparation for EM methods that require extensive drying and/or exposure to vacuum. Depending on the resolution achieved, it may also be possible to corroborate the QD sizes and interparticle distances calculated using x-ray scattering data with the LP EM or cryo-EM images. Recent work highlights the atomic resolution achievable with 3D liquid-cell electron microscopy, which revealed the intrinsic heterogeneity of ligand-protected nanocrystals in solution.[100]

Finally, the sample preparation and x-ray scattering measurement process should be improved to limit exposure to oxygen. One significant improvement would be to perform all ligand exchanges and sample preparation under a nitrogen atmosphere at the beamline, where samples could be measured immediately after their creation. Such preparation has previously been impossible given the instruments available at sector 5-ID-D at APS, though this possibility may arise in the future. A more readily available improvement is to keep all samples under nitrogen before and during loading into the flow cell. In this scenario, the samples could still be prepared off-site and transported under an inert atmosphere but would remain the inert atmosphere through sample loading and measurement. Ultimately, the ideal scenario is to both prep and measure the samples under an inert atmosphere at the beamline to remove exposure to oxygen and precipitation over time as extraneous variables.

3.6 Chapter Conclusion

A detailed analysis of synchrotron SAXS/MAXS/WAXS flow-cell measurements of aqueous PbS-DHLA QDs suggests that acid-induced aggregation is well described by the DLCA and/or the RLCA of polydisperse hard spheres. The local volume fraction within an aggregate, estimated from the correlation hole, is 13 ± 2%, which suggests a maximum 6-to-1 QD coordination. The scattering profile of the aggregated sample (pH=5) is accurately reproduced using a multi-component model consisting of scattering from a flat baseline, closely packed hard spheres, and a mass fractal aggregate described by Beaucage. The volume fraction parameter of the hard-sphere scattering component is only 0.33, which suggests that a diamond-like packing structure, rather than a simple cubic packing structure indicated by the maximum 6-to-1 coordination, might better describe the aggregates. This chapter demonstrates that aggregation mechanisms, structures, and scales can be reasonably determined from SAXS/MAXS/WAXS flow-cell measurements. Further

work is required to remove extraneous variables, such as exposure to oxygen and precipitation of samples over time, and to determine the reproducibility of this analysis for PbS-DHLA QDs. Future work should investigate the generalizability of this aggregation description to other aqueous QD systems while incorporating advanced LP EM and cryo-EM techniques to help guide analysis and support conclusions.

3.7 Supplementary Information

3.7.1 Solvent and Capillary Scattering

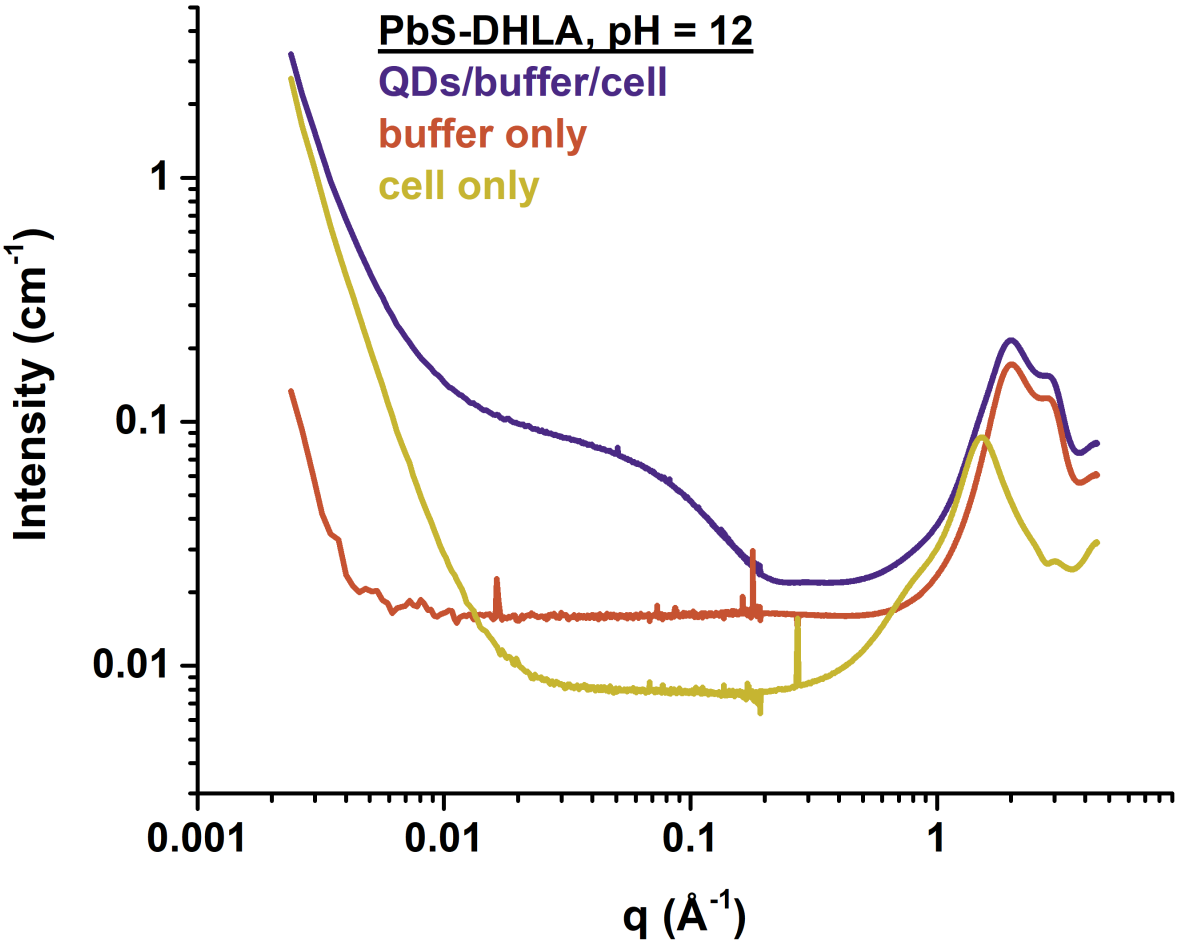

Figure 3.10. Representative x-ray scattering profiles for the buffer solution (dilute DHLA in water, orange trace), capillary (quartz, yellow trace), and raw sample (PbS-DHLA QDs in water, pH = 12, purple trace).

3.7.2 X-ray Scattering Profiles with Error Bars

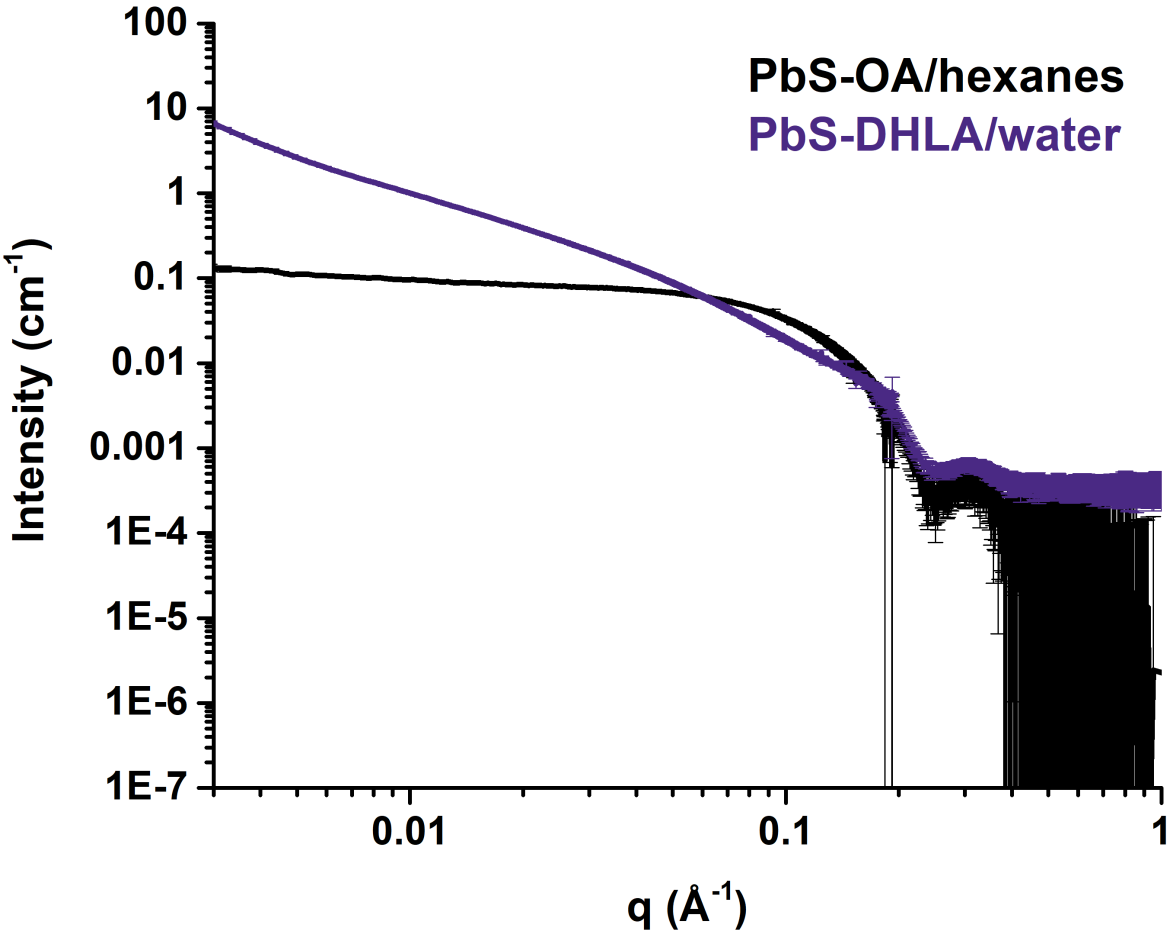

Figure 3.11. X-ray scattering measurements of 1 μM PbS-OA QDs in hexanes (black trace) and 1 μM PbS-DHLA QDs in water at pH = 10.4 (purple trace). Vertical error bars denote the uncertainty propagated through the data reduction process.

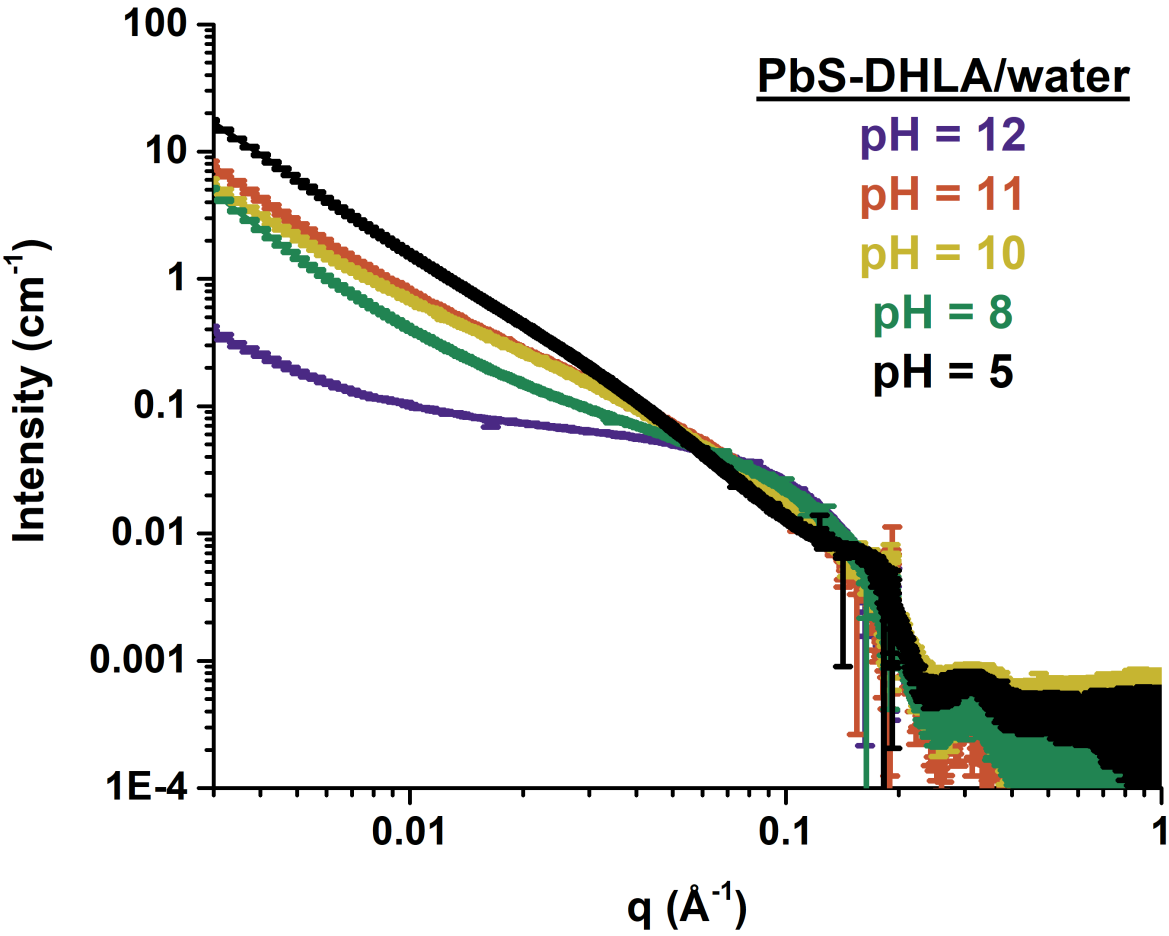

Figure 3.12. X-ray scattering spectra (intensity, cm^{-1}, *vs* *q*, $Å^{-1}$) of aliquots of 1 μM PbS-DHLA QDs in water titrated with 0.5 M HCl. The samples reflect the same batch of aqueous QDs at pH values of 12, 11, 10, 8 and 5 (purple, orange, yellow, green, and black traces, respectively). Vertical error bars denote the uncertainty propagated through the data reduction process.

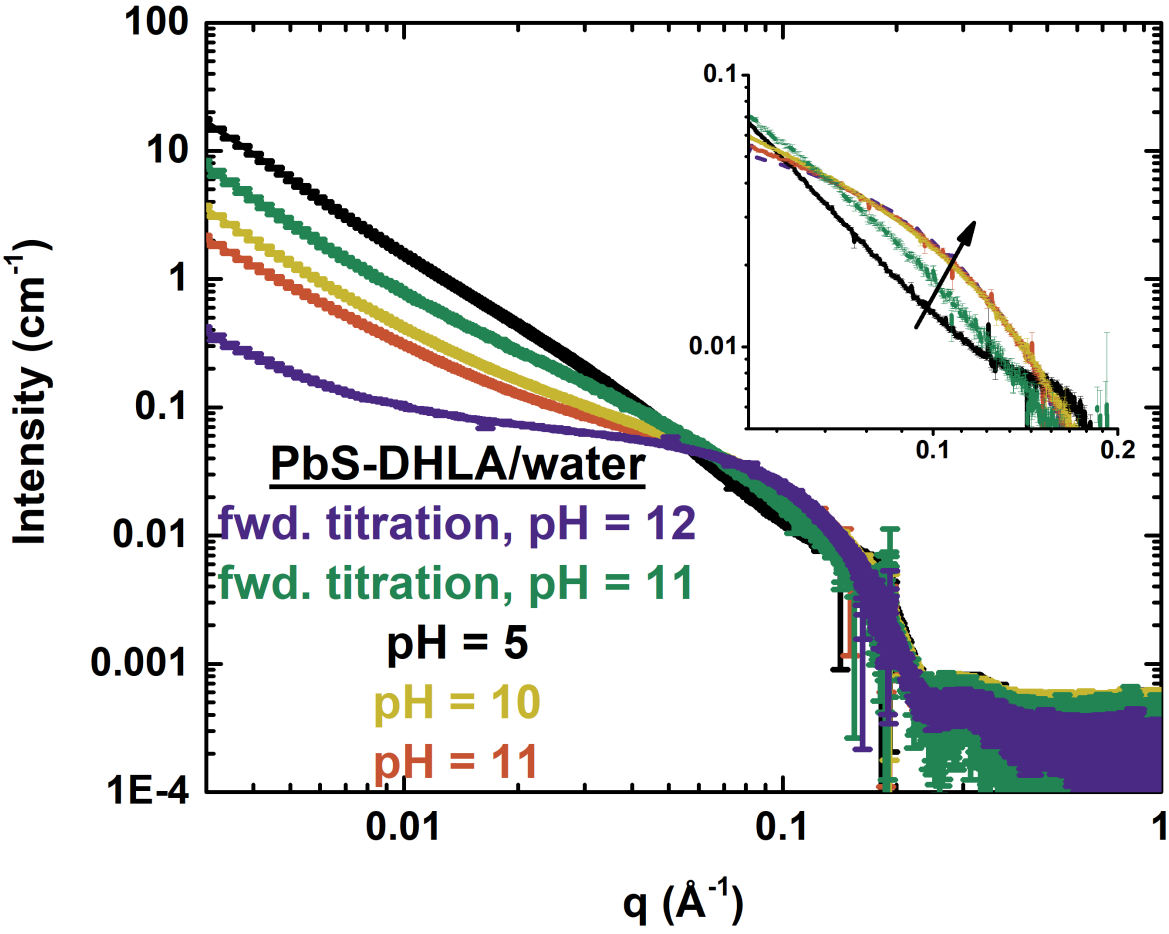

Figure 3.13. X-ray scattering spectra (intensity, cm^{-1}, *vs* q, $Å^{-1}$) of aliquots of 1 μM PbS-DHLA QDs in water titrated with 0.5 M NaOH to bring the same sample of QDs from pH = 5 (black trace) to pH = 10 (yellow trace) and pH = 11 (orange trace). The inset and accompanying arrow highlights the return of the signal between $q \sim 0.04$–0.4 that occurs as the pH increases. The scattering profiles for the forward titration when pH = 12 (purple trace) and pH = 11 (green trace) are shown for comparison. Vertical error bars denote the uncertainty propagated through the data reduction process.

3.7.3 PL Spectra with Absolute Intensities

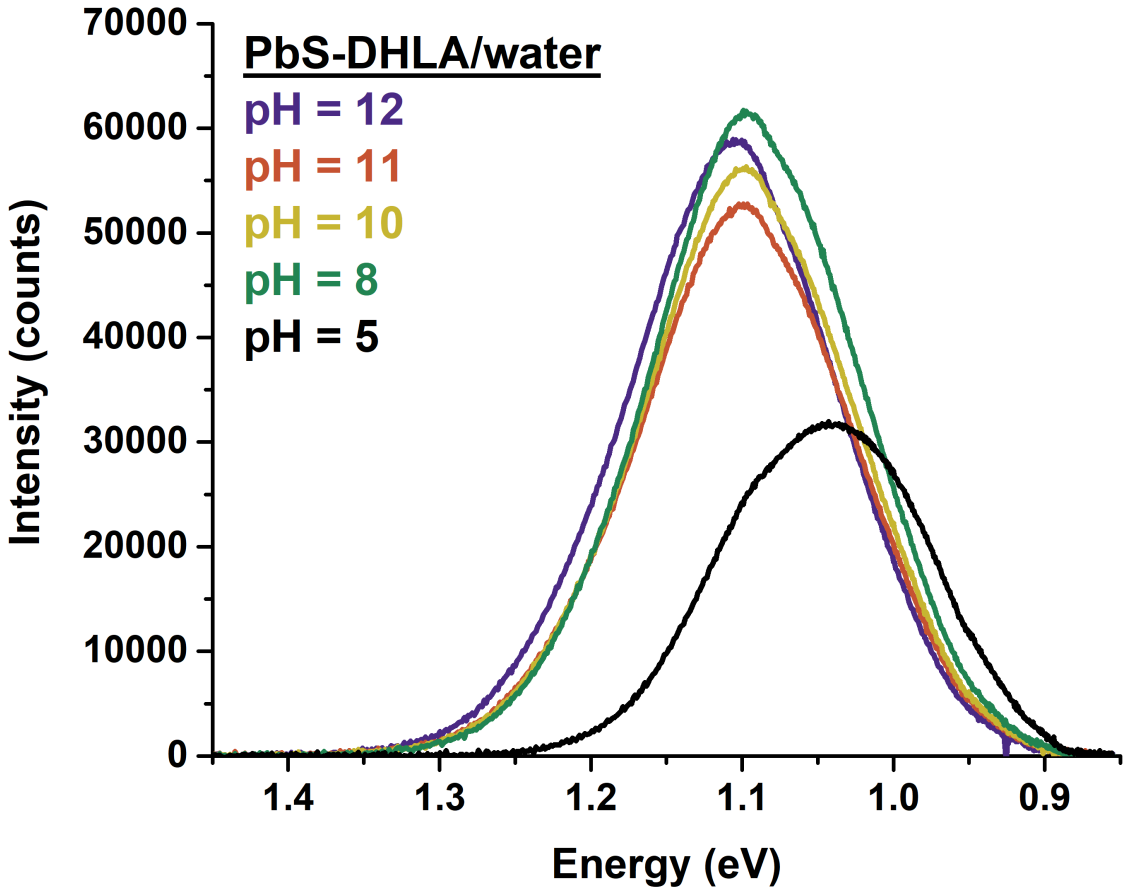

Figure 3.14. PL spectra of aqueous of 1 μM PbS-DHLA QDs titrated with 0.5 M HCl to obtain pH values of 12, 11, 10, 8 and 5 (purple, orange, yellow, green, and black solid lines, respectively).

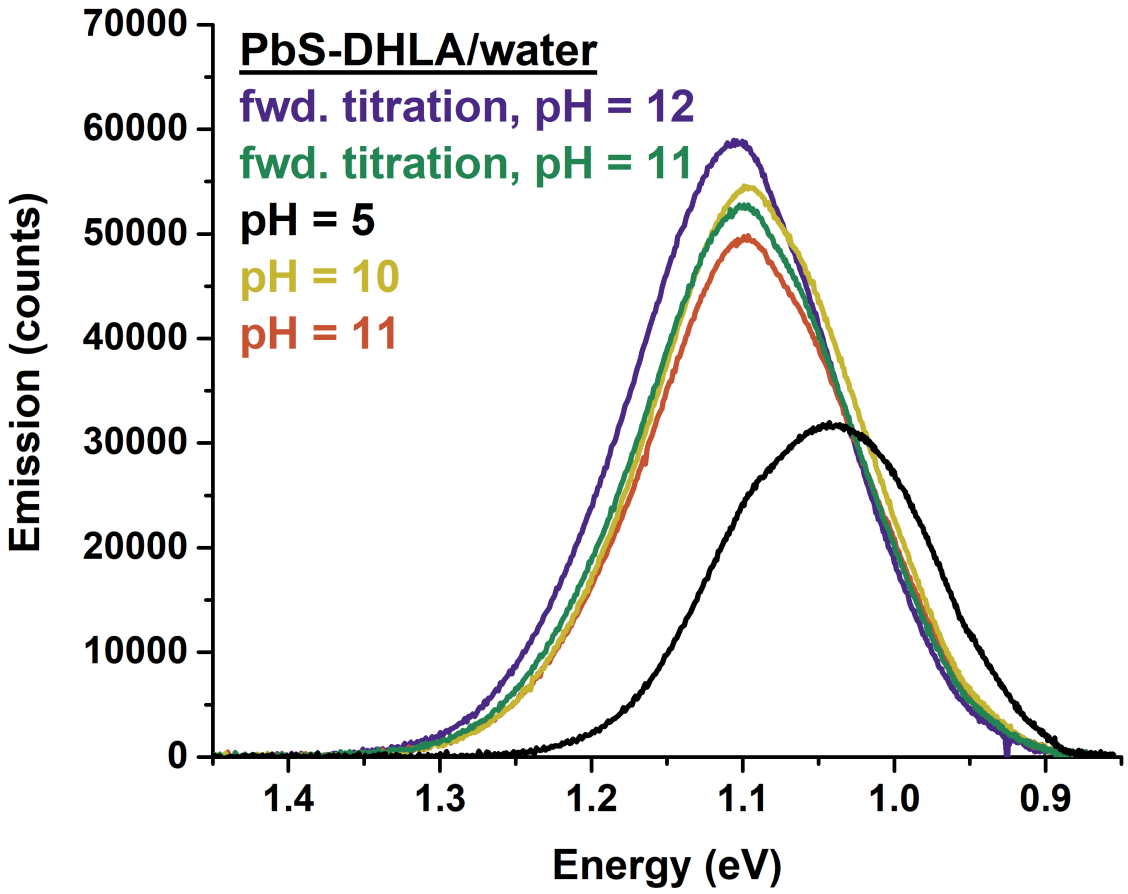

Figure 3.15. PL spectra of the reverse titration of the aqueous 1 μM PbS-DHLA QD sample (pH = 5, black trace) performed by the addition of 0.5 M NaOH to reach pH = 10 (yellow trace) and pH = 11 (orange trace). The forward titration points (pH = 12 and pH = 11, purple and green trace, respectively) are shown for comparison.

3.7.4 Calculating the Local Volume Fraction

We follow the work of Genix *et al.*[88], as stated in the main text, to calculate the estimated local volume fraction of PbS-DHLA QDs in aggregates at pH = 5. We use the polydispersity, σ, determined from the fit in Figure 3.7, to calculate α_{finite}, using **equation 3.1**.

$$\alpha_{finite}(\sigma) = 0.72 - 1.45\sigma^2 \qquad (3.1)$$

We then determine the value of S_0 from the intensity of the minimum in Figure 3.8. With known α_{finite} and S_0, we solve **equation 3.2** for the local volume fraction, κ.

$$S_0 = (1 - \alpha\kappa)^4/(1 + 2\alpha\kappa)^2 \qquad (3.2)$$

3.7.5 Power-Law Fitting

The experimental sample of PbS-DHLA QDs at pH = 5 was fit to a simple power-law function, $I(q) = aq^b$, for two separate ranges of q. Over the larger q range, **Figure 3.16**, b = -1.93 while over the more conservative q range, **Figure 3.17**, b = -1.88, which suggests a fractal dimension, d_f, of ~ 1.9 for PbS-DHLA QD aggregates at pH = 5.

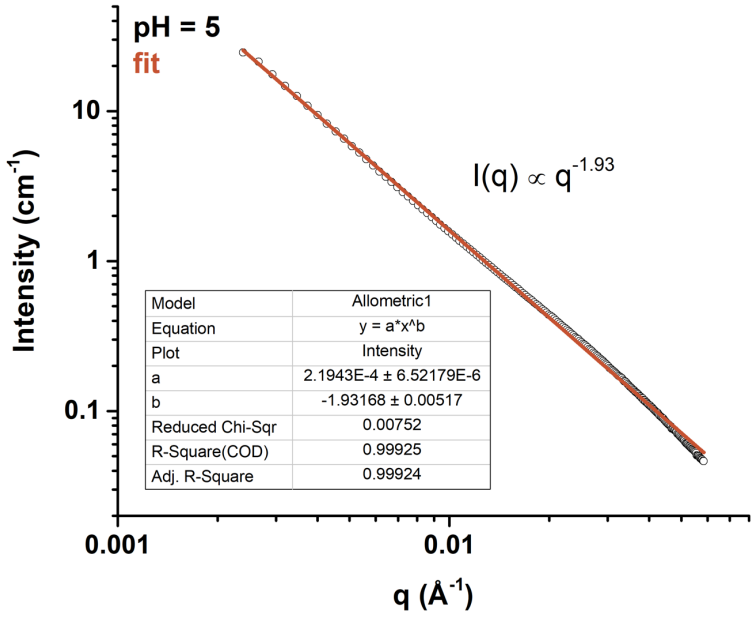

Figure 3.16. X-ray scattering profile (intensity, cm^{-1}, *vs* q, $Å^{-1}$) of 1 μM PbS-DHLA QDs at pH = 5 (black trace) fit to a power-law equation (orange trace), $I(q) = aq^b$, for 0.002 $Å^{-1} < q <$ 0.06 $Å^{-1}$. The exponent, b, is found to be -1.93 with an R-squared value of 0.999.

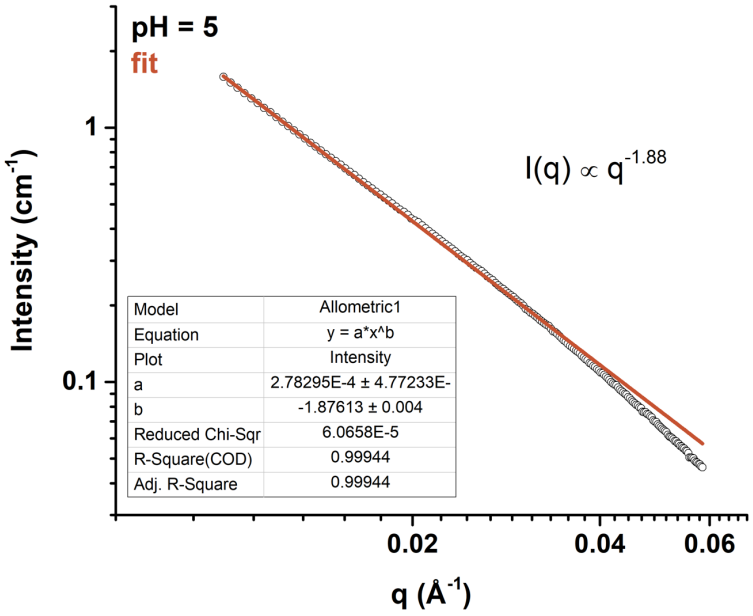

Figure 3.17. X-ray scattering profile (intensity, cm^{-1}, *vs* q, $Å^{-1}$) of 1 μM PbS-DHLA QDs at pH = 5 (black trace) fit to a power-law equation (orange trace), $I(q) = aq^b$, for 0.009 $Å^{-1} < q <$ 0.06 $Å^{-1}$. The exponent, b, is found to be -1.88 with an R-squared value of 0.999.

3.7.6 Multi-component Aggregation Model

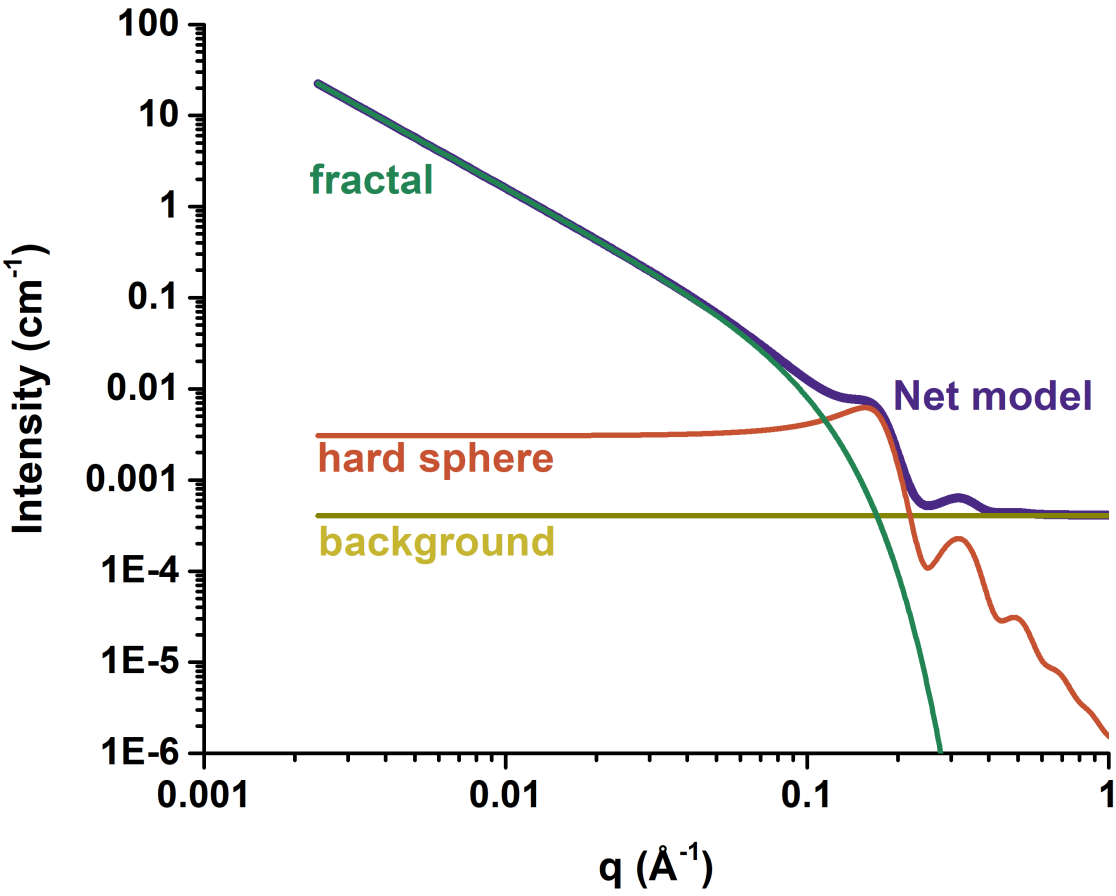

Figure 3.18. X-ray scattering profiles (intensity, cm^{-1}, *vs* *q*, $Å^{-1}$) for the fractal (green trace), hard sphere (orange trace) and background (yellow trace) contributions of the model (purple trace) that fits the experimental scattering profile when pH = 5.

Chapter 4: Simultaneous Phase Transfer and Functionalization of Hydrophobic CdSe/CdS Quantum Dots with Thiolated DNA

Adapted From:

Schwabacher, J. C.; Ramani, N.; Zhu, J.; Rogers, C.R; Mirkin, C.A.; Weiss, E. A. *Unpublished Work.*

4.1 Chapter Summary

This chapter describes the phase transfer of core/shell CdSe/CdS quantum dots (QDs) from chloroform to water using thiolated DNA strands and zwitterionic co-ligands in a ternary solvent system. We report a phase transfer method that exchanges native QD ligands with thiolated DNA strands in less than one hour. While the DNA strands adequately transfer QDs into water in the absence of additional hydrophilic ligands, we employ a zwitterionic co-ligand to increase the yield of the phase transfer and prevent aggregation during the exchange process. Dynamic light scattering (DLS) measurements suggest that including the thiolated co-ligand during the phase transfer process narrows the size distribution of the aqueous ensemble as compared to the size distribution of the DNA-only samples. This method does not rely on reagents are detrimental to QDs or intermediate ligands that prevent DNA from binding to the QD surface, unlike some common protocols for functionalizing QDs with DNA.

4.2 Introduction

DNA-functionalized nanoparticles offer high specificity and directionality in interactions with the surrounding medium through DNA base-pairing.[101-102] Due to this high directionality, DNA-functionalized nanoparticles have been termed programmable atom equivalents, wherein "atoms" of nucleic acid-nanoparticle conjugates are directed to assemble into pre-designed complex structures.[103-105] The success of this framework has been extensively demonstrated with gold nanoparticles[106-109], which has enabled anisotropic single supercrystals[110], RNA interference-based therapeutics[111], and light-responsive supercrystals[112]. Extending this paradigm, DNA-functionalized QDs have potential applications in diagnostics, imaging, drug delivery, and energy harvesting, particularly through Förster Resonance Energy Transfer (FRET)[113] and the formation of complex higher-order assemblies with novel properties.[114] DNA-functionalized QDs have

shown promise in miRNA detection[115], and have been organized into chiral helical architectures[116], 2D lattices[117], and heterogenous cross-shaped complexes[118]. DNA-mediated QD assemblies have allowed, for instance, FRET-based sensing[7, 119-121] and polarized single-particle QD emitters[122].

Many methods for functionalizing QDs with DNA involve modifying DNA strands to increase their affinity for QD surfaces by incorporating imidazole, polyhistidine, phosphorothioate, or thiol groups in the DNA strands.[123] These methods require multiple steps, as hydrophobic QDs must be transferred into water with other hydrophilic ligands before functionalization with DNA can occur, including phosphorothioate-modified DNA in aqueous QD shelling reactions produces core/shell QDs with DNA embedded into the QD shell.[121, 124] Changing the number of phosphorothioate groups in phosphorothioate-modified DNA strands controls the amount of the DNA that tethers to the surface of QDs.[118]

DNA-functionalized QDs with mixed ligand shells containing water-solubilizing ligands, such as mercaptopropionic acid (MPA), are prepared by incubating hydrophilic QDs with excess thiolated DNA for 12–24 hours.[125-128] DNA strands must compete with the other water-solubilizing ligands to bind to the QD surface. MPA and the DNA strand both rely a thiol to bind to the QD surface, which means that excess DNA is required to achieve partially functionalized QDs. Electrostatic assemblies that rely only on the attraction of DNA to cationic QDs in water lack tunability (*i.e.* high non-specific binding) and often result in random DNA-QD aggregates.[123]

Other methods employ conjugation chemistry, such as EDC/NHS coupling[125, 129], disulfide bridging[130], streptavidin-biotin systems[131], or click chemistry[132-133] to chemically tether DNA strands to the QD ligand shell.[134] As-synthesized hydrophobic QDs are exchanged with ligands or wrapped in amphiphilic polymers that provide both water solubility and reactive handles for DNA conjugation. Chemical conjugation methods require reagents that can etch QDs, and therefore

require thorough washing procedures. Thick polymer shells limit access to QD surfaces, which may prohibit catalysis at the surface, and increase the distance between QDs and energy transfer donors/acceptors, which may decrease EnT yields.

Le *et al.*[135] recently reported that a ternary solvent system of dimethyl sulfoxide, chloroform, and water (DMSO/$CHCl_3$/H_2O) successfully and quickly transfers CdZnSeS/ZnS core/shell QDs into water *via* exchanging native QD ligands with 3-mercaptopropionic acid (MPA). Their work suggests that there is zero reduction of QD PL upon phase transfer using this method, and that other methods that employ non-solvent, such as acetone, and centrifugation as a washing step quench PL. They hypothesize that during binary phase transfers (*e.g.* $CHCl_3$/H_2O) high interfacial tension induces defects on the QD surface as the native (hydrophobic) QD ligands and the new (hydrophilic) ligands compete for solubilization at the organic/aqueous solvent interface. A new avenue for the direct functionalization of QDs with thiolated ligands, without the use of an intermediate ligand or intermediate solvation step was developed.

Around the same time as the work described above was reported, we separately began investigating using a liquid lipid extraction method first reported by Bligh and Dyer[136] in 1959 (though based on an earlier method by Folch *et al.*[137]) as a template for a ternary solvent phase transfer protocol for functionalizing QDs with thiolated ligands. The Bligh and Dyer protocol, which was developed for the removal of lipids from biological materials, relies on a miscible $CHCl_3$/MeOH/H_2O (1:2:0.8 v/v/v) system to solubilize tissue samples before separating the mixture into organic ($CHCl_3$) and aqueous (methanolic) phases by the addition of additional $CHCl_3$ and H_2O, and results in the desired lipid extract in the $CHCl_3$ layer with a final ratio of 2:2:1.8 (v/v/v) of $CHCl_3$/MeOH/H_2O . Using the Bligh and Dyer method as a framework, we hypothesized

that a ternary solvent system would provide simultaneous solubility of native, hydrophobic QD ligands and new, hydrophilic ligands to promote QD phase transfer and ligand exchange.

While methods for directly functionalized QDs with small thiolated molecules are well developed, such as the one reported in Chapters 2 and 3, we were unable to adapt these methods the use thiolated-DNA strands as the only hydrophilic ligands. Our work with the Bligh and Dyer protocol and the encouraging results reported by Le *et al.*, led us to employ a $CHCl_3$/DMSO/H_2O ternary solvent system for the phase transfer and DNA-functionalization of CdSe/CdS QDs.

We report the phase transfer of core/shell CdSe/CdS quantum dots (QDs) from chloroform to water using thiolated DNA strands and zwitterionic co-ligands in a ternary solvent system. This method exchanges native QD ligands with thiolated DNA strands. While the DNA strands adequately transfer QDs into water in the absence of additional hydrophilic ligands, we employ a zwitterionic co-ligand to increase the yield of the phase transfer and prevent aggregation during the exchange process. Dynamic light scattering (DLS) measurements suggest that including the thiolated co-ligand during the phase transfer process narrows the size distribution of the aqueous ensemble as compared to the size distribution of the DNA-only samples. This method, unlike common protocols for functionalizing QDs with DNA, does not rely on reagents that degrade QDs or intermediate ligands that prevent DNA from binding to the QD surface, and is completed in less than one hour. These preliminary results underscore the importance of the solvent matrix during phase transfers and highlight a new avenue of QD-DNA functionalization procedures.

4.3 Experimental Methods

4.3.1 CdSe Core QD Synthesis

Following an established protocol[23, 138], 0.147 g of CdO, 2 mL oleic acid (OA), and 3 mL of octadecene (ODE) and introduced into a 25 ml three-neck flask. As the mixture was heated to 120

°C, the flask was switched between vacuum and nitrogen five times. The mixture was heated at 120 °C under nitrogen until the mixture turned clear. The mixture was degassed at 120 °C under vacuum for 1 h before being returned to nitrogen. A 20-mL scintillation vial was filled with 0.5 g Tetradecylphosphonic acid (TDPA) and 2 mL of oleylamine and sealed with a septum and Teflon tape. The vial atmosphere was purged with nitrogen (on the line with the use of a vent needle) for ~ 30 min. This vial was brought into the box with the materials needed to make the 1 M TOPSe. In the glove box, 0.158 g of Se was mixed with 2 mL of trioctylphosphine (TOP) until the solid dissolved (>30 min). 1.5 mL of this 1 M TOPSe solution was added to the vial containing the 2 mL oleylamine and 0.5 g TDPA. Outside the box, under nitrogen flow with a vent, the precursor mixture was heated (on a hot plate) until the solution became clear. This took ~20 minutes with the hot plate temperature set to 115 °C. Under N_2 flow, the temperature of the Cd-Oleate solution was increased to 240 °C before injecting the TOPSe + oleylamine + TDPA mixture (as much as could be removed from the precursor vial via syringe). The temperature was maintained at 212 °C (the original procedure called for 200 °C) for 10 min. After 1 minute the heating mantel was removed. Once the solution was ~ 100 °C, the septum was removed to facilitate cooling. After cooling to 70 °C, 20 mL ethanol was added to the solution to prevent solidification of the product. The sample was cooled to room temperature and divided evenly into two 50-mL Flacon tubes. They were filled with 200-proof ethanol and centrifuged at 3500 rpm for 15 min. The supernatant was discarded and the pellets containing CdSe nanocrystals and TDPA was resuspended in 5 mL hexanes each. This turbid solution was centrifuged for 5 min at room temperature. The clear supernatant containing the QDs was precipitated a final time with ethanol and centrifuged. The pellet containing the QDs was suspended in 10 mL of hexanes.

4.3.2 CdSe/CdS Shelling Procedure

Following previous work[23] that was adapted from an earlier report[138], a cadmium-oleate precursor solution was prepared by dissolving 0.145 g CdO in 2 mL oleic acid and 8 mL ODE to obtain a 0.1 M Cd(oleate)2 solution. The sulfur precursor solution was prepared by dissolving 32 mg S in 10 mL of ODE at 180 °C to obtain the 0.1 M S solution. Both precursor solutions were degassed twice at 70 °C under vacuum for 1 hr, once prior to forming the precursor solution and once after dissolving the precursor. 2 mL of oleylamine, 4 mL of ODE, and 0.453 mL CdSe core solution (298 μM) were introduced into a 50 ml three-neck flask. The hexanes were removed by degassing the solution for 1 hr at 70 °C under vacuum. The flask was filled with N2 and heated to 230 °C. While heating 0.28 mL of the cadmium precursor solution was injected. After reaching 230 °C, the reaction proceeded for 10 min before the addition of 0.28 mL of the sulfur precursor solution. We waited an additional 10 minutes and then injected 0.46 mL of the Cd precursor solution. We then annealed the QDs for 30 mins before cooling the reaction flask.

Following the original washing procedure, which calls for 3 successive ethanol precipitation cycles before resuspending the QDs in hexanes, failed to crash QDs from the reaction solution. All fractions from the washing attempt were combined into a round-bottom flask and the volume of the solution was reduced on a rotary evaporator. The reduced-volume sample was washed once with methanol, which caused phase separation upon addition. The QDs were then crashed with ethanol and resuspended in hexanes.

4.3.3 Ground State Absorption Measurements

All ground state absorption spectra were obtained on a Varian Cary 5000 spectrometer using a 2 mm/10 mm dual pathlength quartz cuvette. We excited our samples along the 2 mm axis and corrected the baselines with solvent blanks prior to measurement.

4.3.4 Photoluminescence Measurements

The photoluminescence (PL) spectra were measured with a Horiba Fluorolog-3 spectrofluorometer using a right-angle geometry and a 2 mm/10 mm dual-pathlength cuvette. The excitation beam was applied along the 10-mm path of the cuvette and the sample emission was collected along the 2-mm path. Samples were excited with 475-nm light. Data was collected using a 0.30 s integration time and 1-nm slit widths.

4.3.5 Zwitterionic Co-Ligand Synthesis

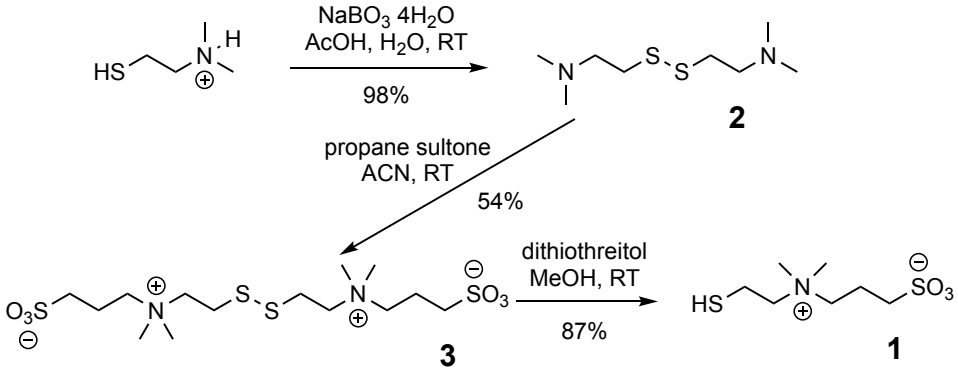

Scheme 4.1. Synthesis of the zwitterionic co-ligand, compound **1**.

Disulfide **2** was prepared by modification of a reported procedure.[139] A 20 mL scintillation vial with magnetic stir bar was charged with 2-(dimethylamino)ethanethiol hydrochloride (1.42 g, 10.0 mmol) and 10 mL aqueous acetic acid (70% v/v). The reaction mixture was cooled to 0 °C and sodium perborate (3.08 g, 20 mmol) was added portion wise. The reaction mixture was allowed to warm to room temperature and stirred 2 h, then transferred to a separatory funnel. Saturated aqueous NaOH was added until the mixture was cloudy (pH ~13), and the aqueous phase was extracted twice with Et_2O. The organic extracts were combined, and the solvent removed by rotary evaporation to yield **2** (1.02 g, 98%) as a colorless oil. NMR signals matched those reported.

Zwitterionic disulfide **3** was prepared by modification of a reported procedure.[1] A dry 100 mL round-bottom flask with magnetic stir bar was charged with **2** (710 mg, 3.41 mmol) and 40 mL dry acetonitrile. 1,3-propanesultone (916 mg, 7.50 mmol) was added and the reaction mixture was stirred at room temperature 16 h. The white precipitate that formed was collected by vacuum filtration and rinsed with acetonitrile, then dried under reduced pressure to yield **3** (837 mg, 54%) as a colorless solid. NMR signals matched those reported.

Synthesis of **1**: A 20 mL scintillation vial with magnetic stir bar was charged with **3** (200 mg, 0.44 mmol) and 8 mL MeOH. Dithiothreitol (72 mg, 0.46 mmol) was added to the resulting suspension, and the reaction mixture was stirred overnight, during which time the turbid reaction mixture became limpid. Then, most (~90%) of the MeOH was removed by rotary evaporation, and the remaining solution was added to 10 mL Et_2O by pipette. The resulting precipitate was collected by vacuum filtration and dried under reduced pressure to yield **1** (175 mg, 87%) as a colorless solid. ^{1}H-NMR (600 MHz, D_2O) δ = 3.58 – 3.52 (m, 2H), 3.52 – 3.46 (m, 2H), 3.13 (s, 6H), 2.99 (t, J = 7.2 Hz, 2H), 2.97 – 2.91 (m, 2H), 2.27 – 2.20 (m, 2H).

4.3.6 DNA Strand Synthesis

The short thiolated-DNA strands used in this study were synthesized and purified by Mirkin and co-workers.

Sequence (5'–3'): TAT CCA GCT GCG TTA-S-S

Theoretical mass: 5703.8 $g \cdot mol^{-1}$

Extinction coefficient (λ=260 nm) 172,500 $L \cdot mol^{-1} \cdot cm^{-1}$

4.3.7 Phosphate Buffer Preparation

5.76348 g of Sodium phosphate dibasic (Na2HPO4, MW=141.96) and 0.2685 g of sodium phosphate monobasic (NaH2PO4, MW=119.98) were dissolved in 250 mL of Milli-Q water (18.2

MΩ·cm at 25 °C) using a volumetric flask. A pH test-strip (MQuant pH 0 – 14 Universal Indicator, Millipore Sigma) confirmed that the solution pH ~ 8. This is solution is referred to as "phosphate buffer."

4.3.8 DNA Strand Preparation

Our thiolated-DNA strand reduction and preparation methods were informed by established protocols.[140-142] In newly washed 3-kDa molecular-weight-cut-off (MWCO) spin filters (Millipore Sigma, Amicon Ultra Centrifugal Filters), each DNA sample, as received from our collaborators, was concentrated to ~ 250 µL using centrifugation at 3500 rpm for 60 minutes. Each concentrate was diluted with 250 µL of phosphate buffer in an Eppendorf tube. Approximately 15 mg of 1,4-dithiothreitol (DTT, MW=154.25, molecular biology grade) was added to each sample. The samples were left to shake at room temperature in the dark for 1 hour.

About 15 minutes before the one-hour incubation time was completed, a NAP5 column was prepared following manufacturer's instructions. The DNA sample was purified using the rinsed NAP5 column and Milli-Q water (18.2 MΩ·cm at 25 °C) as specified by the manufacturer's instructions. Prepared DNA stocks were either used immediately in a phase transfer procedure or immediately stored in a freezer at -20 °C.

4.3.9 Phase Transfer Protocol

For phase transfer using methanol (MeOH, reagent grade), 10 µL of QD stock (24.2 µM) was dried and resuspended in 750 µL of 1:2 (v/v) $CHCl_3$/MeOH. Then, 38.3 µL (~76 equiv. per QD) of acceptor DNA stock (482 µM) and 161.7 µL of Milli-Q water was added. This mixture was incubated in the dark at room temperature on a shaker plate for 35 minutes. After adding 500 µL of 1:1 (v/v) $CHCl_3/H_2O$ and allowing the phases to separate, the sample was centrifuged at 3500

rpm for 1 min. The (top) QD-containing methanolic phase was carefully separated from the (bottom) organic phase using a glass pipette.

For phase transfer using dimethyl sulfoxide (DMSO, anhydrous, ≥ 99%), 10 μL of QD stock (24.2 μM) was dried and resuspended in 250 μL of $CHCl_3$ (HPLC grade) in an Eppendorf tube. 550 μL of DMSO, 160 μL (~103 equiv. per QD) of acceptor DNA stock (156 μM), 20 μL (~26 equiv. per QD) of zwitterion stock (308.93 μM), and 20 μL of water were mixed together before being added to the QD solution. This mixture was incubated in the dark at room temperature on a shaker plate for 35 minutes. After incubation, 500 μL of chloroform was added to separate the phases and the sample was centrifuged at 3500 rpm for 1 minute. The (top) aqueous layer was transferred to a falcon tube and washed with 1 mL of chloroform using centrifugation at 3500 rpm for 1 minute. The (bottom) chloroform layer was removed with a glass pipette and the aqueous layer was washed again with 1 mL chloroform. 250 μL of water was added before centrifugation at 3500 rpm for 1 minute. The chloroform layer was removed, and the aqueous layer was washed once again. At this point, the phases separate quickly and are optically clear, so washing proceeds as an extraction (*i.e.*, without centrifugation). The extraction was repeated with 1 mL of chloroform one last time, for a total of five chloroform washes.

The aqueous layer was transferred to a 7-mL scintillation vials and purged with nitrogen in the dark for approximately 2 hours. The volumes after purging was approximately 360 μL, which was estimated using a 100–1000 μL pipette. The was brought to 750 μL by the addition of 390 μL of Milli-Q water.

4.3.10 Dynamic Light Scattering Measurements using Folded Capillary Cells

Samples were carefully transferred into Folded Capillary Cells (Malvern, DTS1070) using a 1-mL syringe and ensuring that air bubbles were not present inside the cell. The cells were prepared

according to the manufacturer's instructions before loading the samples of interest. Measurements were performed using a dynamic light scattering analyzer (Malvern, Zetasizer Nano). The samples were illuminated with 633-nm He-Ne laser at 25 °C for each measurement.

4.3.11 Concentration Calculations

DNA concentration was calculated using the known extinction coefficient and the Beer-Lambert law such that that molarity of the DNA in a measured sampled is $[DNA] = A_{260}/(\epsilon_{260} * l)$, where A_{260}, ϵ_{260}, and l are the absorbance at 260 nm, the extinction coefficient of the DNA strand at 260 nm and the path length of the cuvette in arbitrary units, $L \cdot mol^{-1} \cdot cm^{-1}$, and cm, respectively.

The QD concentration of a sample was estimated using the existing calibration curve for a CdSe QD ensemble with known absorbance and PL spectra.[143-144]

4.4 Results and Discussion

We synthesized CdSe/CdS core/shell QDs (~ 1 monolayer CdS shell) according to established procedures.[23] We first completed a DNA-functionalization and phase transfer of CdSe/CdS QDs using a $CHCl_3$/MeOH/H_2O solvent, as described in section 4.3. This experiment demonstrates that the functionalization of hydrophobic QDs with *only* thiolated DNA is possible through a ternary solvent system. Employing a ternary solvent that relies on a significant fraction of a non-solvent like methanol, however, is detrimental to the as-synthesized hydrophobic QDs, as demonstrated by the absorbance band broadening, the absorbance baseline increase, and the PL quenching depicted in **Figure 4.1**. Changes in the shape and intensity of the absorbance spectrum upon phase transfer suggests the presence of DNA in the aqueous QD sample. For complete details, see section 4.7.

Through systematic trial and error, we identified that a 1:0.8 (v/v) immiscible mixture of $CHCl_3/H_2O$ becomes miscible upon the addition of no less than 2.2 equivalents by volume of DMSO. We conducted our phase transfers in 2-mL Eppendorf tubes using 250/550/200 μL of $CHCl_3$/DMSO/H_2O as our ternary solvent system. To conduct the ligand exchange and subsequent phase transfer, ~1 μM of CdSe/CdS QDs in 250 μL of $CHCl_3$ was combined with a mixture of 550 μL of DMSO and 200 μL of aqueous ligand solution (*e.g.*, 160 μL of acceptor DNA stock, 20 μL of zwitterionic co-ligand stock, and 20 μL of water). The sample was covered with aluminum foil and was left on the shaker at room temperature for 35 minutes. After 35 minutes, 500 μL of $CHCl_3$ was added to separate the phases and the sample and the resulting QD-containing aqueous phase

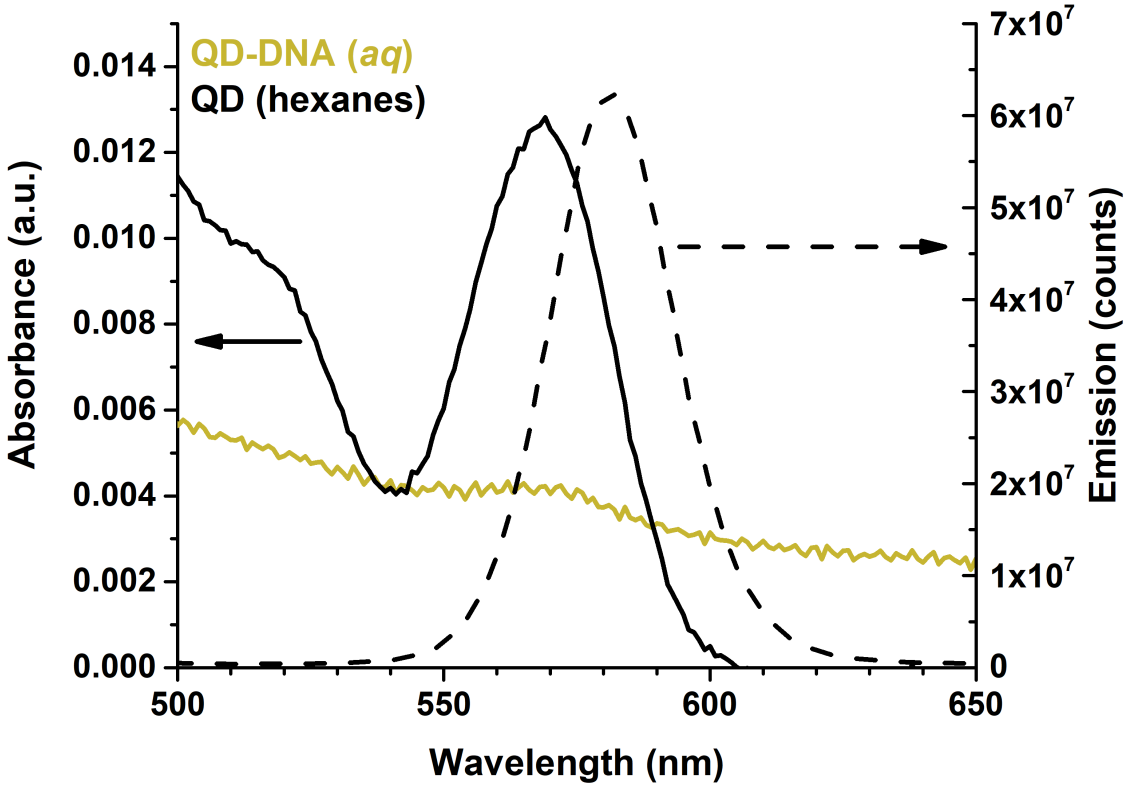

Figure 4.1. Absorbance (left *y*-axis, solid traces) and emission (right *y*-axis, dashed trace) of native (black) and DNA-functionalized (yellow) CdSe/CdS QDs. This phase transfer process uses a $CHCl_3$/MeOH/H_2O ternary solvent and thiolated-DNA. For comparable absorbance peak values, the resulting aqueous QD ensemble has no (completely quenched) emission and a broader absorbance feature with a significant increase in the absorbance baseline.

was washed four more times with $CHCl_3$, as described in section 4.3. The washed QD layer was transferred to a 7-mL scintillation vial and purged with nitrogen in the dark for approximately 2 hours. After purging, the sample volume was increased to ~750 µL by the addition of water. The DMSO-based procedure described above was completed for the DNA, then zwitterion sample (~103 equiv. of DNA per QD added at the start of the exchange and ~23 equiv. of zwitterion per QD zwitterion added for the last 5 minutes of the exchange) and the DNA + zwitterion sample (~103 equiv. of DNA and ~23 equiv. of zwitterion per QD added at the start of the exchange), but

failed for the DNA-only sample (~103 equiv. of DNA per QD added at the start of the exchange), during which the QDs irreversibly aggregated at the solvent interface at the phase separation step.

The DNA, then zwitterion and DNA + Zwitterion samples have sharper absorbance features than the DNA-only sample (**Figure 4.2**). In addition, these DMSO-based ternary solvent phase transfers produce QD ensembles with strong emission peaks. The retainment of some PL feature is a promising sign of the usefulness of ternary solvent phase transfer procedures, since FRET-based sensing applications in biological environments require emissive aqueous QDs. We hypothesized that using DMSO instead of MeOH in the ternary solvent phase transfer procedure helped preserve QD emission. To verify that the addition of zwitterion co-ligand was not responsible for preserving the emission, we repeated the MeOH-based ternary solvent phase transfer procedure and added zwitterion in the last 5 minutes of the incubation period and recorded the sample's PL. The PL was quenched despite including zwitterion during the phase transfer. Similarly, methanolic ternary solvent phase transfers using only zwitterionic co-ligand, or 10:1 zwitterion:DNA were not successful and resulted in QDs crashing at the solvent interface during the phase separation step.

Figure 4.3 displays DLS measurements that suggest that incorporating the zwitterionic co-ligand during the ternary solvent phase transfer procedure decreases aggregation and thus narrows the size distribution of ensembles of DNA-functionalized QDs. Exposing QDs to DNA strands and zwitterion at the same time (purple trace, "DNA + Zwitterion") produces a population with a mean hydrodynamic diameter of 24.3 nm, which is significantly smaller than both the mean hydrodynamic size (38.3 nm) of the phase transfer that exposes QDs to DNA strands before co-ligand molecules (orange trace, "DNA, then Zwitterion") and the mean diameter (55.5 nm) of the phase transfer that entirely omits the co-ligand (yellow trace, "DNA only"). In all cases, the mean

hydrodynamic diameter of the DNA-functionalized QDs is much larger than the expected diameter of the as-synthesized CdSe/CdS QDs, ~ 3.8 nm[23], which implies that aggregation during phase transfer occurs even when zwitterion is added as a co-ligand.

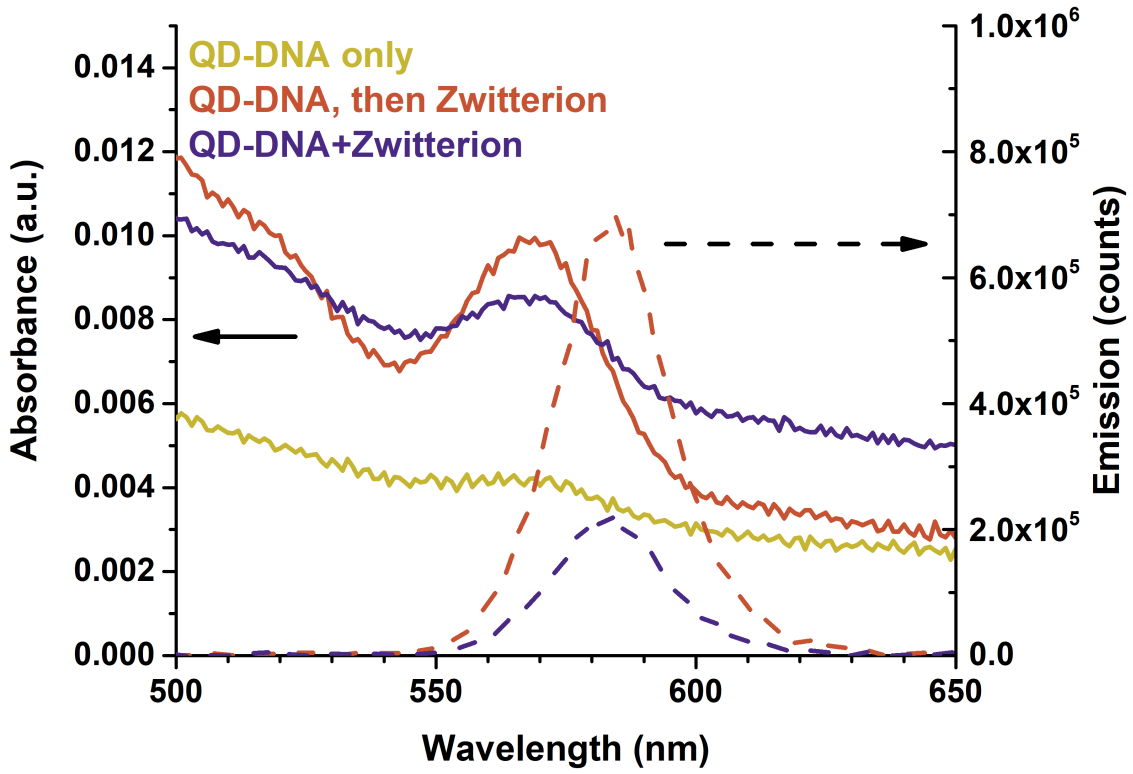

Figure 4.2. Absorbance (left y-axis, solid traces) and emission (right y-axis, dashed traces) of three samples of DNA-functionalized CdSe/CdS QDs prepared using a $CHCl_3$/DMSO/H_2O or $CHCl_3$/MeOH/H_2O ternary solvent with thiolated-DNA strands. The phase transfer that exposes QDs to DNA strands and zwitterion co-ligands at the same time (purple, "DNA + Zwitterion") has a broader absorbance peak and higher absorbance baseline than the absorbance spectra of the sample that exposed QDs to DNA strands before adding co-ligand molecules to the sample (orange, "DNA, then Zwitterion"). Both zwitterion-containing samples have PL peaks, whereas the DNA-only sample, which is the same sample from Figure 4.1 shown for comparison, has no emission.

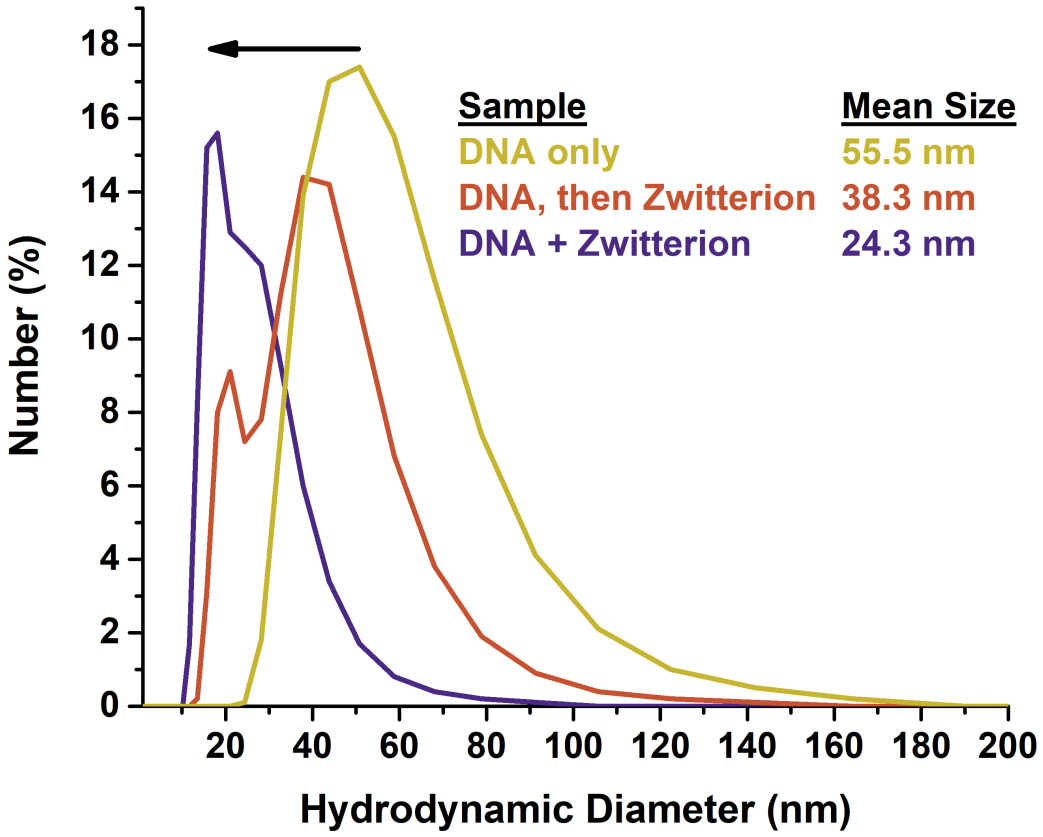

Figure 4.3. The percent of particles (*y*-axis) of a given hydrodynamic diameter in nm (*x*-axis), measured *via* DLS, for three samples of DNA-functionalized CdSe/CdS QDs prepared using a $CHCl_3$/DMSO/H_2O or $CHCl_3$/MeOH/H_2O ternary solvent with thiolated-DNA strands. The phase transfer that exposes QDs to DNA strands and zwitterion co-ligands at the same time (purple, "DNA + Zwitterion") has a mean hydrodynamic diameter of 24.3 nm, which is smaller than the mean hydrodynamic size (38.3 nm) of the phase transfer that exposes QDs to DNA strands before adding co-ligand molecules to the sample (orange, "DNA, then Zwitterion") and the mean diameter (55.5 nm) of the phase transfer that omits the co-ligand (yellow, "DNA only"). The distributions narrow as the mean hydrodynamic diameter decreases. The two-peaked features are an artifact of averaging three runs per sample, which indicates variance between runs.

4.5 Limitations and Future Directions

This preliminary study demonstrates the potential application of ternary solvent systems in functionalizing QDs with thiolated-DNA. This work is the first to report the direct functionalization of QDs with thiolated-DNA—*i.e.*, the functionalizing QDs with thiolated DNA

without the use of intermediate ligands and solvents. Despite this promising start, our current report would benefit from additional systematic trials of the $CHCl_3$/DMSO/H_2O and $CHCl_3$/MeOH/H_2O ternary solvent phase transfers with varying amounts of thiolated-DNA and/or zwitterion. We also encourage the exploration of other ternary solvent systems, which may produce less polydisperse QDs with improved DNA loading, though our initial experiments with an N,N-dimethylformamide (DMF) ternary solvent system suggest that replacing DMSO for DMF increases polydispersity (see section 4.7 for more details).

Poly(acrylamide) gel electrophoresis (PAGE) in combination with optical spectroscopy[145] should be used to assess the amount DNA per QD, the sub-populations within the QD ensemble, and correlate the DNA coverage and aggregation to the spectral profiles of each sub-population moving forward. This analysis is critical to understanding the degree to which aggregation occurs during the exchange and its impacts on the absorbance and emission spectra of the ensemble. PAGE or agarose gel electrophoresis may allow for the isolation of dispersed, non-aggregated aqueous QDs for further characterization.

For QDs functionalized with DNA in this manner to be useful, the DNA strands must be able to hybridize with other DNA strands. Future work, therefore, must also incorporate hybridization studies to examine i) if thiolated-DNA strands on a QD surface will still hybridize to complementary strands, ii) the maximum percentage of surface-bound DNA strands that can hybridize to complementary strands at once, and iii) if these hybridization events can be exploited for the directed self-assembly of complex hierarchical QD structures.

4.6 Chapter Conclusion

This preliminary study demonstrates the potential application of ternary solvent systems in functionalizing QDs with thiolated-DNA. This work is the first to report the direct

functionalization of QDs with thiolated-DNA—*i.e.* the functionalizing QDs with thiolated DNA without the use of intermediate ligands and solvents. This chapter describes the phase transfer of core/shell CdSe/CdS quantum dots (QDs) from chloroform to water using thiolated DNA strands and zwitterionic co-ligands in a ternary solvent system. We report a phase transfer method that exchanges native QD ligands with thiolated DNA strands in less than one hour. While the DNA strands adequately transfer QDs into water in the absence of additional hydrophilic ligands, we employ a zwitterionic co-ligand to increase the yield of the phase transfer and prevent aggregation during the exchange process. Dynamic light scattering (DLS) measurements suggest that including the thiolated co-ligand during the phase transfer process narrows the size distribution of the aqueous ensemble as compared to the size distribution of the DNA-only samples. This method, unlike common protocols for functionalizing QDs with DNA, does not rely on reagents that degrade QDs or intermediate ligands that prevent DNA from binding to the QD surface.

4.7 Supplementary

4.7.1 Absorbance Spectra Confirm Presence of DNA

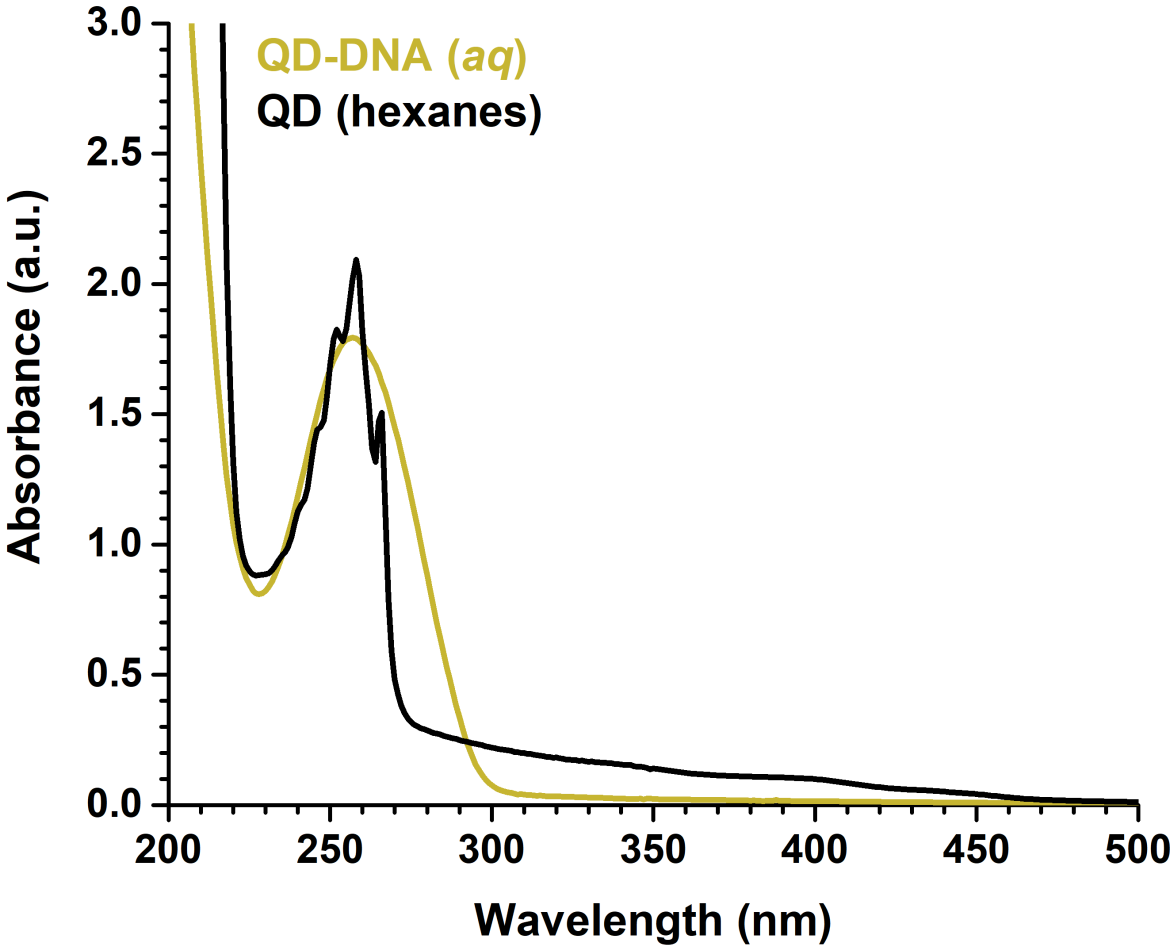

Figure 4.4. Representative absorbance spectra of CdSe/CdS QDs before (black trace) and after (yellow trace) phase transfer from hexanes into aqueous solvent using thiolated-DNA. The broad absorbance peak near 260 nm is contributed by DNA in solution and may be used to calculate the concentration of DNA. The spectra here correspond to the sample depicted in Figure 4.1.

4.7.2 Ternary Solvent Phase Transfers using DMF

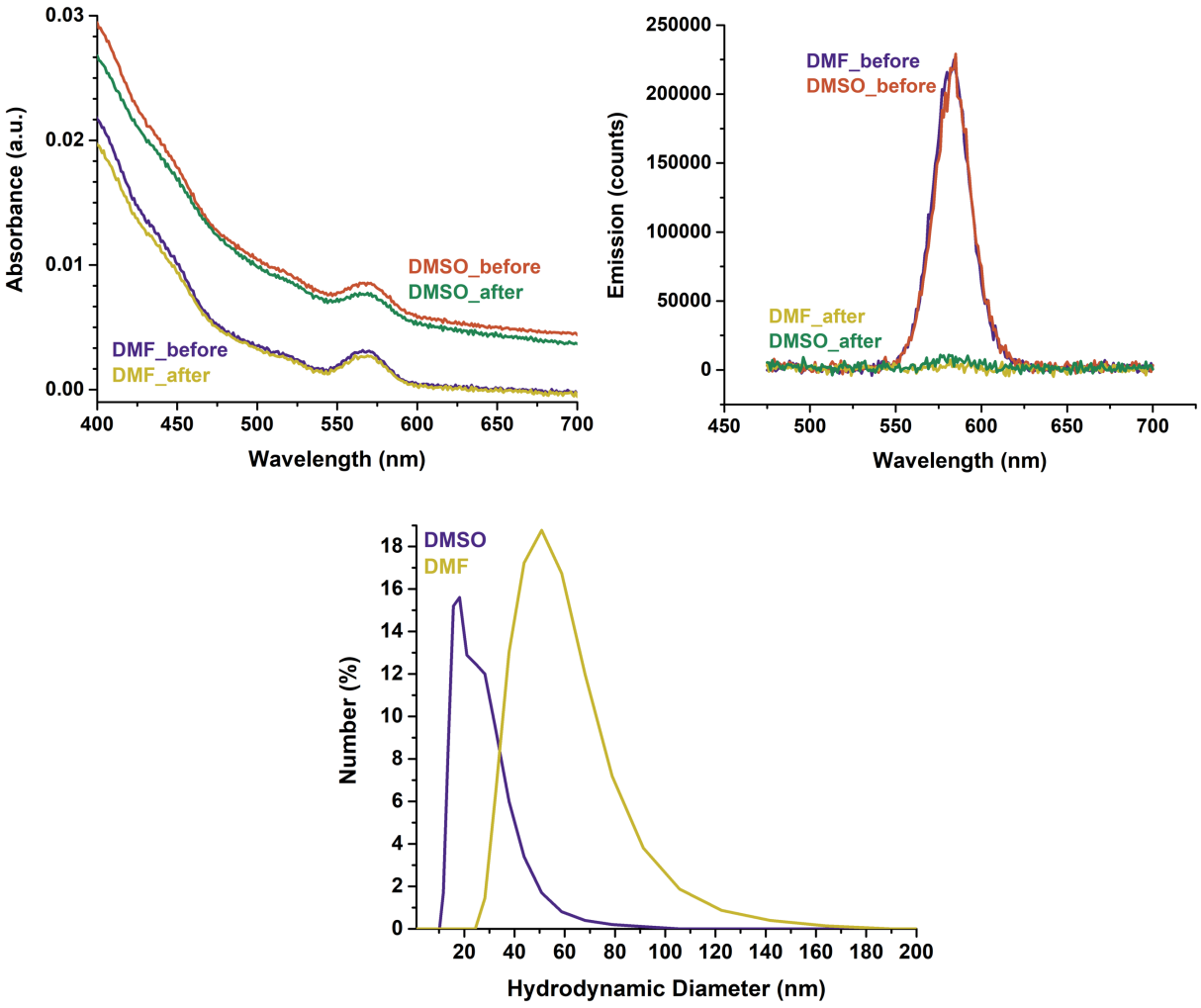

Figure 4.5. Absorbance (**top-left graph**), emission (**top-right graph**), and DLS (**bottom graph**) spectra of CdSe/CdS QDs transferred into water using either DMSO or DMF in a ternary solvent phase transfer with DNA and zwitterionic co-ligands. Despite having a smaller scattering baseline (purple and yellow traces, top left) than the sample transferred using DMSO (orange and green traces, top right), the DMF-based phase transfer produced a QD ensemble with a broader distribution and larger average hydrodynamic diameter (yellow trace, bottom graph) than the ensemble from the DMSO-based phase transfer (purple trace, bottom graph). In both samples, the PL is quenched after the DLS measurements (top-right graph), though there are no significant changes in the absorbance spectra before and after DLS (top-right graph).

Chapter 5: Conclusions

5.1 Dissertation Summary

This dissertation studies the effects of phase transfers with thiol ligands on the optical properties of quantum dots (QDs) in water. In particular, the work presented here focuses on two systems: i) dihydrolipoic acid (DHLA)-capped PbS QDs and ii) core/shell CdSe/CdS QDs functionalized with thiolated-DNA strands.

In Chapter 1, we introduced the novel properties that arise from the quantum confinement of electronic wavefunctions in QDs. We briefly introduced well-established QD syntheses and post-synthetic modification methods. We detailed to two types of QDs relevant to this thesis—PbS and CdSe QDs. The importance of post-synthetic ligand exchanges and QD-QD Förster resonance energy transfer (FRET)processes for designing biologically relevant QD systems were also described. Chapter 1 concluded with an outline of the research presented in this dissertation.

In Chapter 2, we examined how phase transfers of oleic acid-capped PbS QDs with DHLA impact the pH response of aqueous PbS-DHLA QD ensembles. The photoluminescence (PL) spectra of populations of PbS-DHLA QDs bathochromically shift by up to 95 meV as the pH value decreases from 12 to 5. Optical spectroscopy experiments, dynamic light scattering (DLS) experiments, and the results of a phenomenological model for exciton hopping among QDs suggest that these bathochromic shifts can be entirely accounted for by QD-QD FRET as the QDs aggregate with decreasing pH. The magnitude of the PL shift is strongly correlated with the sample's polydispersity directly after phase transfer into basic water. Extrapolation of these data to a hypothetically completely monodisperse sample of QDs yields a PL full width at half maximum (fwhm) of an ensemble of single DHLA-capped PbS QDs in water of 130 meV. This

work shows that the PL linewidth before aggregation, which is controlled by the phase transfer procedure, is an excellent predictor of the pH response of the emission spectra of the QDs.

In Chapter 3, we described the x-ray scattering profiles of PbS QDs transferred from hexanes into water *via* displacement of the native oleate ligands with DHLA. Small-, mid-, and wide-angle x-ray scattering (SAXS/MAXS/WAXS) spectra of samples flowing at 20 μL/s through a quartz capillary were simultaneously recorded upon exposure to 9.0 keV x-rays. Following the system described in Chapter 2, forward and reverse titrations ($12 \geq pH \geq 5$) were performed using 0.5 M HCl and 0.5 M NaOH, respectively, to assess the structure and mechanism of formation of PbS-DHLA QD aggregates. Absorbance and photoluminescence (PL) spectra confirm that the QDs aggregate as the pH decreases below the p*K*a of the PbS-DHLA system (=8.6). The x-ray scattering spectra of all samples have high-q features that correspond to spherical particles with an approximate radius of 1.79 nm. The x-ray scattering spectrum of the most aggregated sample (PbS-DHLA QDs at pH = 5) features a distinct peak at $q \sim 0.1$ Å^{-1}, which we attribute to tightly packed QDs with an approximate center-to-center distance of 3.8 nm. We use the correlation hole at pH = 5 ($q \sim 0.11$ Å^{-1}) to calculate an estimated local volume fraction of 13 ± 2% and maximum 6-to-1 coordination for QDs in an aggregate. The scattering profile at pH = 5 also features an upturn at $q < 0.1$ Å^{-1} due to the presence of relatively large fractal aggregates with a fractal dimension of 1.8–1.9. The scattering spectrum of the aggregated sample is well described by the diffusion-limited cluster aggregation (DLCA) and/or the reaction-limited cluster aggregation (RLCA) of polydisperse hard spheres into a mass fractal.

In Chapter 4, we described the phase transfer of CdSe/CdS QDs from chloroform to water using thiolated-DNA strands and zwitterionic co-ligands in a ternary solvent system. This phase transfer method exchanges native QD ligands with thiolated-DNA strands in less than one hour.

While the DNA strands adequately transfer QDs into water in the absence of additional hydrophilic ligands, our preliminary work suggests that incorporating a zwitterionic co-ligand increases the phase transfer yield and prevents aggregation during the exchange process. DLS measurements indicate that including the thiol co-ligand during the phase transfer process narrows the size distribution of the aqueous ensemble as compared to the size distribution of the DNA-only samples. This method does not rely on reagents that degrade QDs or intermediate thiol ligands that prevent DNA from binding to the QD surface and may generalize across many solvent combinations.

5.2 Future Directions

This thesis depicts a preliminary investigation of how phase transfer procedures dictate the pH-responsiveness, colloidal stability, and functionality of QD ensembles in aqueous environments. Here, we present three promising directions to expand upon our research: i) employ metal-coordinated ligands to reduce the detrimental effects of phase transfers on hydrophobic QDs, ii) use a combination of x-ray scattering, neutron scattering, and advanced electron microscopy techniques to detail the structures and aggregation mechanisms of aqueous QDs, and iii) optimize complex solvent systems to reduce interfacial tension and ligand exchange-induced aggregation during phase transfer processes.

5.2.1 Metal-Coordinated Ligands for QD Phase Transfers

As discussed in Chapter 2, further work is needed to develop DHLA-based ligand exchange procedures that consistently yield monodisperse QD ensembles with pH-independent spectra if the continued use of DHLA as a QD ligand is desired. Prior research suggests[31] one relatively simple solution to decrease polydispersity is to add metallated ligand, *i.e.*, DHLA complexed to a Pb atom, and/or excess metal ion, *e.g.*, $Pb(NO_3)_2$ into the exchange mixture. Sources of excess Pb

atoms may promote the replacement of Pb atoms that are removed from the QD surface during the carboxylate-thiolate exchange process,[146-147] thereby preserving the QD surface, size, and optoelectronic properties. One foreseeable challenge is the insolubility of the Pb-DHLA complex[148], which may prevent employing previously isolated metallated ligand as the ligand source for the phase transfer.

5.2.2 Complete Characterization of Aqueous QDs and their Aggregates

As outlined in Chapter 3, the wealth of information and insight regarding structures across relatively large length scales in solution makes simultaneous SAXS/MAXS/WAXS measurements a powerful tool to investigate nanoparticle aggregation. However, accurate analyses of such data should be informed by images of structures acquired with advanced electron microscopy techniques, such as liquid-phase electron microscopy (LP EM) or cryogenic electron microscopy (cryo-EM), that preserve the structures as they exist in solution. Depending on the resolution achieved, it may also be possible to corroborate the QD sizes and interparticle distances calculated using x-ray scattering data with the LP EM or cryo-EM images. 3D liquid-cell electron microscopy achieved atomic resolution for a sample of platinum nanocrystals and revealed the intrinsic heterogeneity of ligand-protected nanocrystals in solution.[100]

Small-angle neutron scattering (SANS) is also a powerful technique for resolving core, ligand-shell, and solvent structures for oleate-capped PbS QDs.[70] SANS, unlike the more commonly used UV-Vis spectroscopy, transmission electron microscopy, and SAXS characterization techniques, can provide information about organic QD ligands, as well as detailed information regarding the QD surface. SANS was recently used to quantify the $PbCl_x$ layer inherent to PbS QDs synthesized using $PbCl_2$.[149] Similarly, grazing-incidence/grazing-transmission small-angle x-ray scattering (GISAXS/GTSAXS) may be used to investigate the impact of unbound ligands on the superlattice

structure and orientation in QD films.[150] The role of unbound ligands in aqueous QD stability and mechanism of aggregation remains relatively unexplored even though some amount of unbound ligand is always present in solution.

5.2.3 Ternary Solvents for Aqueous Phase Transfers with Thiol Ligands

As outlined in Chapter 4, we encourage the exploration of ternary solvent systems to transfer hydrophobic QDs into water with hydrophilic thiol ligands. Our current findings indicate that systematic trials of $CHCl_3$/DMSO/H_2O, $CHCl_3$/MeOH/H_2O, and $CHCl_3$/DMF/H_2O ternary solvent phase transfers with thiol ligands will provide more details about the optimal solvent matrix for minimal disruption of the QD surfaces during phase transfer. We believe that these phase transfers may generalize to other thiol-containing ligands, beyond the DHLA and thiolated-DNA strands presented in this work. For instance, a ternary solvent could overcome the solubility challenges for metallated thiol ligands described in section 5.2.1 while decreasing the interfacial tension of the phase transfer matrix. The advanced characterization techniques suggested in section 5.2.2 could offer insight into how the combination of ternary solvent and metallated ligand influences the surfaces and ligand shells of the phase-transferred QDs. We, therefore, recommend the incorporation of metal-coordinated ligands, advanced characterization techniques, and complex solvent mixtures into studies of aqueous QDs prepared *via* phase transfers.

References

1. Cui, J.; Panfil, Y. E.; Koley, S.; Shamalia, D.; Waiskopf, N.; Remennik, S.; Popov, I.; Oded, M.; Banin, U. Colloidal Quantum Dot Molecules Manifesting Quantum Coupling at Room Temperature. *Nat. Commun.* **2019,** *10*, 5401.
2. Xia, Y.; Chen, W.; Zhang, P.; Liu, S.; Wang, K.; Yang, X.; Tang, H.; Lian, L.; He, J.; Liu, X., et al. Facet Control for Trap-State Suppression in Colloidal Quantum Dot Solids. *Adv. Funct. Mater.* **2020,** *30*, 2000594.
3. Pietryga, J. M.; Park, Y.-S.; Lim, J.; Fidler, A. F.; Bae, W. K.; Brovelli, S.; Klimov, V. I. Spectroscopic and Device Aspects of Nanocrystal Quantum Dots. *Chem. Rev.* **2016,** *116*, 10513-10622.
4. Baskoutas, S.; Terzis, A. F. Size-Dependent Band Gap of Colloidal Quantum Dots. *J. Appl. Phys.* **2006,** *99*, 013708.
5. Ma, Q.; Su, X. Near-Infrared Quantum Dots: Synthesis, Functionalization and Analytical Applications. *Analyst* **2010,** *135*, 1867-1877.
6. Jaiswal, J. K.; Simon, S. M. Potentials and Pitfalls of Fluorescent Quantum Dots for Biological Imaging. *Trends Cell Biol.* **2004,** *14*, 497-504.
7. Cardoso Dos Santos, M.; Algar, W. R.; Medintz, I. L.; Hildebrandt, N. Quantum Dots for Förster Resonance Energy Transfer (FRET). *TrAC, Trends Anal. Chem.* **2020,** *125*, 115819.
8. Hines, M. A.; Scholes, G. D. Colloidal PbS Nanocrystals with Size-Tunable Near-Infrared Emission: Observation of Post-Synthesis Self-Narrowing of the Particle Size Distribution. *Adv. Mater.* **2003,** *15*, 1844-1849.
9. Hou, B.; Cho, Y.; Kim, B. S.; Hong, J.; Park, J. B.; Ahn, S. J.; Sohn, J. I.; Cha, S.; Kim, J. M. Highly Monodispersed PbS Quantum Dots for Outstanding Cascaded-Junction Solar Cells. *ACS Energy Lett.* **2016,** *1*, 834-839.
10. Weidman, M. C.; Beck, M. E.; Hoffman, R. S.; Prins, F.; Tisdale, W. A. Monodisperse, Air-Stable PbS Nanocrystals via Precursor Stoichiometry Control. *ACS Nano* **2014,** *8*, 6363-6371.
11. Murray, C. B.; Norris, D. J.; Bawendi, M. G. Synthesis and Characterization of Nearly Monodisperse CdE (E = Sulfur, Selenium, Tellurium) Semiconductor Nanocrystallites. *J. Am. Chem. Soc.* **1993,** *115*, 8706-8715.
12. Makkar, M.; Viswanatha, R. Frontier Challenges in Doping Quantum Dots: Synthesis and Characterization. *RSC Adv.* **2018,** *8*, 22103-22112.
13. Nandan, Y.; Mehata, M. S. Wavefunction Engineering of Type-I/Type-II Excitons of CdSe/CdS Core-Shell Quantum Dots. *Sci. Rep.* **2019,** *9*, 2.
14. García-Santamaría, F.; Brovelli, S.; Viswanatha, R.; Hollingsworth, J. A.; Htoon, H.; Crooker, S. A.; Klimov, V. I. Breakdown of Volume Scaling in Auger Recombination in CdSe/CdS Heteronanocrystals: The Role of the Core−Shell Interface. *Nano Lett.* **2011,** *11*, 687-693.
15. Purcell-Milton, F.; Visheratina, A. K.; Kuznetsova, V. A.; Ryan, A.; Orlova, A. O.; Gun'ko, Y. K. Impact of Shell Thickness on Photoluminescence and Optical Activity in Chiral CdSe/CdS Core/Shell Quantum Dots. *ACS Nano* **2017,** *11*, 9207-9214.
16. Ko, J.; Jeong, B. G.; Chang, J. H.; Joung, J. F.; Yoon, S.-Y.; Lee, D. C.; Park, S.; Huh, J.; Yang, H.; Bae, W. K., et al. Chemically Resistant and Thermally Stable Quantum Dots Prepared

by Shell Encapsulation with Cross-Linkable Block Copolymer Ligands. *NPG Asia Mater.* **2020,** *12*, 19.
17. Harris, R. D.; Bettis Homan, S.; Kodaimati, M.; He, C.; Nepomnyashchii, A. B.; Swenson, N. K.; Lian, S.; Calzada, R.; Weiss, E. A. Electronic Processes within Quantum Dot-Molecule Complexes. *Chem. Rev.* **2016,** *116*, 12865-12919.
18. Dutta, A. K.; Ho, T.; Zhang, L.; Stroeve, P. Nucleation and Growth of Lead Sulfide Nano- and Microcrystallites in Supramolecular Polymer Assemblies. *Chem. Mater.* **2000,** *12*, 1042-1048.
19. Wind, O.; Gindele, F.; Woggon, U.; Klingshirn, C. Gain Processes in CdSe Quantum Dots. *J. Cryst. Growth* **1996,** *159*, 867-870.
20. Mohamed, M. B.; Tonti, D.; Al-Salman, A.; Chemseddine, A.; Chergui, M. Synthesis of High Quality Zinc Blende CdSe Nanocrystals. *J. Phys. Chem. B* **2005,** *109*, 10533-7.
21. Drijvers, E.; De Roo, J.; Geiregat, P.; Fehér, K.; Hens, Z.; Aubert, T. Revisited Wurtzite CdSe Synthesis: A Gateway for the Versatile Flash Synthesis of Multishell Quantum Dots and Rods. *Chem. Mater.* **2016,** *28*, 7311-7323.
22. Wu, F.; Zhang, Z.; Zhu, Z.; Li, M.; Lu, W.; Chen, M.; Xu, E.; Wang, L.; Jiang, Y. Fine-Tuning the Crystal Structure of Cdse Quantum Dots by Varying the Dynamic Characteristics of Primary Alkylamine Ligands. *CrystEngComm* **2018,** *20*, 4492-4498.
23. Kodaimati, M. S.; Lian, S. C.; Schatz, G. C.; Weiss, E. A. Energy Transfer-Enhanced Photocatalytic Reduction of Protons within Quantum Dot Light-Harvesting-Catalyst Assemblies. *Proc. Natl. Acad. Sci. U. S. A.* **2018,** *115*, 8290-8295.
24. Clapp, A. R.; Medintz, I. L.; Mattoussi, H. Förster Resonance Energy Transfer Investigations Using Quantum-Dot Fluorophores. *ChemPhysChem* **2006,** *7*, 47-57.
25. Aldana, J.; Wang, Y. A.; Peng, X. Photochemical Instability of CdSe Nanocrystals Coated by Hydrophilic Thiols. *J. Am. Chem. Soc.* **2001,** *123*, 8844-8850.
26. Wang, Y.; Herron, N. Nanometer-Sized Semiconductor Clusters: Materials Synthesis, Quantum Size Effects, and Photophysical Properties. *J. Phys. Chem.* **1991,** *95*, 525-532.
27. Chan, W. C. W.; Maxwell, D. J.; Gao, X.; Bailey, R. E.; Han, M.; Nie, S. Luminescent Quantum Dots for Multiplexed Biological Detection and Imaging. *Curr. Opin. Biotechnol.* **2002,** *13*, 40-46.
28. Deng, D. W.; Zhang, W. H.; Chen, X. Y.; Liu, F.; Zhang, J.; Gu, Y. Q.; Hong, J. M. Facile Synthesis of High-Quality, Water-Soluble, Near-Infrared-Emitting PbS Quantum Dots. *Eur. J. Inorg. Chem.* **2009**, 3440-3446.
29. Zamberlan, F.; Turyanska, L.; Patane, A.; Liu, Z.; Williams, H. E. L.; Fay, M. W.; Clarke, P. A.; Imamura, Y.; Jin, T.; Bradshaw, T. D., et al. Stable DHLA-PEG Capped PbS Quantum Dots: from Synthesis to Near-Infrared Biomedical Imaging. *J. Mater. Chem. B* **2018,** *6*, 550-555.
30. Zhao, H. G.; Wang, D. F.; Chaker, M.; Ma, D. L. Effect of Different Types of Surface Ligands on the Structure and Optical Property of Water-Soluble PbS Quantum Dots Encapsulated by Amphiphilic Polymers. *J. Phys. Chem. C* **2011,** *115*, 1620-1626.
31. Shestha, A.; Yin, Y.; Andersson, G. G.; Spooner, N. A.; Qiao, S.; Dai, S. Versatile PbS Quantum Dot Ligand Exchange Systems in the Presence of Pb-Thiolates. *Small* **2017,** *13*, 1602956.
32. Liu, Y.; Kim, D.; Morris, O. P.; Zhitomirsky, D.; Grossman, J. C. Origins of the Stokes Shift in PbS Quantum Dots: Impact of Polydispersity, Ligands, and Defects. *ACS Nano* **2018,** *12*, 2838-2845.

33. Hinds, S.; Myrskog, S.; Levina, L.; Koleilat, G.; Yang, J.; Kelley, S. O.; Sargent, E. H. NIR-Emitting Colloidal Quantum Dots having 26% Luminescence Quantum Yield in Buffer Solution. *J. Am. Chem. Soc.* **2007,** *129*, 7218-7219.
34. Tyrakowski, C. M.; Snee, P. T. Ratiometric CdSe/ZnS Quantum Dot Protein Sensor. *Anal. Chem.* **2014,** *86*, 2380-2386.
35. Snee, P. T. The Role of Colloidal Stability and Charge in Functionalization of Aqueous Quantum Dots. *Acc. Chem. Res.* **2018,** *51*, 2949-2956.
36. Zhang, C.; Xia, Y.; Zhang, Z.; Huang, Z.; Lian, L.; Miao, X.; Zhang, D.; Beard, M. C.; Zhang, J. Combination of Cation Exchange and Quantized Ostwald Ripening for Controlling Size Distribution of Lead Chalcogenide Quantum Dots. *Chem. Mater.* **2017,** *29*, 3615-3622.
37. He, C.; Zhang, Z.; Wang, C.; Jiang, Y.; Weiss, E. A. Reversible Modulation of the Electrostatic Potential of a Colloidal Quantum Dot through the Protonation Equilibrium of its Ligands. *J. Phys. Chem. Lett.* **2017,** *8*, 4981-4987.
38. Debruyne, D.; Deschaume, O.; Coutiño-Gonzalez, E.; Locquet, J.-P.; Hofkens, J.; Van Bael, M. J.; Bartic, C. The pH-Dependent Photoluminescence of Colloidal CdSe/ZnS Quantum Dots with Different Organic Coatings. *Nanotechnology* **2015,** *26*, 255703.
39. Roux, S.; Garcia, B.; Bridot, J.-L.; Salomé, M.; Marquette, C.; Lemelle, L.; Gillet, P.; Blum, L.; Perriat, P.; Tillement, O. Synthesis, Characterization of Dihydrolipoic Acid Capped Gold Nanoparticles, and Functionalization by the Electroluminescent Luminol. *Langmuir* **2005,** *21*, 2526-2536.
40. Young, A. G.; Green, D. P.; McQuillan, A. J. IR Spectroscopic Studies of Adsorption of Dithiol-Containing Ligands on CdS Nanocrystal Films in Aqueous Solutions. *Langmuir* **2007,** *23*, 12923-12931.
41. Mattoussi, H.; Mauro, J. M.; Goldman, E. R.; Anderson, G. P.; Sundar, V. C.; Mikulec, F. V.; Bawendi, M. G. Self-Assembly of CdSe−ZnS Quantum Dot Bioconjugates Using an Engineered Recombinant Protein. *J. Am. Chem. Soc.* **2000,** *122*, 12142-12150.
42. Medintz, I. L.; Clapp, A. R.; Mattoussi, H.; Goldman, E. R.; Fisher, B.; Mauro, J. M. Self-Assembled Nanoscale Biosensors Based on Quantum Dot FRET Donors. *Nat. Mater.* **2003,** *2*, 630-638.
43. Kodaimati, M. S.; Wang, C.; Chapman, C.; Schatz, G. C.; Weiss, E. A. Distance-Dependence of Interparticle Energy Transfer in the Near-Infrared within Electrostatic Assemblies of PbS Quantum Dots. *ACS Nano* **2017,** *11*, 5041-5050.
44. Liu, Y.-S.; Sun, Y.; Vernier, P. T.; Liang, C.-H.; Chong, S. Y. C.; Gundersen, M. A. pH-Sensitive Photoluminescence of CdSe/ZnSe/ZnS Quantum Dots in Human Ovarian Cancer Cells. *J. Phys. Chem. C* **2007,** *111*, 2872-2878.
45. Nagaraja, A. T.; Sooresh, A.; Meissner, K. E.; McShane, M. J. Processing and Characterization of Stable, pH-Sensitive Layer-by-Layer Modified Colloidal Quantum Dots. *ACS Nano* **2013,** *7*, 6194-6202.
46. Gregory, J. Monitoring Particle Aggregation Processes. *Adv. Colloid Interface Sci.* **2009,** *147-148*, 109-123.
47. Pons, T.; Uyeda, H. T.; Medintz, I. L.; Mattoussi, H. Hydrodynamic Dimensions, Electrophoretic Mobility, and Stability of Hydrophilic Quantum Dots. *J. Phys. Chem. B* **2006,** *110*, 20308-20316.
48. Wang, D.; Kowalczyk, B.; Lagzi, I.; Grzybowski, B. A. Bistability and Hysteresis During Aggregation of Charged Nanoparticles. *J. Phys. Chem. Lett.* **2010,** *1*, 1459-1462.

49. Bishop, K. J. M.; Grzybowski, B. A. “Nanoions”: Fundamental Properties and Analytical Applications of Charged Nanoparticles. *ChemPhysChem* **2007,** *8*, 2171-2176.
50. Bishop, K. J. M.; Wilmer, C. E.; Soh, S.; Grzybowski, B. A. Nanoscale Forces and their Uses in Self-Assembly. *Small* **2009,** *5*, 1600-1630.
51. Wang, C.; Kodaimati, M. S.; Schatz, G. C.; Weiss, E. A. The Photoluminescence Spectral Profiles of Water-Soluble Aggregates of PbS Quantum Dots Assembled Through Reversible Metal Coordination. *Chem. Commun.* **2017,** *53*, 1981-1984.
52. Kagan, C. R.; Murray, C. B.; Bawendi, M. G. Long-Range Resonance Transfer of Electronic Excitations in Close-Packed CdSe Quantum-Dot Solids. *Phys. Rev. B* **1996,** *54*, 8633-8643.
53. Caram, J. R.; Bertram, S. N.; Utzat, H.; Hess, W. R.; Carr, J. A.; Bischof, T. S.; Beyler, A. P.; Wilson, M. W. B.; Bawendi, M. G. PbS Nanocrystal Emission is Governed by Multiple Emissive States. *Nano Lett.* **2016,** *16*, 6070-6077.
54. Peterson, J. J.; Krauss, T. D. Fluorescence Spectroscopy of Single Lead Sulfide Quantum Dots. *Nano Lett.* **2006,** *6*, 510-514.
55. Voznyy, O.; Levina, L.; Fan, F.; Walters, G.; Fan, J. Z.; Kiani, A.; Ip, A. H.; Thon, S. M.; Proppe, A. H.; Liu, M., et al. Origins of Stokes Shift in PbS Nanocrystals. *Nano Lett.* **2017,** *17*, 7191-7195.
56. Susumu, K.; Oh, E.; Delehanty, J. B.; Blanco-Canosa, J. B.; Johnson, B. J.; Jain, V.; Hervey, W. J.; Algar, W. R.; Boeneman, K.; Dawson, P. E., et al. Multifunctional Compact Zwitterionic Ligands for Preparing Robust Biocompatible Semiconductor Quantum Dots and Gold Nanoparticles. *J. Am. Chem. Soc.* **2011,** *133*, 9480-9496.
57. Mei, B. C.; Susumu, K.; Medintz, I. L.; Mattoussi, H. Polyethylene Glycol-Based Bidentate Ligands to Enhance Quantum Dot and Gold Nanoparticle Stability in Biological Media. *Nat. Protc.* **2009,** *4*, 412.
58. Moreels, I.; Lambert, K.; Smeets, D.; De Muynck, D.; Nollet, T.; Martins, J. C.; Vanhaecke, F.; Vantomme, A.; Delerue, C.; Allan, G., et al. Size-Dependent Optical Properties of Colloidal PbS Quantum Dots. *ACS Nano* **2009,** *3*, 3023-3030.
59. He, C.; Nguyen, T. D.; Edme, K.; Olvera de la Cruz, M.; Weiss, E. A. Noncovalent Control of the Electrostatic Potential of Quantum Dots through the Formation of Interfacial Ion Pairs. *J. Am. Chem. Soc.* **2017,** *139*, 10126-10132.
60. Uyeda, H. T.; Medintz, I. L.; Jaiswal, J. K.; Simon, S. M.; Mattoussi, H. Synthesis of Compact Multidentate Ligands to Prepare Stable Hydrophilic Quantum Dot Fluorophores. *J. Am. Chem. Soc.* **2005,** *127*, 3870-3878.
61. Deng, D.; Xia, J.; Cao, J.; Qu, L.; Tian, J.; Qian, Z.; Gu, Y.; Gu, Z. Forming Highly Fluorescent Near-Infrared Emitting PbS Quantum Dots in Water Using Glutathione as Surface-Modifying Molecule. *J. Colloid Interface Sci.* **2012,** *367*, 234-240.
62. Charron, G.; Hühn, D.; Perrier, A.; Cordier, L.; Pickett, C. J.; Nann, T.; Parak, W. J. On the Use of pH Titration to Quantitatively Characterize Colloidal Nanoparticles. *Langmuir* **2012,** *28*, 15141-15149.
63. Harris, D. C., *Quantitative Chemical Analysis*. 8th ed.; W.H. Freeman and Co.: New York, 2010.
64. Israelachvili, J. N., Special Interactions: Hydrogen-Bonding and Hydrophobic and Hydrophilic Interactions. In *Intermolecular and Surface Forces (Third Edition)*, Israelachvili, J. N., Ed. Academic Press: San Diego, 2011; pp 151-167.

65. Mourdikoudis, S.; Pallares, R. M.; Thanh, N. T. K. Characterization Techniques for Nanoparticles: Comparison and Complementarity upon Studying Nanoparticle Properties. *Nanoscale* **2018,** *10*, 12871-12934.
66. Andrews, R. N.; Serio, J.; Muralidharan, G.; Ilavsky, J. An in situ USAXS-SAXS-WAXS Study of Precipitate Size Distribution Evolution in a Model Ni-Based Alloy. *J. Appl. Crystallogr.* **2017,** *50*, 734-740.
67. Green, P. B.; Li, Z.; Wilson, M. W. B. PbS Nanocrystals Made with Excess PbCl2 Have an Intrinsic Shell that Reduces Their Stokes Shift. *J. Phys. Chem. Lett.* **2019,** *10*, 5897-5901.
68. Weir, M. P.; Toolan, D. T. W.; Kilbride, R. C.; Penfold, N. J. W.; Washington, A. L.; King, S. M.; Xiao, J.; Zhang, Z.; Gray, V.; Dowland, S., et al. Ligand Shell Structure in Lead Sulfide–Oleic Acid Colloidal Quantum Dots Revealed by Small-Angle Scattering. *J. Phys. Chem. Lett.* **2019,** *10*, 4713-4719.
69. Maes, J.; Castro, N.; De Nolf, K.; Walravens, W.; Abécassis, B.; Hens, Z. Size and Concentration Determination of Colloidal Nanocrystals by Small-Angle X-ray Scattering. *Chem. Mater.* **2018,** *30*, 3952-3962.
70. Winslow, S. W.; Shcherbakov-Wu, W.; Liu, Y.; Tisdale, W. A.; Swan, J. W. Characterization of Colloidal Nanocrystal Surface Structure Using Small Angle Neutron Scattering and Efficient Bayesian Parameter Estimation. *J. Chem. Phys.* **2019,** *150*, 244702.
71. Genix, A.-C.; Oberdisse, J. Nanoparticle Self-Assembly: From Interactions in Suspension to Polymer Nanocomposites. *Soft Matter* **2018,** *14*, 5161-5179.
72. Musino, D.; Genix, A.-C.; Chaussée, T.; Guy, L.; Meissner, N.; Kozak, R.; Bizien, T.; Oberdisse, J. Aggregate Formation of Surface-Modified Nanoparticles in Solvents and Polymer Nanocomposites. *Langmuir* **2018,** *34*, 3010-3020.
73. Lin, Y.-C.; Chen, H.-L.; Hashimoto, T.; Chen, S.-A. Mechanism of Hierarchical Structure Formation of Polymer/Nanoparticle Hybrids. *Macromolecules* **2016,** *49*, 7535-7550.
74. Lin, Y.-C.; Chen, C.-Y.; Chen, H.-L.; Hashimoto, T.; Chen, S.-A.; Li, Y.-C. Hierarchical Self-Assembly of Nanoparticles in Polymer Matrix and the Nature of the Interparticle Interaction. *J. Chem. Phys.* **2015,** *142*, 214905.
75. Banc, A.; Genix, A.-C.; Chirat, M.; Dupas, C.; Caillol, S.; Sztucki, M.; Oberdisse, J. Tuning Structure and Rheology of Silica–Latex Nanocomposites with the Molecular Weight of Matrix Chains: A Coupled SAXS–TEM–Simulation Approach. *Macromolecules* **2014,** *47*, 3219-3230.
76. Xia, Y.; Nguyen, T. D.; Yang, M.; Lee, B.; Santos, A.; Podsiadlo, P.; Tang, Z.; Glotzer, S. C.; Kotov, N. A. Self-Assembly of Self-Limiting Monodisperse Supraparticles from Polydisperse Nanoparticles. *Nat. Nanotechnol.* **2011,** *6*, 580-587.
77. Tian, Y.; Zhang, Y.; Wang, T.; Xin, H. L.; Li, H.; Gang, O. Lattice Engineering through Nanoparticle–DNA Frameworks. *Nat. Mater.* **2016,** *15*, 654-661.
78. Li, R.; Bian, K.; Hanrath, T.; Bassett, W. A.; Wang, Z. Decoding the Superlattice and Interface Structure of Truncate PbS Nanocrystal-Assembled Supercrystal and Associated Interaction Forces. *J. Am. Chem. Soc.* **2014,** *136*, 12047-12055.
79. Lee, B.; Littrell, K.; Sha, Y.; Shevchenko, E. V. Revealing the Effects of the Non-solvent on the Ligand Shell of Nanoparticles and Their Crystallization. *J. Am. Chem. Soc.* **2019,** *141*, 16651-16662.

80. Schwabacher, J. C.; Kodaimati, M. S.; Weiss, E. A. Origin of the pH Dependence of Emission of Aqueous Dihydrolipoic Acid-Capped PbS Quantum Dots. *J. Phys. Chem. C* **2019,** *123*, 17574-17579.
81. Ilavsky, J.; Jemian, P. R. Irena: Tool Suite for Modeling and Analysis of Small-Angle Scattering. *J. Appl. Crystallogr.* **2009,** *42*, 347-353.
82. Bressler, I.; Kohlbrecher, J.; Thunemann, A. F. SASfit: A Tool for Small-Angle Scattering Data Analysis Using a Library of Analytical Expressions. *J. Appl. Crystallogr.* **2015,** *48*, 1587-1598.
83. Takeuchi, H.; Omogo, B.; Heyes, C. D. Are Bidentate Ligands Really Better than Monodentate Ligands For Nanoparticles? *Nano Lett.* **2013,** *13*, 4746-4752.
84. Lin, W.; Fritz, K.; Guerin, G.; Bardajee, G. R.; Hinds, S.; Sukhovatkin, V.; Sargent, E. H.; Scholes, G. D.; Winnik, M. A. Highly Luminescent Lead Sulfide Nanocrystals in Organic Solvents and Water through Ligand Exchange with Poly(acrylic acid). *Langmuir* **2008,** *24*, 8215-8219.
85. Li, T.; Senesi, A. J.; Lee, B. Small Angle X-ray Scattering for Nanoparticle Research. *Chem. Rev.* **2016,** *116*, 11128-11180.
86. Lund, L. H.; Vineyard, G. H. Inter-Particle Interference Effects in the Small Angle X-Ray Scattering from Fine Powders. *J. Appl. Phys.* **1949,** *20*, 593-597.
87. Mansel, B. W.; Chen, C.-Y.; Lin, J.-M.; Huang, Y.-S.; Lin, Y.-C.; Chen, H.-L. Hierarchical Structure and Dynamics of a Polymer/Nanoparticle Hybrid Displaying Attractive Polymer–Particle Interaction. *Macromolecules* **2019,** *52*, 8741-8750.
88. Genix, A.-C.; Oberdisse, J. Determination of the Local Density of Polydisperse Nanoparticle Assemblies. *Soft Matter* **2017,** *13*, 8144-8155.
89. Anitas, E. M. Small-Angle Scattering from Weakly Correlated Nanoscale Mass Fractal Aggregates. *Nanomaterials* **2019,** *9*.
90. Márquez, A. M.; Pacheco, L. C.; Sanz, J. F. Structural and Electronic Properties of Lead Sulfide Quantum Dots from Screened Hybrid Density Functional Calculations Including Spin–Orbit Coupling Effects. *Theor. Chem. Acc.* **2017,** *136*, 58.
91. Percus, J. K.; Yevick, G. J. Analysis of Classical Statistical Mechanics by Means of Collective Coordinates. *Phys. Rev.* **1958,** *110*, 1-13.
92. Vrij, A. Mixtures of Hard Spheres in the Percus–Yevick Approximation. Light Scattering at Finite Angles. *J. Chem. Phys.* **1979,** *71*, 3267-3270.
93. Beaucage, G. Small-Angle Scattering from Polymeric Mass Fractals of Arbitrary Mass-Fractal Dimension. *J. Appl. Crystallogr.* **1996,** *29*, 134-146.
94. Beaucage, G. Approximations Leading to a Unified Exponential Power-Law Approach to Small-Angle Scattering. *J. Appl. Crystallogr.* **1995,** *28*, 717-728.
95. Hecht, F. M.; Bausch, A. R. Kinetically Guided Colloidal Structure Formation. *Proc. Natl. Acad. Sci. U. S. A.* **2016,** *113*, 8577.
96. Zhang, W., Nanoparticle Aggregation: Principles and Modeling. In *Nanomaterial: Impacts on Cell Biology and Medicine*, Capco, D. G.; Chen, Y., Eds. Springer Netherlands: Dordrecht, 2014; pp 19-43.
97. Jungblut, S.; Eychmüller, A., Modeling Nanoparticle Aggregation. In *Chemical Modelling: Volume 15*, The Royal Society of Chemistry: 2020; Vol. 15, pp 1-27.
98. Zhao, K.; Mason, T. G. Assembly of Colloidal Particles in Solution. *Rep. Prog. Phys.* **2018,** *81*.

99. Kasap, S. O., *Principles of Electronic Materials and Devices*. 3rd ed.; McGraw-Hill: Boston, 2006; p xiii, 874 p.
100. Kim, B. H.; Heo, J.; Kim, S.; Reboul, C. F.; Chun, H.; Kang, D.; Bae, H.; Hyun, H.; Lim, J.; Lee, H., et al. Critical Differences in 3D Atomic Structure of Individual Ligand-Protected Nanocrystals in Solution. *Science* **2020,** *368*, 60.
101. Zhang, Y.; Lu, F.; Yager, K. G.; van der Lelie, D.; Gang, O. A General Strategy for the DNA-Mediated Self-Assembly of Functional Nanoparticles into Heterogeneous Systems. *Nat. Nanotechnol.* **2013,** *8*, 865-872.
102. Laramy, C. R.; O'Brien, M. N.; Mirkin, C. A. Crystal Engineering with DNA. *Nat. Rev. Mater.* **2019,** *4*, 201-224.
103. Macfarlane, R. J.; O'Brien, M. N.; Petrosko, S. H.; Mirkin, C. A. Nucleic Acid-Modified Nanostructures as Programmable Atom Equivalents: Forging a New "Table of Elements". *Angew. Chem. Int. Ed.* **2013,** *52*, 5688-5698.
104. Mirkin, C. A.; Letsinger, R. L.; Mucic, R. C.; Storhoff, J. J. A DNA-Based Method for Rationally Assembling Nanoparticles into Macroscopic Materials. *Nature* **1996,** *382*, 607-609.
105. Zhang, C.; Macfarlane, R. J.; Young, K. L.; Choi, C. H. J.; Hao, L.; Auyeung, E.; Liu, G.; Zhou, X.; Mirkin, C. A. A General Approach to DNA-Programmable Atom Equivalents. *Nat. Mater.* **2013,** *12*, 741-746.
106. Zheng, Y.; Thai, T.; Reineck, P.; Qiu, L.; Guo, Y.; Bach, U. DNA-Directed Self-Assembly of Core-Satellite Plasmonic Nanostructures: A Highly Sensitive and Reproducible Near-IR SERS Sensor. *Adv. Funct. Mater.* **2013,** *23*, 1519-1526.
107. Deka, J.; Měch, R.; Ianeselli, L.; Amenitsch, H.; Cacho-Nerin, F.; Parisse, P.; Casalis, L. Surface Passivation Improves the Synthesis of Highly Stable and Specific DNA-Functionalized Gold Nanoparticles with Variable DNA Density. *ACS Appl. Mater. Interfaces* **2015,** *7*, 7033-7040.
108. Boles, M. A.; Engel, M.; Talapin, D. V. Self-Assembly of Colloidal Nanocrystals: From Intricate Structures to Functional Materials. *Chem. Rev.* **2016,** *116*, 11220-11289.
109. Saha, K.; Agasti, S. S.; Kim, C.; Li, X.; Rotello, V. M. Gold Nanoparticles in Chemical and Biological Sensing. *Chem. Rev.* **2012,** *112*, 2739-2779.
110. Seo, S. E.; Girard, M.; Olvera de la Cruz, M.; Mirkin, C. A. Non-Equilibrium Anisotropic Colloidal Single Crystal Growth with DNA. *Nat. Commun.* **2018,** *9*, 4558.
111. Tommasini-Ghelfi, S.; Lee, A.; Mirkin, C. A.; Stegh, A. H., Synthesis, Physicochemical, and Biological Evaluation of Spherical Nucleic Acids for RNAi-Based Therapy in Glioblastoma. In *RNA Interference and Cancer Therapy: Methods and Protocols*, Dinesh Kumar, L., Ed. Springer New York: New York, NY, 2019; pp 371-391.
112. Zhu, J.; Lin, H.; Kim, Y.; Yang, M.; Skakuj, K.; Du, J. S.; Lee, B.; Schatz, G. C.; Van Duyne, R. P.; Mirkin, C. A. Light-Responsive Colloidal Crystals Engineered with DNA. *Adv. Mater.* **2020,** *32*, 1906600.
113. Gill, R.; Willner, I.; Shweky, I.; Banin, U. Fluorescence Resonance Energy Transfer in CdSe/ZnS−DNA Conjugates: Probing Hybridization and DNA Cleavage. *J. Phys. Chem. B* **2005,** *109*, 23715-23719.
114. Hildebrandt, N.; Spillmann, C. M.; Algar, W. R.; Pons, T.; Stewart, M. H.; Oh, E.; Susumu, K.; Díaz, S. A.; Delehanty, J. B.; Medintz, I. L. Energy Transfer with Semiconductor Quantum Dot Bioconjugates: A Versatile Platform for Biosensing, Energy Harvesting, and Other Developing Applications. *Chem. Rev.* **2017,** *117*, 536-711.

115. Goryacheva, O. A.; Novikova, A. S.; Drozd, D. D.; Pidenko, P. S.; Ponomaryeva, T. S.; Bakal, A. A.; Mishra, P. K.; Beloglazova, N. V.; Goryacheva, I. Y. Water-Dispersed Luminescent Quantum Dots for miRNA Detection. *TrAC, Trends Anal. Chem.* **2019,** *111*, 197-205.
116. Zhang, T.; Liedl, T. DNA-Based Assembly of Quantum Dots into Dimers and Helices. *Nanomaterials* **2019,** *9*.
117. Yamauchi, M.; Masuo, S. Self-Assembly of Semiconductor Quantum Dots using Organic Templates. *Chem. Eur. J* **2020**.
118. Tikhomirov, G.; Hoogland, S.; Lee, P. E.; Fischer, A.; Sargent, E. H.; Kelley, S. O. DNA-Based Programming of Quantum Dot Valency, Self-Assembly and Luminescence. *Nat. Nanotechnol.* **2011,** *6*, 485-490.
119. Coopersmith, K.; Han, H.; Maye, M. M. Stepwise Assembly and Characterization of DNA Linked Two-Color Quantum Dot Clusters. *Langmuir* **2015,** *31*, 7463-7471.
120. Hu, J.; Liu, M.-h.; Zhang, C.-y. Construction of Tetrahedral DNA-Quantum Dot Nanostructure with the Integration of Multistep Förster Resonance Energy Transfer for Multiplex Enzymes Assay. *ACS Nano* **2019,** *13*, 7191-7201.
121. Yang, Y.; Mao, G.; Ji, X.; He, Z. DNA-Templated Quantum Dots and Their Applications in Biosensors, Bioimaging, and Therapy. *J. Mater. Chem. B* **2020,** *8*, 9-17.
122. Zhang, H.; Li, M.; Wang, K.; Tian, Y.; Chen, J.-S.; Fountaine, K. T.; DiMarzio, D.; Liu, M.; Cotlet, M.; Gang, O. Polarized Single-Particle Quantum Dot Emitters through Programmable Cluster Assembly. *ACS Nano* **2020,** *14*, 1369-1378.
123. Banerjee, A.; Pons, T.; Lequeux, N.; Dubertret, B. Quantum Dots-DNA Bioconjugates: Synthesis to Applications. *Interface Focus* **2016,** *6*, 20160064.
124. Deng, Z.; Samanta, A.; Nangreave, J.; Yan, H.; Liu, Y. Robust DNA-Functionalized Core/Shell Quantum Dots with Fluorescent Emission Spanning from UV–vis to Near-IR and Compatible with DNA-Directed Self-Assembly. *J. Am. Chem. Soc.* **2012,** *134*, 17424-17427.
125. Madsen, M.; Gothelf, K. V. Chemistries for DNA Nanotechnology. *Chem. Rev.* **2019,** *119*, 6384-6458.
126. Mitchell, G. P.; Mirkin, C. A.; Letsinger, R. L. Programmed Assembly of DNA Functionalized Quantum Dots. *J. Am. Chem. Soc.* **1999,** *121*, 8122-8123.
127. Xing, M.; Shen, H.; Zhao, W.; Liu, Y.; Du, Y.; Yu, Z.; Chen, X. dsDNA-coated Quantum Dots. *BioTechniques* **2011,** *50*, 259-261.
128. Patolsky, F.; Gill, R.; Weizmann, Y.; Mokari, T.; Banin, U.; Willner, I. Lighting-Up the Dynamics of Telomerization and DNA Replication by CdSe−ZnS Quantum Dots. *J. Am. Chem. Soc.* **2003,** *125*, 13918-13919.
129. Meng, H.; Yang, Y.; Chen, Y.; Zhou, Y.; Liu, Y.; Chen, X. a.; Ma, H.; Tang, Z.; Liu, D.; Jiang, L. Photoelectric Conversion Switch based on Quantum Dots with i-motif DNA Scaffolds. *Chem. Commun.* **2009**, 2293-2295.
130. Medintz, I. L.; Berti, L.; Pons, T.; Grimes, A. F.; English, D. S.; Alessandrini, A.; Facci, P.; Mattoussi, H. A Reactive Peptidic Linker for Self-Assembling Hybrid Quantum Dot−DNA Bioconjugates. *Nano Lett.* **2007,** *7*, 1741-1748.
131. Diamandis, E. P.; Christopoulos, T. K. The Biotin-(Strept)Avidin System: Principles and Applications in Biotechnology. *Clin. Chem.* **1991,** *37*, 625-636.
132. Mamidyala, S. K.; Finn, M. G. In situ Click Chemistry: Probing the Binding Landscapes of Biological Molecules. *Chem. Soc. Rev.* **2010,** *39*, 1252-1261.

133. Tiefenbrunn, T. K.; Dawson, P. E. Chemoselective Ligation Techniques: Modern Applications of Time-honored Chemistry. *J. Pept. Sci.* **2010,** *94*, 95-106.
134. Boeneman, K.; Deschamps, J. R.; Buckhout-White, S.; Prasuhn, D. E.; Blanco-Canosa, J. B.; Dawson, P. E.; Stewart, M. H.; Susumu, K.; Goldman, E. R.; Ancona, M., et al. Quantum Dot DNA Bioconjugates: Attachment Chemistry Strongly Influences the Resulting Composite Architecture. *ACS Nano* **2010,** *4*, 7253-7266.
135. Le, T.-H.; Kim, S.; Chae, S.; Choi, Y.; Park, C. S.; Heo, E.; Lee, U.; Kim, H.; Kwon, O. S.; Im, W. B., et al. Zero Reduction Luminescence of Aqueous-Phase Alloy Core/Shell Quantum Dots via Rapid Ambient-Condition Ligand Exchange. *J. Colloid Interface Sci.* **2020,** *564*, 88-98.
136. Bligh, E. G.; Dyer, W. J. A Rapid Method of Total Lipid Extraction and Purification. *Can. J. Biochem. Physiol.* **1959,** *37*, 911-917.
137. Folch, J.; Lees, M.; Stanley, G. H. S. A Simple Method for the Isolation and Purification of Total Lipides from Animal Tissues. *J. Biol. Chem.* **1957,** *226*, 497-509.
138. Mahler, B.; Spinicelli, P.; Buil, S.; Quelin, X.; Hermier, J. P.; Dubertret, B. Towards Non-blinking Colloidal Quantum Dots. *Nat. Mater.* **2008,** *7*, 659-664.
139. Rouhana, L. L.; Jaber, J. A.; Schlenoff, J. B. Aggregation-resistant water-soluble gold nanoparticles. *Langmuir* **2007,** *23*, 12799-12801.
140. Hill, H. D.; Mirkin, C. A. The Bio-Barcode Assay for the Detection of Protein and Nucleic Acid Targets using DTT-Induced Ligand Exchange. *Nat. Protc.* **2006,** *1*, 324-336.
141. Hurst, S. J.; Lytton-Jean, A. K. R.; Mirkin, C. A. Maximizing DNA Loading on a Range of Gold Nanoparticle Sizes. *Anal. Chem.* **2006,** *78*, 8313-8318.
142. Zhu, J.; Kim, Y.; Lin, H.; Wang, S.; Mirkin, C. A. pH-Responsive Nanoparticle Superlattices with Tunable DNA Bonds. *J. Am. Chem. Soc.* **2018,** *140*, 5061-5064.
143. Yu, W. W.; Qu, L.; Guo, W.; Peng, X. Experimental Determination of the Extinction Coefficient of CdTe, CdSe and CdS Nanocrystals. *Chem. Mater.* **2004,** *16*, 560-560.
144. Yu, W. W.; Qu, L.; Guo, W.; Peng, X. Experimental Determination of the Extinction Coefficient of CdTe, CdSe, and CdS Nanocrystals. *Chem. Mater.* **2003,** *15*, 2854-2860.
145. Kim, H.; Jeen, T.; Tran, M. V.; Algar, W. R. Polyacrylamide Gel Electrophoresis of Semiconductor Quantum Dots and Their Bioconjugates: Materials Characterization and Physical Insights from Spectrofluorimetric Detection. *Analyst* **2018,** *143*, 1104-1116.
146. Kessler, M. L.; Dempsey, J. L. Mapping the Topology of PbS Nanocrystals through Displacement Isotherms of Surface-Bound Metal Oleate Complexes. *Chem. Mater.* **2020,** *32*, 2561-2571.
147. Kessler, M. L.; Starr, H. E.; Knauf, R. R.; Rountree, K. J.; Dempsey, J. L. Exchange equilibria of carboxylate-terminated ligands at PbS nanocrystal surfaces. *Phys. Chem. Chem. Phys.* **2018,** *20*, 23649-23655.
148. Brown, P. R. The Investigation of Some Reactions of Alpha-Lipoic Acid. Brown University, 1968.
149. Winslow, S. W.; Liu, Y.; Swan, J. W.; Tisdale, W. A. Quantification of a PbClx Shell on the Surface of PbS Nanocrystals. *ACS Mater. Lett.* **2019,** *1*, 209-216.
150. Winslow, S. W.; Swan, J. W.; Tisdale, W. A. The Importance of Unbound Ligand in Nanocrystal Superlattice Formation. *J. Am. Chem. Soc.* **2020,** *142*, 9675-9685.